A Thesis for the Doctor of Philosophy

Tetrahydrobenzimidazole TMQ0153 induces autophagy followed by controlled necrosis via oxidative stress induction in chronic myeloid leukemia cell lines

반합성천연물 TMQ0153 (Tetrahydrobenzimidazole)이 일으키는 세포사멸과 만성 백혈병 치료법 연구

February, 2020

Sungmi Song

College of Pharmacy
Seoul National University

Tetrahydrobenzimidazole TMQ0153 induces autophagy followed by controlled necrosis via oxidative stress induction in chronic myeloid leukemia cell lines

by

Sungmi Song

A thesis submitted in partial fulfillment of the

requirements for the degree of

DOCTOR OF PHILOSOPHY

(Pharmacy: Pharmaceutical bioscience major)

Under the supervision of

Professor Marc Francois Diederich

College of Pharmacy
Seoul National University

February 2020

Overall Abstract

Tetrahydrobenzimidazole TMQ0153 induces autophagy followed by controlled necrosis via oxidative stress induction in chronic myeloid leukemia cell lines

Sungmi Song
College of Pharmacy
Department of Pharmacy Graduate School
Advisor: Prof. Marc Francois Diederich

Chronic myeloid leukemia (CML) is characterized by the Philadelphia (Ph) chromosome with a t(9;22)(q34;q11) reciprocal translocation in single hemopoietic stem cells (HSC) and resulting in expression of the BCR-ABL chimeric oncoprotein. This abnormal gene stimulates the production of reactive oxygen species (ROS). ROS levels increase with CML progression and induce BCR-ABL self-mutagenesis. Imatinib and other tyrosine kinase inhibitors (TKIs) such as dasatinib and nilotinib radically improved the diseases outcome, but TKI-resistance is still considered as a major problem. TKI resistance can be associated with even higher ROS production than in TKI-sensitive cells. So far, a role for redox changes in apoptosis has been established; however, several new modalities of regulated cell death have been recently described, The importance of ROS production as well as cellular stress are being actively investigated. Taken together, we investigate here the role of ROS and redox changes in the activation and execution of regulated necroptosis. We also discuss how cellular stress and redox modulation by TMQ0153 concentration-dependently leads to different cell death modalities including controlled necrosis in CML cell models.

Keywords : Tetrahydrobenzimidazole; Metabolic stress; ROS; Cell death; Chronic myeloid leukemia therapy

Student Number : 2014-21957

Table of Contents

List of Tables

List of Figures

Chapter 1. Redox biology of regulated cell death in cancer: A focus on necroptosis

Chapter 2. Tetrahydrobenzimidazole TMQ0153 triggers apoptosis, autophay and necroptosis crosstalk in chronic myeloid leukemia

List of Abbreviations

3-MA	3-methyladenine
5-aza	5-aza-2’-deoxycytidine
ATP	adenosine triphosphate
Baf-A1	bafilomycin A1
BCR-ABL	breakpoint cluster region-Abelson
Bcl-xL	B-cell lymphoma-extra large
BSO	buthionine sulfoximine
CML	chronic myeloid leukemia
COX	cyclooxygenase
CQ	chloroquine
CRT	calreticulin
CypD	cyclophilin D
DMSO	dimethyl sulfoxide
DAMP	damage-associated molecular pattern
EtOH	ethanol
ELISA	enzyme-linked immunosorbent assay
FACS	fluorescence-activated cell sorting
FITC	fluorescein isothiocyanate
GSH	glutathione
GR	glutathionereductase
GPX	glutathioneperoxidase
H_2DCFDA	2′,7′-Dichlorofluorescin diacetate
HMGB1	high mobility group box
HNE	hydroxynonenal
HQ	hydroquinone
ICD	immunogenic cell death
LMP	lysosomal membrane permeabilization
LOX	lipooxigenase

NOX	NADPHoxidase;
MCL	myeloid cell leukemia
MDA	malondialdehyde
MLKL	mixed lineage kinase domain-like
MMP	mitochondrial membrane potential
mPTP	mitochondrial permeability transition pore
mTOR	mammalian target of rapamycin
NAC	N-acetyl-L-cysteine
NAD(P)H	nicotinamide adenine dinucleotide phosphate hydride
NOX	NADPHoxidase
Nec-1	necrostatin-1
NQO1	NAD(P)Hquinineoxidoreductase1
OCR	oxygen consumption rate
PARP	poly [ADP-ribose] polymerase
PBMC	peripheral blood mononuclear cell
PCD	programmed cell death
PEBP1	phosphatidylethanolamine binding protein 1
PI	propidium iodide
PKM2	pyruvate kinase M2
PLA2	phospholypase A2
PRX	peroxiredoxin
PUFA	polyunsaturated fatty acid
RFK	riboflavin kinase
RIP	receptor-interacting protein kinase
ROS	reactive oxygen species
RSL-3	Ras selective lethal-3
siRNA	small interfering RNA
SERCA	sarco /endoplasmic reticulum Ca^{2+} -ATPase
SOD	superoxide dismutase
SQSTM1	sequestosome-1

TEM	transmission electron microscopy
TKI	tyrosine kinase inhibitor
TMQ	tetrahydrobenzimidazole
TNF	tumor necrosis factor
TRX	thioredoxin
TSG	thapsigargin
XO	xanthine oxidase
z-VAD	carbobenzoxy-valyl-alanyl-aspartyl-[O-methyl]-fluoromethylketone

Chapter 1.

Redox biology of regulated cell death in cancer: A focus on necroptosis

1.1. Abstract

Redox changes and generation of reactive oxygen species (ROS) are part of normal cell metabolism. While low ROS levels are implicated in cellular signaling pathways necessary for survival, higher levels play major roles in cancer development as well as cell death signaling and execution. A role for redox changes in apoptosis has been long established; however, several new modalities of regulated cell death have been brought to light, for which the importance of ROS production as well as ROS source and targets are being actively investigated. In this review, we summarize recent findings on the role of ROS and redox changes in the activation and execution of two major forms of regulated cell death, necroptosis and ferroptosis. We also discuss the potential of using modulators of these two forms of cell death to exacerbate ROS as a promising anticancer therapy.

Keywords: ROS, Redox changes Regulated cell death, Necroptosis, Cancer Anticancer therapy

1.2. Introduction

1.2.1. Redox homeostasis in normal and cancer cells

Reduction and oxidation (red-ox) reactions occur in living organisms as part of the normal cellular metabolism. They consist in the loss or acquisition of electrons by an atom, which leads to generation of reactive, mostly short-lived intermediates. The most relevant molecules produced by redox events in the cells are reactive oxygen species (ROS), derived from O_2 metabolism and comprising free radicals, such as superoxide anion ($O_2^{\bullet -}$) and hydroxyl radical ($^{\bullet}OH$), as well as non-radical species such as hydrogen peroxide (H_2O_2) [1, 2].

ROS can be generated by several physiological and pathological mechanisms. Mitochondria are the major ROS generator of the cell, mainly through leakage of oxidative phosphorylation, where approximately 1% of all mitochondrial O_2 is converted to superoxide [3]. ROS may also be generated also in other organelles such as peroxisomes and the endoplasmic reticulum (ER) and by the activity of NADPH oxidases (NOX)—enzymes specialized in ROS production [4]. Several other enzymatic activities are involved in ROS generation, including lipooxigenase (LOX), cyclooxigenase (COX), xanthine oxidase (XO), nitric oxide synthase (NOS) activities [5]. ROS production may also result from exposure to environmental stressors, such as xenobiotics or variations in environmental parameters [6].

While redox homeostasis is pivotal for cell survival, ROS play a dichotomous role in the cell. At submicromolar concentrations, they act as second messengers, regulating cellular signaling and participating in the control of several cellular functions, such as cell growth, survival, and differentiation [7, 8]. When ROS levels rise above a critical level, they cause oxidative damage to cell structures. For this reason, spikes of ROS are usually rapidly neutralized to a steady state level by a series of antioxidant cellular systems, comprising enzymes such as superoxide dismutase (SOD), catalase, glutathione reductase (GR), glutathione peroxidase (GPX),

thioredoxins (TRX), and peroxiredoxins (PRX) [2, 5].

If optimal redox homeostasis is compromised, due to ROS overproduction or decreased antioxidant activity, the cell undergoes cell death or survives by developing strategies to cope with chronically higher ROS levels. This adaptive situation can in turn contribute to the development of several pathologies, such as neurological disorders or cancer [9, 10, 11].

ROS are known to modulate cancer-promoting functions, such as proliferation, migration and metastasis [12, 13, 14]. Deregulated ROS homeostasis may also lead to epigenetic alterations [15], which may further contribute to cancer progression [16, 17] by modulating the expression of genes involved in ROS detoxification [18].

However, to cope with the high amounts of ROS from a deregulated energetic metabolism, cancer cells increase antioxidant defense systems [9]. In this context, it is important to consider that ROS may also have tumor suppressive roles [19]. Stabilization of a master regulator of antioxidant response, Nuclear Factor erythroid 2-related factor (NRF2) has been reported following oncogene activation, and is a driver of cancer proliferation [20]. Remarkably, the supplementation of antioxidants was shown to increase incidence and mortality in some cancers types, such as lung cancer [21]. Finally, the oxidative homeostasis of cancer *in vivo* may be also modulated by the interaction with its specific tumor microenvironment [22], adding another layer to the complexity of ROS management in *in vivo* contexts.

When oxidative stress becomes excessively high, cancer cell death is induced. Exacerbating oxidative stress by increasing ROS levels or decreasing cellular antioxidant capacity is a promising potential anticancer strategy and part of the mechanism of action of many chemotherapeutic drugs already in clinical use [23, 24, 25, 26, 27, 28].

1.2.2. ROS-induced events accompanying cell death

We have only just begun to understand the complexity of the role of ROS in cell death. At lower levels, ROS have been linked to cell signaling and survival responses [8]. At higher levels, ROS may be involved in the signaling steps that precede and regulate cell death in response to several stimuli [1]. Moreover, excessive ROS levels oxidize DNA, proteins, and lipids, compromising their structure and function and participating in the execution of cell death (**Figure 1.1**).

The superoxide generated mainly by mitochondrial respiration, is converted to hydrogen peroxide by SOD. While hydrogen peroxide has relatively low reactivity, it can be converted into the potent hydroxyl radical in the presence of iron by Fenton reactions [8]. The extremely high reactivity of the hydroxyl radical is responsible a considerable amount of oxidative damage [29, 30]. Both superoxide and hydrogen peroxide can modify proteins, typically reacting with thiol groups to generate disulfide forms. Protein function is tightly controlled by amino-acid modifications, and reversible oxidation is well described as a mechanism of ROS-controlled cell signaling [8, 30]. Signaling through oxidized cysteine may promote survival mechanism such as autophagy [31]. However, when hydrogen peroxide levels are markedly increased, the subsequent production of high amounts of hydroxyl radical cause irreversible protein oxidation and cellular toxicity [8].

DNA is less easily oxidized than cysteine thiols; however, it can undergo multiple types of damage from the predominant oxidation of single bases up to interstrand and DNA-protein crosslinks when significant amounts of potent radicals come into proximity [29, 32]. If not repaired, DNA damage may lead to mutations, epigenetic alterations and genetic instability, or in the case of massive damage, induction of cell death [33].

Lipid peroxides can be formed as result of uncontrolled ROS propagation as well as by the action of specific enzymes, such as LOX, COX and cytocrome P450. The antioxidant enzyme GPX plays an important

role in limiting lipid peroxide formation by utilizing L-γ-glutamyl-L-cysteinylglycine (glutathione; GSH) to neutralize them. Lipid peroxides are able to diffuse across lipid bilayers, compromising membrane integrity and may also propagate the production of other ROS species and be degraded into more toxic compounds, which participate in DNA and protein crosslinking [10, 34]. GSH is the most prominent cellular reducing agent. Its free thiol group becomes oxidized to glutathione disulfide (GSSG) to buffer oxidative stress. Healthy cells constantly maintain a high GSH-to-GSSG ratio to ensure a high buffering capacity against increased ROS levels [35]. A decrease in the GSH pool is a hallmark of cell death following an oxidative burst, with important roles in apoptosis regulation [36]. GSH depletion can either be the result of massive consumption via oxidation in an attempt to buffer the peak in ROS levels or due to GSH efflux through membrane transport [36, 37].

Based on the large spectrum of activities described above, ROS can participate in different steps of cell death. Their exact contribution to each of those steps, however, remains unclear. In early studies, apoptosis was shown to occur in conditions of low O_2 [38, 39, 40]. In the last decades ROS have been implicated in signaling leading to apoptosis induction [2, 6], such as in JNK activation following TNFα stimuli [41].

The underlying mechanisms of ROS involvement in other forms of regulated cell death are even less defined and are the current subject of intense investigation.

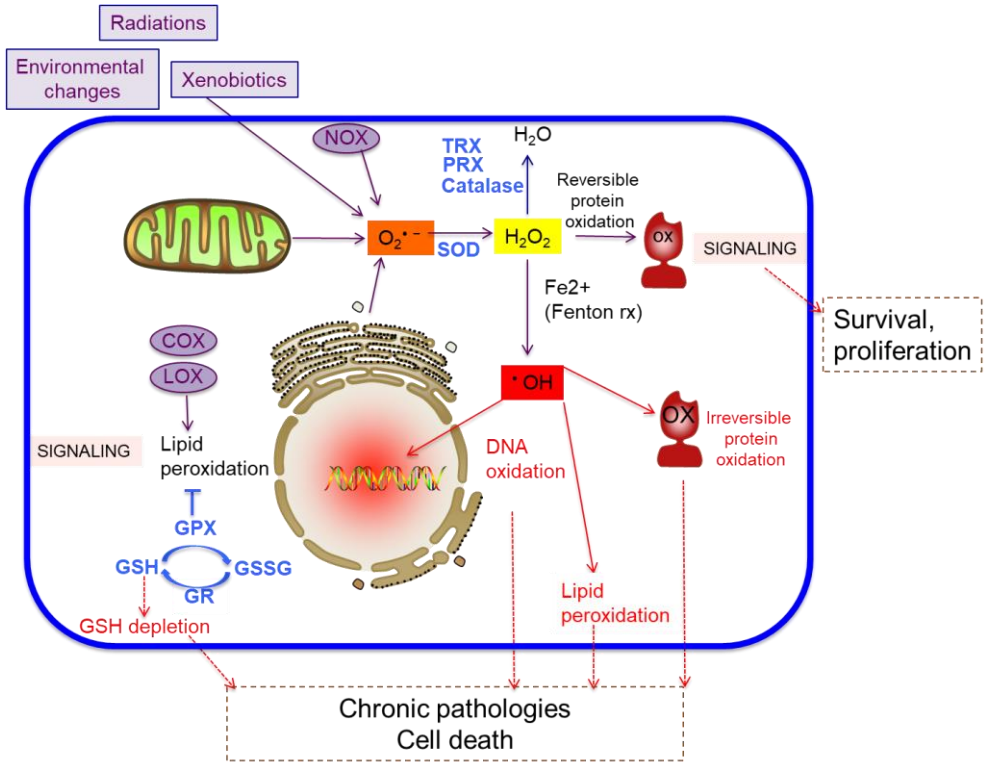

Figure 1.1. Cellular redox homeostasis. Schematic overview of major redox events in cells. ROS may lead to pro-survival signaling or to cellular damage and eventually cell death, based on the extent of oxidative stress and the cellular antioxidant capacity. When the antioxidant system is not capable of coping with high amounts of stress, damaging events (depicted in red) occur and participate incellexecution. Alternatively, ifthe cellsareable to survive, these events may contribute to the development of chronic diseases. GSH: glutathione; GSSG: glutathione disulfide; GR: glutathione reductase; GPX: glutathione peroxidase; TRX: thioredoxin; PRX: peroxiredoxin; COX: cyclooxygenase; LOX: lipoxygenase; NOX: NADPH oxidase; rx: reactions.

1.3. Regulated cell death (RDC) and ROS

For decades, apoptosis was considered the only form of regulated cell death (RDC), as opposed to necrosis, which was regarded as an accidental and uncontrollable form of cell death, independent of any specific genetic program. However, accumulating evidence in the previous years showed that many forms of non-apoptotic, RDC exist [42, 43, 44, 45]. Nowadays, these RDC forms are regarded as a class of genetically regulated type of cell death, each one impinging on different (although overlapping) signaling pathways. Morphologically, non-apoptotic RDC are characterized by cellular swelling, plasma membrane damage, and cell content leakage [45]; however, peculiar morphological features exist, as evidenced by ferroptosis (see dedicated paragraph). Although differing in the molecular pathways that elicit them, non-apoptotic RDC share some downstream execution mechanisms. In this regard, bioenergetics and redox metabolism disruption have been proposed as a common basis in their progression and execution [45].

Among the non-apoptotic RDC forms described thus far, necroptosis is the best characterized. Other recently discovered forms include pyroptosis, parthanatos, NETotic cell death, and ferroptosis [43, 44, 45]. We will focus below on redox involvement in two of these forms, necroptosis, as forerunner of the group and for which the role of ROS has been long investigated, and ferroptosis, an oxidative form of cell death for which alterations in redox metabolism constitute the main deciphered mechanism of action **(Figure 1.2)**.

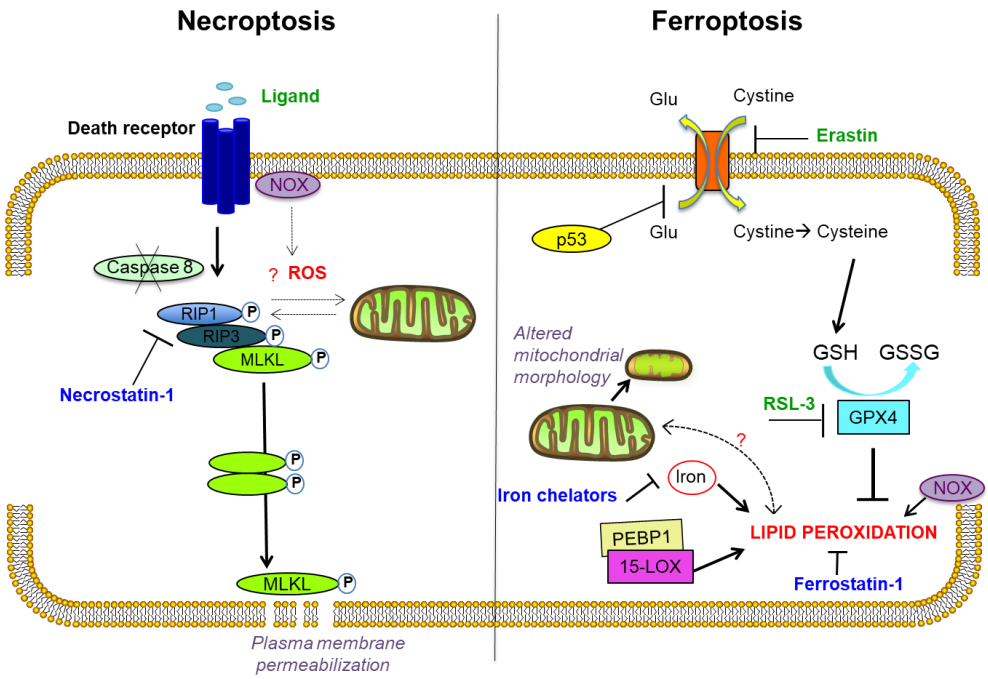

Figure 1.2. Schematic representation of Necroptosis and Ferroptosis pathways and relative ROS involvement. A simplified overview of the main players involved in necroptosis and ferroptosis is depicted. Confirmed or potential ROS involvement is indicated in red and main agents responsible for induction and inhibition of the two cell death pathways are indicated in green and blue, respectively. 15-LOX: 15-lipoxigenase; Becn-1: Beclin-1; DDP4: dipeptidyl-peptidase4; PEBP1: phosphatidylethanolamine binding protein 1; NOX: NADPH oxidase; NRF2: Nuclear factor erythroid 2-related factor 2; MLKL: mixed lineage kinase domain-like pseudokinase; RIP: receptor-interacting protein; Glu: glutamate; RSL-3: Ras-selective lethal 3.

1.3.1. The role of ROS in necroptosis

Over the last decade, necroptosis occurrence has been described in many pathological contexts [46]. Sharing some key features with apoptosis, necroptosis was mainly described to occur under pharmacological inhibition or genetic deletion of caspases, as a “backup” form of programmed cell death upon cellular inability to activate apoptosis [47]. The involvement of necroptosis during infection and inflammation has been also well

established; however, there are no indications (to date) of a physiological role during development [46].

Necroptosis can be induced by ligands binding to receptors of the tumor necrosis factor (TNF) family [48, 49]. Several other stimuli have been associated with necroptosis induction, such as ER stress [50, 51, 52], DNA damage [33], anticancer drugs [53], viruses [54] and bacteria [55]. The main molecular signaling events of necroptosis involve the activation of a multi-protein complex called necrosome, harboring the receptor-interacting kinases RIP1 and RIP3 as key mediators and the executioner protein mixed lineage kinase domain-like (MLKL). After death receptor stimulation, and in the absence of caspase-8 availability, RIP1 recruits RIP3, promoting its activation. Then, the effector protein MLKL and constitutive binding partner of RIP3 becomes activated, oligomerizes, and translocates to the plasma or intracellular membranes [56], where it can form cationic channels leading to membrane permeabilization [57]. A conformational switch of the pseudokinase domain of MLKL is achieved upon RIP3 stimulation, which leads to the constitution of the active tetrameric form. In this form, the four-helix bundle (4HB) domain of the protein is unmasked [58] and binds to phosphatidylinositol phosphates in the membrane leading to permeabilization [59].

RIP1 is not always required for necroptosis induction. After stimulation of Toll-like receptors (TLR), necroptosis can proceed *via* TIR domain-containing adapter-inducing interferon-β (TRIF)-RIP3 complexes [60], and virus-induced necroptosis may be coordinated by the DNA sensor DAI and RIP3, independently from RIP1 [61]. In fact, to see RIP1 only as an activator of necroptosis would be too simplistic; its presence is also required to protect cells both from caspase 8-induced apoptosis and from RIP3-dependent necroptosis, as shown by genetic studies in mice [62]. Similarly to RIP1, caspase 8 also bears both death-inducing and pro-survival roles. In parallel to its pro-apoptotic activity, it suppresses RIP3 signaling and is

required for T cell activation [63]. Thus, both caspase 8 and RIP1 are implicated in complex survival-death decision within the cell.

Below we will discuss the role of ROS in necroptosis and summarize recent research on the subject.

1.3.2. Mitochondria and mitochondrial ROS in necroptosis induction

Mitochondrial ROS have been regarded as an essential component of necroptosis induction, and many studies support this view. However, other studies have suggested that mitochondrial ROS are not needed for necroptosis induction **(Table 1.1)**, generating a debate on this matter [64].

In 1992, research by the Fiers group [65] showed that ROS generated at the mitochondrial respiratory chain determine the necrotic response of murine fibrosarcoma cell line L929 to TNFα treatment. Further evidence suggested that TNFα-mediated RIP1 activation leads to mitochondrial dysfunction, producing ROS that are involved in TNFα-induced necroptosis in L929 cells [66],

The molecular link between RIP1 activation and ROS production has been investigated by other studies conducted on murine cells, and ROS generation has been proposed to be RIP1-dependent [67], [48]. Other studies showed mitochondrial ROS accumulation and dysfunction leading to RIP1-dependent necroptosis, which was inhibited by ROS scavengers in murine cell lines [66],[68],[69]. However, suppressing ROS did not prevent necroptosis in other cell lines, such as the human Jurkat T cells, HT-29 and THP-1 cells [70], [71] [72] suggesting that the role of ROS in necroptosis is cell line-specific. Overall, data obtained using murine cell lines such as L929 are not always confirmed by studies in human cells, suggesting that these latter are potentially less dependent than murine cells on ROS contribution for necroptosis induction.

In accordance with the multiple roles of mitochondria related to cell death induction, it was shown that RIP1 and RIP3 can localize to these

organelles [72, 73]. Moreover, the mitochondrial permeability transition pore (mPTP) has been implicated in necroptosis induction by several studies, with particular focus on one of its components—CypD. It was shown that overexpression of CypD, but not ROS inhibition, prevented TNF-mediates necroptosis, in leukemia THP-1 cells [72]; moreover, CypD knockout mouse embryonic fibroblasts (MEFs) showed partial resistance to necroptosis induced by TNF-α, second mitochondrial-derived activator of caspases (SMAC) mimetics, and pan-caspase inhibitor z-VAD [71]. In addition, inhibition of CypD can block RIP1-RIP3-dependent necroptosis in zebrafish macrophages, in synergy with ceramide pathway blocking. In this study, necroptosis was shown to occur via TNFα-mediated mitochondrial ROS production. However, this was shown in the peculiar context of tuberculosis-infected macrophages, where bacterial components are implicated in ROS production [74].

In contrast to these studies, parkin-induced mitophagy was recently used to demonstrate that mitochondrial ROS are dispensable for necroptosis induction in TNFα-treated 3T3 MEFs [75]. Moreover, recent data suggested that MLKL can directly mediate rupture of the plasma membrane [56].

Overall, these findings indicate that different pathways to necroptosis may exist, with differential dependency on mitochondria and mitochondrial ROS according to cell type and conditions. Further studies examining these issues should take into account to directly compare multiple murine and human cell models under same experimental conditions.

Table 1.1 Evidence for and against a role of mitochondrial ROS in necroptosis.

	Role (Yes /No)	References	Finding	Cancer cell lines
Necroptosis	**N**	[72] [70, 71]	ROS scavenging does not prevent necroptosis in some cell lines.	THP-1, HT-29, U-937
	N	[76]	Non- mitochondrial ROS contributes to RIP1 dependent necroptosis	L929, MEFs
	N	[75]	Necroptosis occurs in cells where mitochondria are depleted through parkin-induced mitophagy	3T3-SA
	N	[56]	MLKL oligomers move from cytosol to plasma membrane and disrupt membrane integrity directly during necroptosis	HT-29
	Y	[65, 66, 69, 77 78]	Mitochondrial dysfunction and ROS in necroptotic cell death.	L929, RAW 264.7, MEFs
	Y	[71]	CypD deficient cells show partial resistance to necroptosis.	MEF
	Y	[74]	CypD and ceramide pathway inhibition blocked necrptosis	Macrophages
	Y	[72]	RIP1 can localize to mitochondrai	THP-1
	Y	[67]	RIP-dependent mitochondrially derived ROS.	L929

1.3.3. NOX and cytosolic ROS in necroptosis induction

An alternative source of ROS production is the plasma membrane associated NADPH oxidase 1 (NOX1) complex, which catalyzes the production of ROS from molecular oxygen [76], [79]. NOX1 is recruited by RIP1 in TNFα-induced necroptosis in L929 cells [76]. It was shown that TNFα stimulates NOX1 activity through complex with RIP1 partners such as TNFR1-associated death domain protein (TRADD), in L929, MEF and HeLa cells [76], [79]. However, NOX1 is unlikely to be the most important player in necroptosis induction in the investigated contexts. While knockdown of NOX1 was reported to rescue TNFα-mediated necroptosis in L929 cells [76], this rescue appears to be moderate. Moreover, another study

reported that silencing of NOX component $p22^{phos}$ did not prevent necroptosis in L929 cells [67].

Riboflavin kinase (RFK) is another component of the NOX complex and is known to associate with TNFR1 and TRADD after TNFα treatment. RFK binds TNFR1 to recruit the NADPH oxidase NOX1, NOX2, and $p22^{phos}$ in both mouse and human cells, but RIP1 is not directly related to the cell death pathway [79]. Finally, NOX4 was shown to promote cisplatin-induced nephrotoxicity by increasing ROS-mediated RIP1-dependent necroptosis in human HK2 cells and *in vivo* mouse models [80].

Taken together, these data suggest that while NOX enzymes play a role in necroptosis induction in different models, their contribution appears to be partial and does not exclude mitochondrial ROS involvement.

Iron is another important player in cytosolic ROS generation that is independent from enzymatic activities and relies on Fenton reactions. Iron can be found in cells in its divalent or trivalent form (i.e., reduced or oxidized) and is essential for the functioning of several enzymes involved in ROS production and detoxification, such as LOX, cytochrome p450, catalase, peroxidases and PRX. The majority of cellular iron is bound to proteins, such as ferritin and transferrin, or is coordinated in complexes, such as in heme. However, some free or loosely coordinated iron (so called “labile” iron) is also present in the cell and constitutes a highly redox-active iron pool. Redox-active iron is toxic to cells and must be carefully transported and accumulated in an inactive form.

Iron chelators were shown to rescue cells from necroptosis [65] and changes in iron transport and storage can also impact necroptotic cells death. For example, Xie et al. [81] showed that L929 cells with reduced levels of the iron storage protein ferritin are more resistant to TNFα-induced increases in the labile iron pool, ROS production, and ROS-dependent necroptosis. Interestingly, they also reported that elevation of the labile iron pool failed in RIP1-deficient MEFs after TNFα treatment. Moreover, it was proposed

that TNFα may stimulate production of ROS through c-Jun N-terminal kinase 1 (JNK1), which mediates the degradation of ferritin and thus the elevation in labile iron pool levels [82].

1.3.4. ROS, RIP and the positive feedback loop

Recent research is attempting to answer whether ROS are involved in a positive feedback loop regulating the formation of the necrosome [83]. RIP1 autophosphorylation of Ser161 has a crucial role in TNFα-induced necroptosis [84], [85]. Shindo et al. [69] showed that butylated hydroxyanisole can decrease necroptosis in MEFs without affecting RIP phosphorylation, thus arguing for a role of ROS downstream of RIP1. However, it was recently shown that three crucial RIP1 cysteines (257, 268, and 586) are required for sensing ROS prior to activation, supporting the notion that mitochondrial ROS promotes RIP1 autophosphorylation of Ser161 [86]. In another study, treatment with TNFα and Smac mimetic stimulated ROS production in Jurkat cells, which in turn stabilized the necrosome in a positive feedback loop [87]. Moreover, lipid peroxides can stimulate necroptosis in erythroid cells lacking glutathione peroxidase 4 (GPX4) independently of TNFα treatment by acting upstream on the necrosome [88]. Overall, the exact role of ROS upstream of RIP and of the necrosome is still elusive and should be clarified by further studies.

1.3.5. Role of lipid peroxidation in necroptosis

Lipid peroxides, have been also shown to contribute to necroptosis execution. ROS can target polyunsaturated fatty acids (PUFAs) in the cellular membranes to produce toxic aldehydes such as 4-hydroxynonenal (HNE), malondialdehyde (MDA) and acrolein [89], [90], [91]. Moreover, TNFα was shown to stimulate the production of not only mitochondrial ROS but also of lipid peroxides through the activation of phospholipase A2 and liberation of arachidonic acid [92, 93], which can then be

targeted by LOX. This process eventually contributes to lysosomal membrane permeabilization (LMP) and the execution of necroptosis [94]. Moreover, GPX4 was recently found to be required for preventing RIP3-dependent necroptosis in erythoid precursor cells by avoiding lipidic ROS accumulation [88], supporting the importance of lipidic ROS in necroptosis in this cell type. Of note, GPX4 plays also a role in protecting macrophages from gasdermin-D (GSDMD)-mediated pyroptosis, [95] highlighting the fundamental importance of this enzyme in cell survival. In cancer cells however, GPX4 appears to be mainly implicated in ferroptosis induction.

1.4. Redox cancer therapy

The understanding of ROS mechanisms supported the development of two parallel anticancer strategies based on ROS modulation, the use of antioxidants for cancer prevention and the use of ROS inducers to exacerbate oxidative stress to lead cancer cells to death [27, 96]. The second strategy represents the main mechanism of action of some current anticancer approaches, such as radio- and photodynamic therapy [97]. These therapies induce an intense and sudden burst of ROS, which cancer cells are unable to buffer, leading to cell death. Some clinically used chemotherapeutics have also been shown to induce cellular ROS. While chemotherapy-induced ROS in healthy cells have been linked to several side effects [98, 99, 100], ROS induction has been reported to occur also in cancer cells, and in some context to participate to the anticancer activity of chemotherapy [23, 24, 101].

As many cancer cells develop resistance to apoptosis, ROS eliciting this cell death pathway may not be sufficient to kill all cancer cells. The possibility of using molecules exacerbating ROS and eliciting necroptosis or ferroptosis is a promising scenario for ROS-based cancer therapies, especially for treating resistant cancers. Therefore, the list of natural and synthetic molecules with these interesting properties is increasing **(Table 1.2)**.

Table 1.2. Molecules inducing necroptosis in cancer cells

Necroptosis inducers	Clinical use/ clinical trials (www.clinicaltrials.gov)	Activity	Cancer cell line	References
Shikonin	no	Inhibitors of tumor specific pyruvate kinase M2 (PKM2)	K7, U2OS, Human multiple myeloma, MDA-MB-468, CNE-2Z, MCF-7, A549, U937, K562, HL60	86, 102, 103, 104, 105, 106, 107
β-Lapachone (ARQ761)	Clinical trials for treatment of several cancers types	Inhibitor of NQO1. RIP1 dependent ROS generation, HMGB1 release, NAD+↓, ATP↓	SK-Hep1	25
Eupomatenoid-5	no	Necroptotic morphology, ROS generation	786-0	108
Obatoclax (GX15-070)	Acute myeloid leukemia, Phase I/Ⅱ trial in chronic lymphocytic leukemia, Hodgkin's lymphoma, small cell lung cancer.	Targets Bcl-2, Bcl-X_L, Bcl-w and Mcl-1. Interaction of p62 with RIP1-RIP3-FADD Inhibited by Necrostatin-1	Rhabdomyosarcom, acute lymphoblastic leukemia, pral squamous cell carcinoma	53, 109, 110
Staurosporine	Clinical trials for treatment of	Inhibited by Necrostain-1,	Rat astrocytes, U937, Raji	111, 112, 113

	refractory neoplasms, acute myeloid leukemia.	Inhibited by Necrosulfonamide		
Cisplatin	Clinical trials for treatment of several cancers types	RIP1-RIP3-MLKL dependent, CypD-mediated mPTP opening event	L929, OVCAR4, SKOV3, HT-29, HeLa, HK-2, A549	[114, 115, 116, 117]
FTY720	Clinical trials for acute stroke, Rett's syndrome, Multiple sclerosis, Renal insufficiency	RIP1-RIP3 interaction, ROS-JNK-p53 signaling pathway	Human glioblastoma, A549	[118, 119]
Neoalbaconol	no	RIP1 dependent MLKL phosphorylation, ROS production, ATP↓	C666-1, HK1	[120, 121]
Tanshinone IIA	Acute myocardial infraction, Pulmonary hypertension, Cardiovascular disease, Polycystic ovary syndrome	RIP1-RIP3-MLKL mediated necroptosis. FLIP down-regulation	HepG2	[122]
Taurolidine	Clinical trials for solid cancer treatment	ROS generation	Glioma, pancreatic cancer and fibrosarcoma	[123, 124, 125]
BAY-87-2243	Phase I trial for	Complex I	BRAF mutant	[126]

	treatment of advanced malignancies	inhibitor	melanoma cancer cells	

1.4.1. Necroptosis inducers as redox cancer therapeutics

Over the last decade, several natural and synthetic compounds have been shown to induce necroptosis in specific cancer cell types. In this growing list we find novel compounds as well as well-known molecules in anticancer research, such as cisplatin and staurosporine [111, 114].

The natural compound shikonin was one of the first natural necroptosis inducers to be discovered. Shikonin is a naphthoquinone derived from the herbal plant *Lithospermum erythrorhizon* used in traditional Chinese medicine [127] and was shown to inhibit pyruvate kinase M2 (PKM2) [128]. Recently, shikonin was shown to induce necroptosis by increasing intracellular ROS levels in several cancer cell lines, such as U-937 [107], K-562 and HL-60 [102] and T-47D breast cancer cells [129]. A series of natural shikonin analogues has also been reported to induce necroptosis [130].

The natural compound β-lapachone (3,4-dihydro-2,2-dimethyl-2H-naphtho[1,2-b]pyran-5–6-dione) is derived from the bark of the lapacho tree. β-lapachone is an ortho-naphthoquinone shown to inhibit the enzymatic activity of NAD(P)H quinine oxidoreductase 1 (NQO1) [131]; NQO1 is highly upregulated in most human solid tumor [132], [133], [134]. Evidence supports that β-lapachone induces necroptosis through ROS production and the activation of a RIP1-PARP1-AIF dependent pathway in human hepatocellular carcinoma cells [135].

Eupomatenoid-5 (eup-5) is a neolignan isolated from *Piper regnellii* leaves. A recent investigation suggested that eup-5 treatment induces necroptosis in the kidney cancer cell line 786-0 by enhancing mitochondrial ROS generation [108]. Obatoclax (GX15-070) is a small molecule indole bipyrrole compound that targets B-cell lymphoma 2 (Bcl-2),

Bcl-X_L, Bcl-w, and myeloid cell leukemia 1 (Mcl-1) [136], [137], [138], [53]. GX15-070 was shown to induce necroptosis through mitochondrial ROS accumulation and mitochondrial membrane depolarization in oral squamous cell carcinoma cells, rhabdomyosarcoma, and acute lymphoblastic leukemia [110], [53], [109].

FTY720 (2-amino-2-[2-(4-octylphenyl)ethyl]propane-1,3-diol; Fingolimod) is a synthetic sphingosine analogue of myriocin, a compound produced by a fungal metabolite and used in traditional Chinese medicine [139]. FTY720 was shown to induce RIP1-dependent necroptosis in lung cancer cells [119]. Furthermore, FTY720 activates ROS-JNK-p53 loop to induce apoptosis, necroptosis and autophagy in human glioma cells [118].

Taurolidine (bis (1,1- dioxoperhydro-1,2,4-thiadizinyl-4) methane) is derived from the amino acid taurine [140]. Taurolidine induced necroptosis via ROS production in cultured tumor cell lines, such as glioma cells, fibrosarcoma cells, and pancreatic cancer [123, 124, 125]

Recent research has also been showed that LGH00168 induces excessive ROS production in mitochondria, matrix metalloproteinase loss, and lysosomal membrane permeabilization in A549 cells as a necroptosis inducer [141]. Polyphenon E is a standardized green tea extract, which was shown to induce necroptosis by causing ER enlargement and increasing the production of intracellular ROS in prostate carcinoma cells [142].

Redox active selenium compounds have also been investigated regarding cell death induction in a species-specific manner. Selenite has toxic effects associated with ROS production, deregulation of thiols homeostasis, mitochondria dysfunction and mitochondria DNA condensation. Selenite-treated Hela cells exhibited partially inhibited cell death by Nec-1, suggesting the involvement of necroptosis [143], [144]. Finally, the multi-kinase inhibitor sorafenib in combination with the histone deacetylase inhibitor Givinostat (ITF2357) induces caspase-independent cell death, which was rescued by pretreatment with Nec-1, and is associated

with ROS production in Hodgkin's lymphoma [145].

1.5. Future directions

Many questions remain unanswered regarding the role of ROS in necroptosis. The context-specific involvement of mitochondrial and cytosolic ROS in necroptosis is one main research focus. Moreover, the precise final targets of ROS in both cell death forms have yet to be defined. Further research is needed to clarify the iron-dependent enzymatic activities responsible for ferroptosis. This type of cell death can also be accompanied by ER stress and eukaryotic translation initiation factor 2A (eIF2A) phosphorylation [146], which is recognized as marker of immunogenic cell death (ICD). Therefore, it would be interesting to investigate whether ferroptosis results in the release of danger associated molecular patterns, and to which extent it can eventually induce an anticancer immune response. Overall, the increasing understanding of the mechanisms underlying necroptosis and ferroptosis will benefit the advancement of redox cancer strategies and the discovery of new redox-active anticancer therapeutics.

Chapter 2.

TetrahydrobenzimidazoleTMQ0153 triggers apoptosis, autophagy and necroptosis crosstalk in chronic myeloid leukemia

.

2.1. Abstract

By comparing imatinib-sensitive and -resistant CML cell models, we investigated the molecular mechanisms by which tetrahydrobenzimidazole derivative TMQ0153 triggered caspase-dependent apoptosis at low concentrations accompanied by loss of mitochondrial membrane potential (MMP) and increase of cytosolic free Ca^{2+} levels. Interestingly, at higher concentrations, TMQ0153 induced necroptotic cell death with accumulation of ROS, both preventable by **N**-acetyl-L-cysteine (NAC) pretreatment. At necroptosis-inducing concentrations, we observed increased ROS and decreased ATP and GSH levels, concomitant with protective autophagy induction. Inhibitors such as bafilomycin A1 (baf-A1) and siRNA against beclin 1 abrogated autophagy, sensitized CML cells against TMQ0153 and enhanced necroptotic cell death. Importantly, TMQ153-induced necrosis led to cell surface exposure of calreticulin (CRT) and ERp57 as well as the release of extracellular ATP and high mobility group box (HMGB1) demonstrating the capacity of this compound to release immunogenic cell death (ICD) markers.. We validated the anti-cancer potential of TMQ0153 by *in vivo* inhibition of K562 microtumor formation in zebrafish. Taken together, our findings provide evidence that cellular stress and redox modulation by TMQ0153 concentration-dependently leads to different cell death modalities including controlled necrosis in CML cell models.

Keywords: Tetrahydrobenzimidazole; Metabolic stress; ROS; Cell death; Chronic myeloid leukemia

2.2. Introduction

Imatinib kills leukemic cells essentially *via* apoptosis but triggers primary or secondary resistance in approximately 20~30% of patients [147]. Second-generation tyrosine kinase inhibitors (TKIs) such as dasatinib and nilotinib re-activate apoptotic cell death induction [148, 149] in patients with imatinib resistance, however, *de novo* resistance against these TKIs were also reported [150].

Pharmacological agents that target BCR-ABL-independent molecular targets in CML by initiating non-apoptotic cell death may overcome both BCR-ABL- and apoptosis-related resistance mechanisms by targeting unrelated vulnerabilities of CML cells specifically related to oxidative and metabolic stress metabolism. Transformation of leukemic cells by Bcr-Abl is associated with metabolic alterations and increased reactive oxygen species (ROS) generation. In addition, ROS levels are tightly regulated in normal hematopoiesis but are chronically elevated in CML. Koptyra et al. showed that Bcr-Abl kinase stimulates ROS that cause oxidative DNA damage that results in the mutation of the kinase domain, leading to imatinib resistance[151]. In addition, Landry et al. [152] published that NADPH oxidase (Nox) activity affects intracellular ROS levels in Bcr-Abl positive cells, enhancing survival signaling. Therefore, targeting the altered metabolism and accumulation of ROS in CML cells could be of therapeutic interest as exacerbation of intracellular ROS levels constitute one of the main mechanisms of most chemo- and radio-therapeutic agents, eventually killing cells whether by apoptosis or programmed necrosis, depending on the metabolic status of the cell. Apoptosis and necroptosis are major cell death mechanisms that result in opposite immune responses [153]. Whereas apoptotic cell death was described to trigger immunotolerant responses, necroptotic cell death releases molecules that are related to inflammation and activate immune responses as implicated to ICD [154]. ICD is also triggered by stress response mechanisms such as autophagy, ROS and

endoplasmic reticulum (ER) stress and unfolded protein response (UPR) [155]. These stress responses further lead to cell death and DAMP release that are required for the activation of anticancer immune response by elevating immunogenicity of dying cells via ICD [156].

Controlled necrosis pathways cause a disequilibrium of the redox metabolome leading to depletion of ATP and glutathione (GSH) eventually triggering an energetic catastrophe. The crosstalk between the redox metabolism, autophagy and necroptosis offers an interesting therapeutic target in CML. Under oxidative and metabolic stress, autophagy becomes a cellular homeostasis mechanism that aims to re-establish the cellular energy balance, among others [157] allowing cell survival under stress conditions. Moreover, autophagy cross-talks with apoptosis at the level of caspase-8 degradation as well as with non-apoptotic or necrotic programmed cell death mechanisms [158].

We previously reported the synthesis of various tetrahydrobenzimidazole derivatives and investigated their cytotoxic potential against hematopoietic cancer cell lines. Among these derivatives, the quinone TMQ0153 exhibited significant differential cytotoxicity against cancer cells[159]. The usefulness of such quinones as inducers of non-canonical cell death in CML remains to be investigated.

2.3. Material and Methods

2.3.1. Compounds

Tetrahydrobenzimidazole (TMQ) 0153 was synthetized from p-benzoquinone as previously described [159]. 2′-deoxy-5-azacytidine (5-aza; A3656), 3-methyl adenine (3-MA; M9281), bafilomycin (baf-A1; #B1793), N-acetyl-L-cysteine (NAC; LAA21), thapsigargin (TSG; T9033), PP242 (P0037), shikonin (SHK; S7576) and necrostatin-1 (Nec-1; N9037) were purchased from Sigma–Aldrich (St. Louis, MO, USA). Chloroquine (CQ; NZ-51031-K200) was purchased from Enzo Life Science (ENZ-51031-0050). Tiron (SC-253669), Trolox (SC-200810), buthionine sulfoximine (BSO) (SC-200824) were obtained from Santa-Cruz Biotechnology (CA, USA). Hydrogen peroxide (H_2O_2) was purchased from Junsei Chemical (23150-0350) (Tokyo, Japan).

2.3.2. Cell culture

Chronic myeloid leukemia cell lines K562, KBM-5 and MEG01 were cultured in RPMI 1640 medium (Lonza, Walkersville, MD, USA) supplemented with 10 % (v/v) fetal calf serum (FCS; Biowest, Riverside, MO, USA) and 1 % (v/v) antibiotic–antimycotics (Lonza, Walkersville, MD, USA) at 37 °C and 5 % of CO_2. KBM-5 cells were kindly donated by Dr. Bharat B. Aggarwal. Imatinib-resistant KBM5-T315I cells (KBM5R) cells were obtained by sequentially increasing the concentration of imatinib from 0.25, to 1 μM imatinib in IMDM media supplemented with 10 % (v/v) fetal calf serum and 1 % (v/v) antibiotic–antimycotics [160]. Imatinib-resistant K562 (K562R) cells were a gift of the Catholic University of Seoul and cultured in RPMI 1640 medium with 25 mM HEPES (Lonza) supplemented with 10 % (v/v) FCS and 1 % (v/v) antibiotic-antimycotics. Both resistant cell types were cultured with 1 μM of imatinib and washed three times before each experiment. Lung carcinoma A549 and breast adenocarcinoma MCF7 cells were obtained from the American Type Culture Collection

(ATCC, Manassas, USA) were cultured in RPMI 1640 medium (Lonza, Walkersville, MD, USA) supplemented with 10 % (v/v) fetal calf serum (FCS; Biowest, Riverside, MO, USA) and 1 % (v/v) antibiotic–antimycotics (Lonza, Walkersville, MD, USA). Normal B lymphocyte RPMI-1788 from the Korean cell line Bank (KCLB, Seoul, South Korea) were cultured in RPMI 1640 medium (Lonza, Walkersville, MD, USA) supplemented with 10 % (v/v) fetal calf serum (FCS; Biowest, Riverside, MO, USA) and 1 % (v/v) antibiotic–antimycotics (Lonza, Walkersville, MD, USA) at 37 °C and 5 % of CO_2. All cells were cultured according to standard procedures. Peripheral blood mononuclear cells (PBMCs) were isolated by density gradient centrifugation using Ficoll-Hypaque (GE Healthcare, Roosendaal, The Netherlands) from freshly collected buffy coats as previously described [160, 161], obtained from healthy adult human volunteers (Red Cross, Luxembourg, Luxembourg) after ethical approval as well as written informed consent from each volunteer. After isolation, cells were incubated overnight at 2 x 10^6 cells/mL in RPMI 1640 (supplemented with 1% antibiotic–antimycotic and 10% FCS (BioWhittaker, Verviers, Belgium) at 37ºC and 5% CO_2 in a humidified atmosphere. The day after, cell concentration was adjusted at 1 x 10^6 cells/mL using the same fresh complete medium and then treated as indicated.

2.3.3. Cell viability and cell death assessment

A Trypan blue exclusion assay (Lonza) was used to assess cell viability and IC_{50} values were also calculated on data obtained from Trypan blue assay. The mode of cell death was determined and quantified after determination of the nuclear morphology was evaluated under fluorescence microscopy (Nikon Eclipse Ti-U, Nikon Instruments Korea, South Korea) after cell staining with 1 µg/mL Hoechst 33342 (Sigma-Aldrich,) and 1 µg/mL propidium iodide staining (Sigma-Aldrich). Caspase 3/7 activity was assessed by Caspase-Glo 3/7 Assay (Promega, Madison, WI, USA), and

intracellular ATP levels were measured using the CellTiter-Glo Luminescent Cell Viability Assay (Promega, Madison, WI, USA).

2.3.4. Colony formation Assays

Colony formation assays were performed as previously published [162].

2.3.5. Protein extraction and western blotting

Whole cell extracts were prepared using M-PER® (Thermofisher, R7007, Waltham, MA, USA) supplemented by 1x protease inhibitor cocktail (Complete EDTA-free; Roche, Basal, Switzerland) according to manufacturer's instructions. Western blots were performed using the following primary antibodies: anti-caspase 7 (9494S), anti-caspase 9 (9502S), anti-caspase 8 (9746), anti-PARP-1 (9542), anti-Mcl-1 (4572S), anti-LC3B (2775), anti-p62 (5114), anti-Beclin 1 (3738) and anti-RIP3 (#13526) from Cell Signaling (Danvers, MA, USA); anti-caspase 3 (sc-56053), anti-PARP-1 (C2-10; sc-53643) from Santa Cruz Biotechnology (CA, USA); anti-Bcl-xL (610212), anti-RIP1 (610458) from BD Pharmingen (San Jose, CA, USA); anti-beta actin (5441) from Sigma Aldrich. Bands were quantified using Image Quant TL (GE Healthcare, Pittsburgh, PA, USA).

2.3.6. Morphology analysis

For Giemsa staining, cells were spun onto a glass slide for 5 minutes at 800 *g* using a cytopad with caps (ELITech Biomedical Systems, USA). Cells were then fixed and stained with the Diff-Quik staining kit (Dade Behring S.A., USA) according to the manufacturer's protocol and pictures were taken under a microscope (Nikon Eclipse Ti-U, Nikon Instruments Korea, South Korea). A total of 50 cells were counted in one area, and three independent areas were counted for each set of three independent experiments.

2.3.7. Transmission electron microscopy

For transmission electron microscopy (TEM), 5 x 10^6 cells were pelleted and fixed in 2.5 % glutaraldehyde (Electron Microscopy Sciences, USA) diluted in 0.1 M sodium cacodylate buffer, pH 7.2 (Electron Microscopy Sciences, USA) overnight. Cells were then rinsed with sodium cacodylate buffer twice and post-fixed in 2 % osmium tetroxide for 2 h at room temperature. Samples were washed with distilled water and then stained with 0.5 % uranyl acetate at 4 ˚C for overnight. After 24 h, samples were dehydrated through a graded series of ethanol solutions to water followed by propylene oxide, and then infiltrated in 1:1 propylene oxide/Spurr's resin. Samples were kept overnight embedded in Spurr's resin, mounted in molds and left to polymerize in an oven at 56 ˚C for 48 h. Ultrathin sections (70–90 nm) were obtained with ultramicrotome, EM UC7 (Leica, Germany). Sections were stained with uranyl acetate and lead citrate and subsequently examined with a JEM1010 transmission electron microscope (JEOL, Japan).

2.3.8. Analyses of autophagic vesicles

For fluorescence microscopy analysis, 3 × 10^6 cells were stained with Cyto-ID® Green dye and Hoechst 33342, according to manufacturer's instructions (Enzo Life Science). Cells were observed by confocal microscopy (Leica TCS SP8, Germany). Segmentation of objects of interest was based on 31 parameters assessing color, texture and edge and was carried out in Ilastik, version 1.3.0 (https://www.ilastik.org/), developed by the European Molecular Biology Laboratory, Heidelberg [163]. Classifiers trained for these parameters on a set of representative images were then applied to batch process multiple images as described in Ilastik's user manual. Binary masks thus obtained were measured in FIJI [164] after applying a size filter to remove small size artefacts resulting from segmentation. Results were compared by Kruskal-Wallis test followed by Conover post-test further adjusted by the Benjamini-Hochberg FDR method

(www.astatsa.com). Overall, the number of images evaluated in the different groups was as follows: control group n=7, 4 h group n=7, 8 h group n=6, and PP242 treated group n=5.

2.3.9. Measurement of cytosolic calcium levels

Experiments were based on published procedures with modifications [165]. Cells were stained with 500 nM Fluo-3-AM (Thermo Fisher, R7007, Waltham, MA, USA) for 25 min at 37 °C. After 15 min at room temperature, cytosolic Ca^{2+} levels were assessed by flow cytometry (FACS Calibur, Becton Dickinson, San Jose, CA, USA) and data were recorded statistically (10,000 events/sample) using the CellQuest Pro software (BD, Biosciences). Data were analyzed using the Flow-Jo 8.8.7 software (Tree Star, Inc., Ashland, OR, USA) and results were expressed as mean fluorescence intensity (MFI).

2.3.10. Determination of the oxygen consumption rate

The oxygen consumption rate (OCR) was measured using a Seahorse XFp cell mito stress Assay (#103010-100, Agilent, USA) ran on a Seahorse XFp analyzer (Agilent, Yongsan-gu, Seoul) according to manufacturer's instructions. Briefly, cells were seeded at 200,000 cells per well and treated with TMQ0153 for 4 h in 175 µL medium. Before measurements, plates were equilibrated in a CO_2-free incubator at 37 °C for 1 h. Analysis were performed using 1.5 µM oligomycin, 0.5 µM carbonyl cyanide-4-(trifluoromethoxy)phenylhydrazone (FCCP), and 1 µM rotenone/antimycin A as indicated. Data were analyzed using the Seahorse XF Cell Mito stress rest report generator software (Agilent).

2.3.11. Transfections

Cells were transfected with 4.5 µL HiPerFect Transfection reagent (HPF; Qiagen, Germantown, MD, USA,) and 5 nM small interfering RNAs

(siRNAs; Qiagen) targeting the human beclin 1 (BCN-1) gene [NM003766; SiBEC-1_1: Hs_BECN1_1 (SI00055573) and 10 nM SiBEC-1_2: Hs_BECN1_2 (SI00055580)] or non-targeting (AllStars Negative Control siRNA) as described elsewhere [166]. 24 h post-transfection, medium was replaced, and cells were treated as indicated on figures.

2.3.12. Analysis of ROS, mitochondrial membrane potential, mitochondrial and lysosomal membrane mass

ROS levels were probed by using 10 μM on 2-7-dichlorodihydrofluorescein diacetate (H_2DCF-DA; Life Technologies, Carlsbad, USA) and analyzed by flow cytometry as previously described [167]. To monitor lysosomal mass, mitochondrial membrane potential and mitochondrial mass, cells were incubated at 37 °C for 30 min with 20 nM LysoTracker Red DND-99, 50 nM MitoTracker Red CMXRos (all from Molecular Probes, Invitrogen, Grand Island, NY, USA), respectively, and then analyzed by flow cytometry. Data were recorded statistically (10,000 events/sample) using the CellQuest Pro software. Data were analyzed using the Flow-Jo 8.8.7 software and results were expressed as mean fluorescence intensity (MFI).

2.3.13. Glutathione measurements

Reduced (GSH) and oxidized (GSSG) glutathione measurements were performed using the GSH/GSSG-Glo™ Assay kit (Promega, Madison, WI, USA) following the manufacturer's instructions. The luminescence signal was acquired using with a microplate luminometer Centro LB 960 and data were recorded using the MikroWin 2000 software package (Berthold Technologies, Bad Wildbad, Germany).

2.3.14. Quantification of HMGB1 release

Quantification of HMGB1 release in cell culture supernatants was assessed by enzyme-linked immunosorbent assay kit from Shino-Test-Corporation

(Jinbocho, Chiyoda-ku, Tokyo, Japan) according to the manufacturer's instructions. Absorbance data were collected using with a SpectraMax i3x microplate reader and data were recorded using the SoftMax Pro 7.0 software package (Sunnyvale, California, USA).

2.3.15. Measurement of extracellular ATP content

Extracellular ATP levels in the supernatant were assessed by the ENLITEN® ATP Assay system bioluminescence detection kit (Promega, Madison, WI, USA) following the manufacturer's protocol. Luminescence signal was acquired with a microplate luminometer Centro LB 960 and data were recorded using the MikroWin 2000 software package (Berthold Technologies, Bad Wildbad, Germany).

2.3.16. Analysis of calreticulin and ERp57 exposure

Cells were collected, washed twice with 1x PBS and fixed in 0.25 % paraformaldehyde in 1x PBS at 4 °C. After 5 min incubation, cells we washed twice in cold 1x PBS and incubated for 30 min at RT with anti-calreticulin (CRT; Ab2907, Abcam, Cambridge, UK) or ERp57 (Ab10287, Abcam) primary antibody diluted (1:50) in cold blocking buffer (2 % FCS in 1x PBS) and then incubated for 30 min with an Alexa488-conjugated monoclonal secondary antibody (A11034) diluted (1:50) in blocking buffer. Isotype-matched Alexa488-conjugated IgG antibodies were used as a control. Samples were then analyzed by flow cytometry. Data were recorded statistically (10,000 events/sample) using the CellQuest Pro software and analyzed using the Flow-Jo 8.8.7 software Results were expressed as mean fluorescence intensity (MFI). Samples were also analyzed by fluorescence microscopy (Nikon Eclipse Ti-U, Nikon Instruments Korea, South Korea).

2.3.17. Zebrafish toxicity assays and cancer cell xenografts

Cancer xenograft assays were performed as previously published [162]. Briefly,

200 K562 cells were stained for 2 h by 4 μM of Cell tracker CM-Dil dye (Invitrogen, Grand Island, NY, USA), then treated with TMQ0153 at indicated concentrations for 8 h and injected as described.

2.3.18. *In silico* drug-likeness properties

In silico drug-likeness properties according to Lipinski's 'rule-of-five' and other parameters for drug-likeness and oral bioavailability were evaluated by using the SCFBio website (www.scfbio-iitd.res.in/).

2.3.19. Bioinformatics analysis

The Microarray Innovations in Leukemia (MILE) dataset [168, 169] (GSE13159) was downloaded from the Gene Expression Omnibus repository [168] and normalized using the Robust Multichip Average (RMA) algorithm from the affy R package (version 1.62.0) [170]. Boxplot was generated using the *ggboxplot* function of the ggpubr R package (version 0.2.2) in R 3.6.0 [171] and RStudio [172].

2.3.20. Statistical analysis

Data are expressed as the mean ± S.D. and significance was estimated by using one-way or two-way ANOVA tests using Prism 8 software, GraphPad Software (La Jolla, CA, USA). Statistical significances were evaluated at **p**-values below 0.05 and represented by the following legend: *$\mathbf{p} \leq 0.05$, **$\mathbf{p} \leq 0.01$, ***$\mathbf{p} \leq 0.001$; posthoc analyses Dunnett; Sidak; Tukey). All histograms represent the mean ± SD of at least three independent experiments.

2.4. Results

2.4.1. Cellular uptake and drug-likeness potential of TMQ0153 in human leukemia cells

We first assessed the cellular uptake of auto-fluorescent TMQ0153 [173] by K562 cells using flow cytometry after 8 h, 24 h, 48 h and 72 h of treatment with concentrations up to 50 µM. Auto-fluorescence was detected in all three channels (FL1-530/30nm, FL2-585/42nm and FL3-670LP) up to 72 h **(Figure 2.1A)** and TMQ0153 (50 µM) was detected by confocal microscopy after 24 h of treatment when cell viability was 25% **(Figure 2.1B)** validating the time- and dose-dependent uptake of TMQ153. Moreover, TMQ153 follows Lipinski's 'rule of five' **(Table 2.1)** confirming its potential drug-likeness properties.

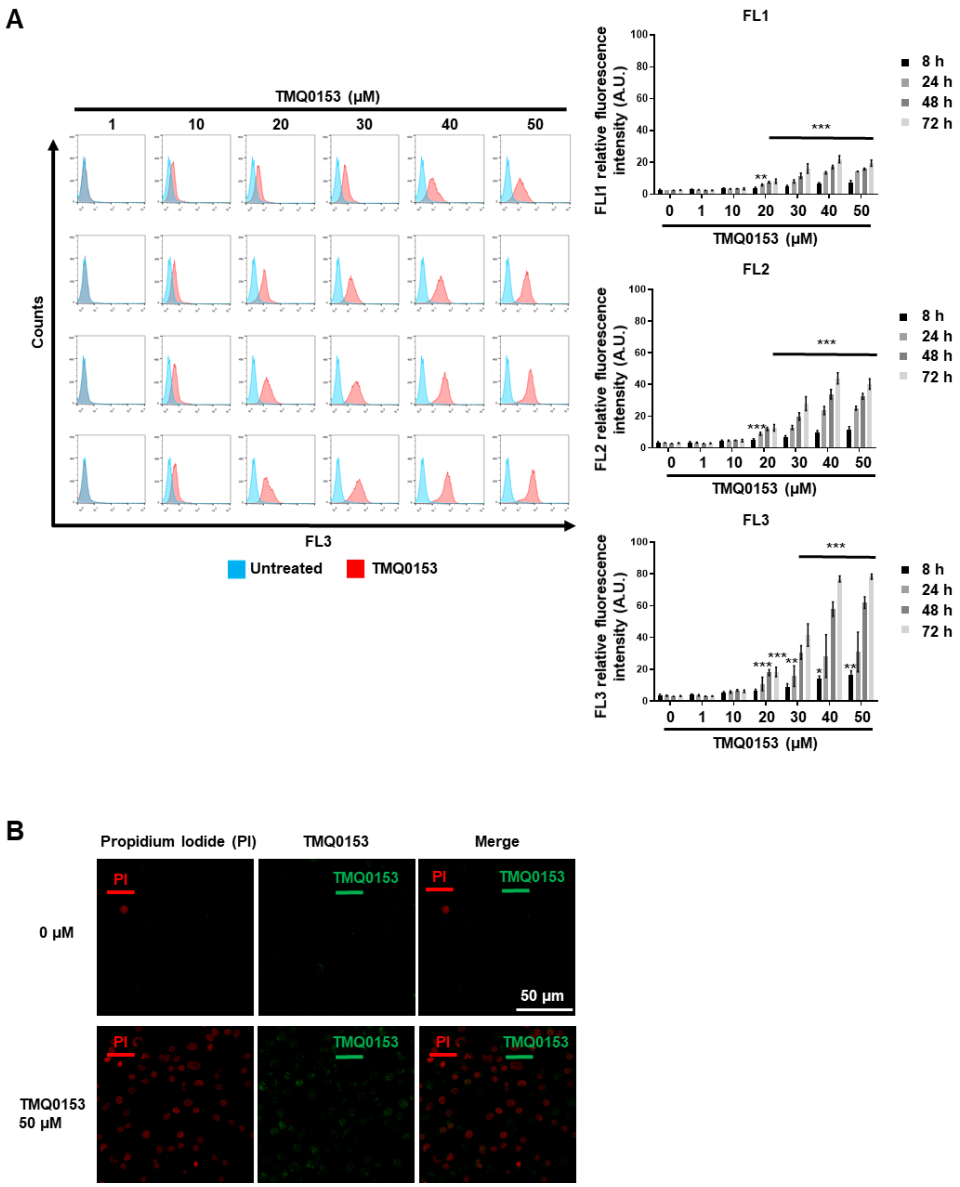

Figure 2.1 TMQ0153 is accumulated in the cytoplasm of K562 cells in a dose- and time-dependent manner (**A**) TMQ0153 showed a concentration- and time-dependent cellular uptake as quantified by flow cytometry using FL1, FL2 & FL3 channels with the strongest shift in the FL3 channel. Left panel: representative dot blots obtained with FL3 channel. Right panels: fluorescence intensity quantification on FL1, FL2 & FL3 channels represented as the mean (±S.D.) of three independent experiments. Statistical significance was assessed as *P<0.05, **P<0.01, ***P<0.001 compared to untreated cells. **(B)** After 24 h of treatment,

TMQ0153 localized in intra-cytoplasmic vesicular structures as observed by confocal microscopy. Two-way ANOVA (FACS); post hoc; Sidak's test.

Table 2.1 *In silico* prediction for the drug-likeness of TMQ0153 compared to hydroquinone based on Lipinski's 'rule of five' [174]

Drug-likeness parameter	Values		
	Theoretical	TMQ0153	Hydroquinone
MW (kDa)*	$180 \leq x \leq 500$	276.5	110
Hydrogen bond donors	≤ 5	1	2
Hydrogen bond acceptors	≤ 10	4	2
LogP (lipophilicity)	≤ 5	2.16	1.10
Molar refractivity	$40 \leq x \leq 130$	74.5	29.8

*MW: molecular weight

2.4.2. TMQ0153 inhibits cell viability, proliferation and colony formation capacity of drug-sensitive and -resistant cancer cells

We then validated the effect of TMQ0153 **(Figure 2.2A)** on imatinib-sensitive and -resistant K562 (K562R) KBM5, imatinib-resistant KBM5 (KBM5R) and MEG01 cells **(Figure 2.2B)**. We also compared the capacity of imatinib to induce cell death in K562 and K562R **(Figure 2.2C)**. Moreover, TMQ0153 decreased colony formation capacity of various imatinib-sensitive and resistant CML cell types **(Figure 2.2D)**. To extend our findings to an *in vivo* situation, zebrafish K562 xenograft formation was dose-dependently reduced by TMQ153, compared to controls **(Figure 2.2E)**. To assess for acute toxic side effects, no morphological alterations or toxicity of developing zebrafish larvae were observed at concentrations up to 50 μM, confirming the safety of this compound **(Figure 2.2F)**. We generalized our findings by using solid tumor cell lines lung A549, prostate PC3 and breast MCF7 cancer cells where TMQ153 also induced cell death **(Table 2.2)**. Next, we evaluated the selectivity of TMQ0153. We conducted viability assays on peripheral blood mononuclear cells (PBMCs) isolated

form healthy donors (**Figure 2.2G**). Viability of TMQ0153-treated PBMCs was dose-dependently impacted. We then evaluated the differential toxicity. After 72 h of treatment, TMQ0153 at 40 and 50 μM was 6.8 and 149-fold more selective to K562 cells compared to PBMCs, respectively (**Figure 2.2G**; **Table 2.3**). Considering the anti-cancer potential and differential toxicity, we selected CML models to further elucidate the mechanisms of action of TMQ0153.

Table 2.2 Effect of TMQ0153 on human cancer cell viability

Cancer model		**IC_{50} (μM)***			
Cancer type	**Cell line**	**8 h**	**24 h**	**48 h**	**72 h**
Blood	**K562**	>50	35.4±0.6	28.7±0.7	26.1±0.7
	K562R	>50	>50	>50	43.4±1.8
	KBM5	>50	>50	20.0±2.3	14.5±0.3
	KBM5R	>50	>50	20.7±2.7	15.1±0.8
	MEG01	>50	>50	45.3±2.7	28.8±1.7
Lung	**A549**	>50	>50	>50	>50
Prostate	**PC3**	>50	>50	>50	49.0±0.9
Breast	**MCF7**	>50	>50	>50	46.7±2.4

*IC_{50} values were calculated on data obtained from Trypan blue assays and represent the mean ± S.D. of three independent experiments.

R: Imatinib-resistant.

Table 2.3 Differential toxicity of TMQ0153 on PBMCs vs. K562.

	Fold Change		
Concentration (μM)	**24 h**	**48 h**	**72 h**
0	1.00	1.00	1.00
10	0.99	0.87	0.94
20	1.06	0.87	0.81
30	1.25	1.27	1.81
40	1.73	2.33	6.77
50	2.27	13.12	149.24

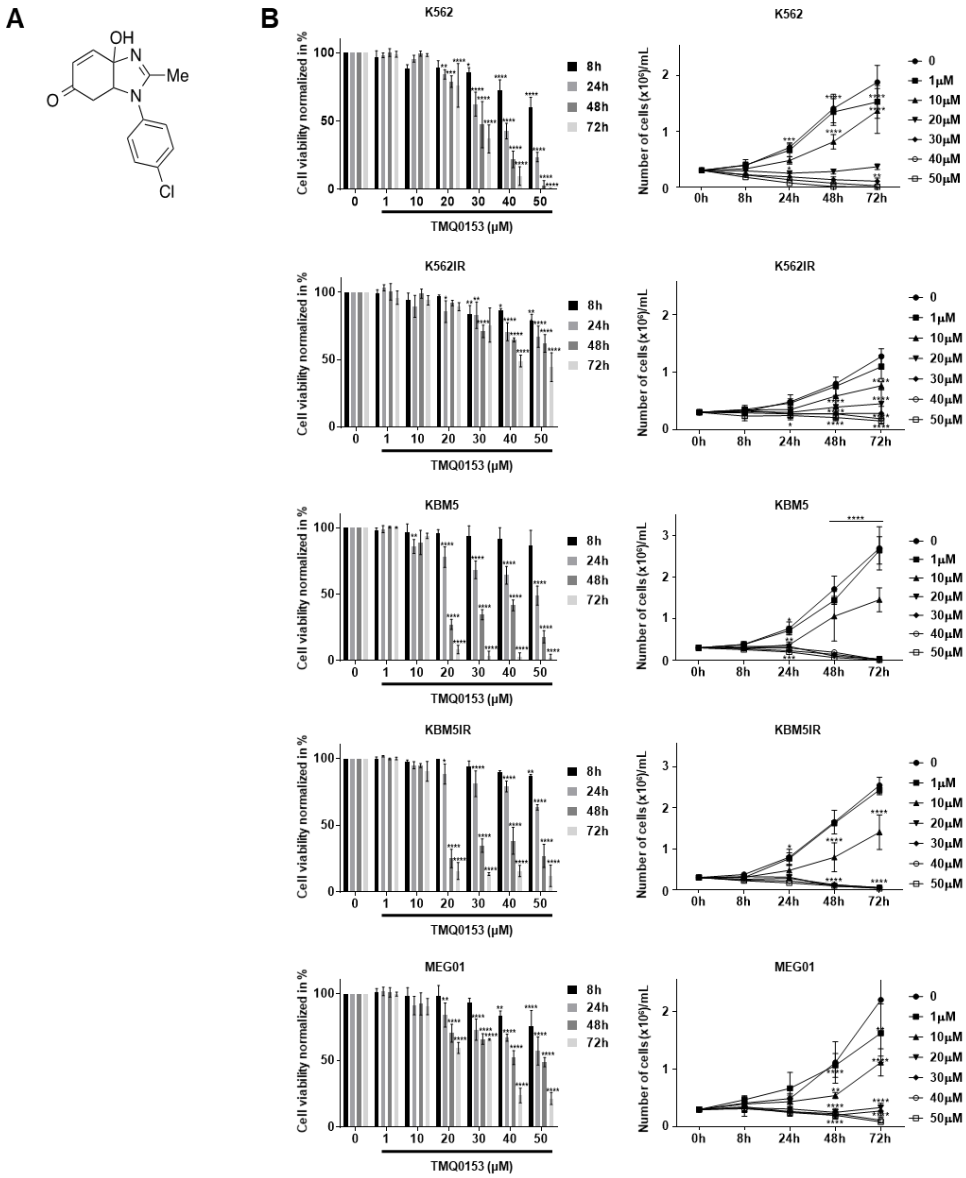
A
OH
N
Me
O
N
Cl
B
K562
Cell viability normalized in %
8h
24h
48h
72h
TMQ0153 (μM)
Number of cells (x10⁵)/mL
0
1μM
10μM
20μM
30μM
40μM
50μM
0h
8h
24h
48h
72h
K562IR
KBM5
KBM5IR
MEG01

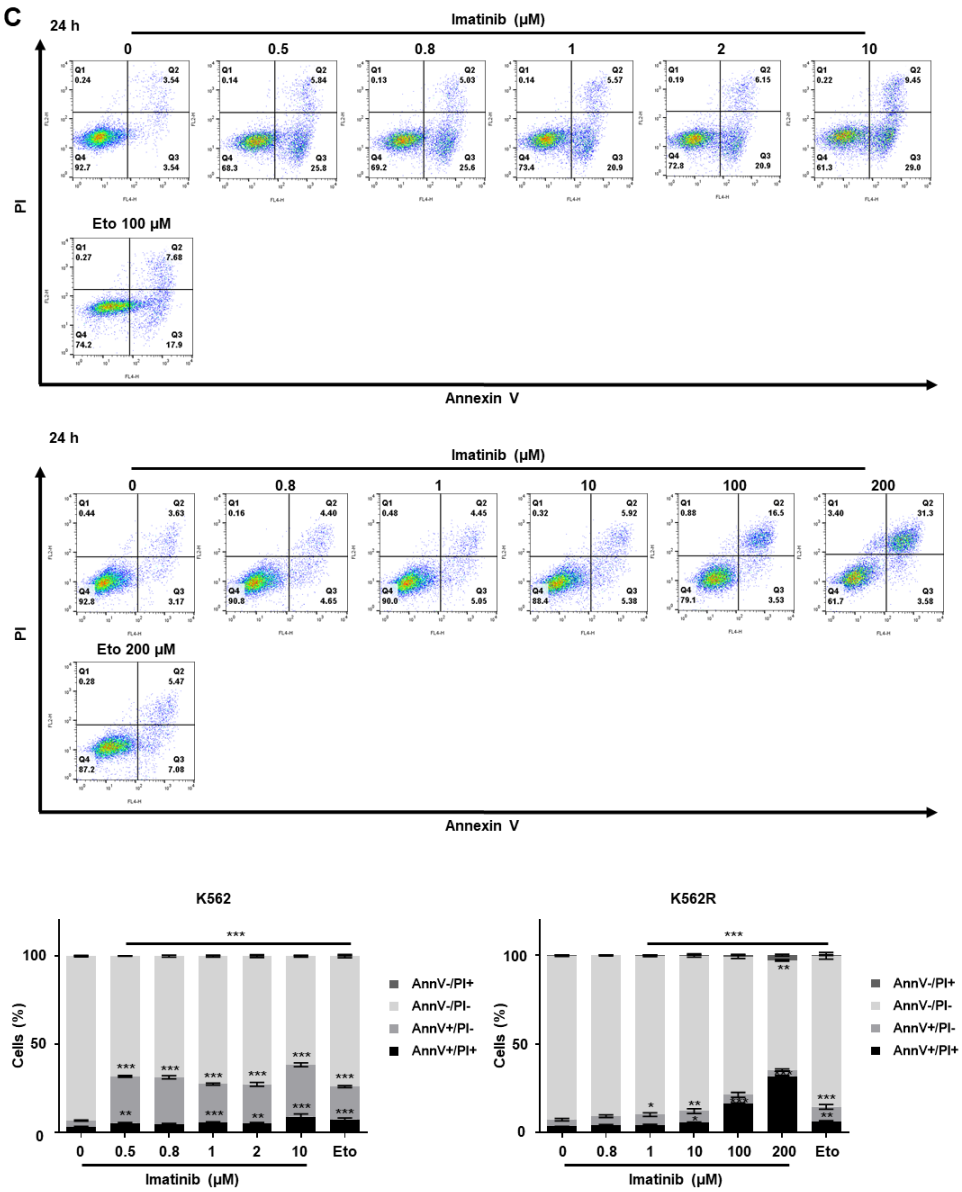
C
24 h
Imatinib (μM)
0
0.5
0.8
1
2
10
PI
Eto 100 μM
Annexin V
24 h
Imatinib (μM)
0
0.8
1
10
100
200
PI
Eto 200 μM
Annexin V
K562
Cells (%)
AnnV-/PI+
AnnV-/PI-
AnnV+/PI-
AnnV+/PI+
Imatinib (μM)
0
0.5
0.8
1
2
10
Eto
K562R
Cells (%)
AnnV-/PI+
AnnV-/PI-
AnnV+/PI-
AnnV+/PI+
Imatinib (μM)
0
0.8
1
10
100
200
Eto

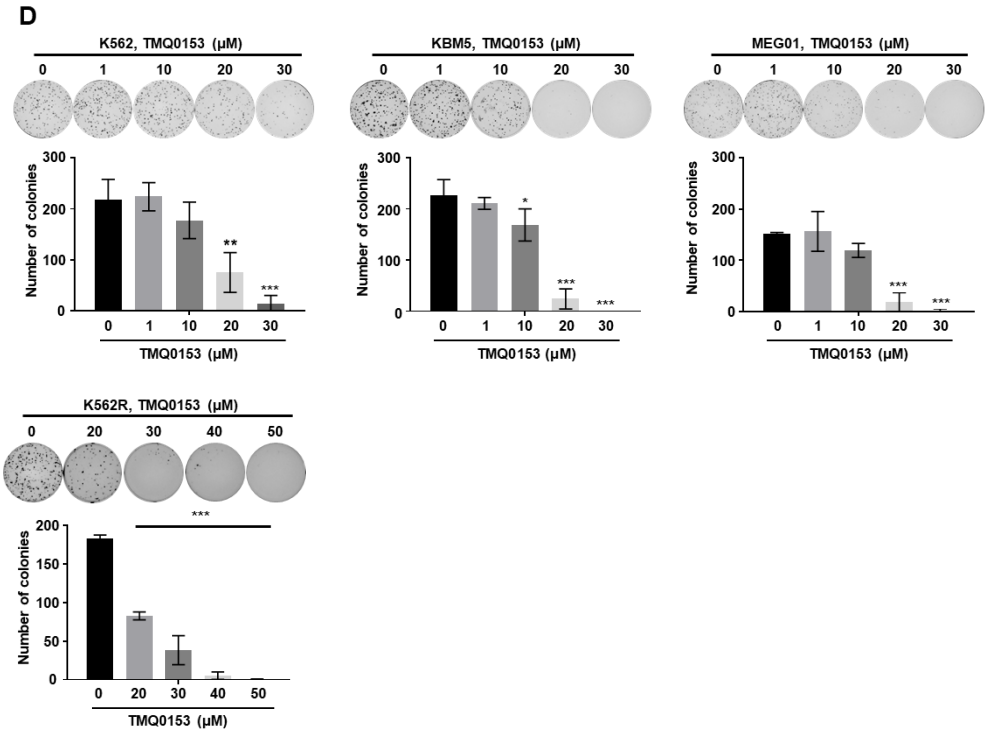
D
K562, TMQ0153 (μM)
0 1 10 20 30
Number of colonies
300
200
100
0
**
***
0 1 10 20 30
TMQ0153 (μM)
KBM5, TMQ0153 (μM)
0 1 10 20 30
Number of colonies
300
200
100
0
*
***
***
0 1 10 20 30
TMQ0153 (μM)
MEG01, TMQ0153 (μM)
0 1 10 20 30
Number of colonies
300
200
100
0
***
***
0 1 10 20 30
TMQ0153 (μM)
K562R, TMQ0153 (μM)
0 20 30 40 50
***
Number of colonies
200
150
100
50
0
0 20 30 40 50
TMQ0153 (μM)

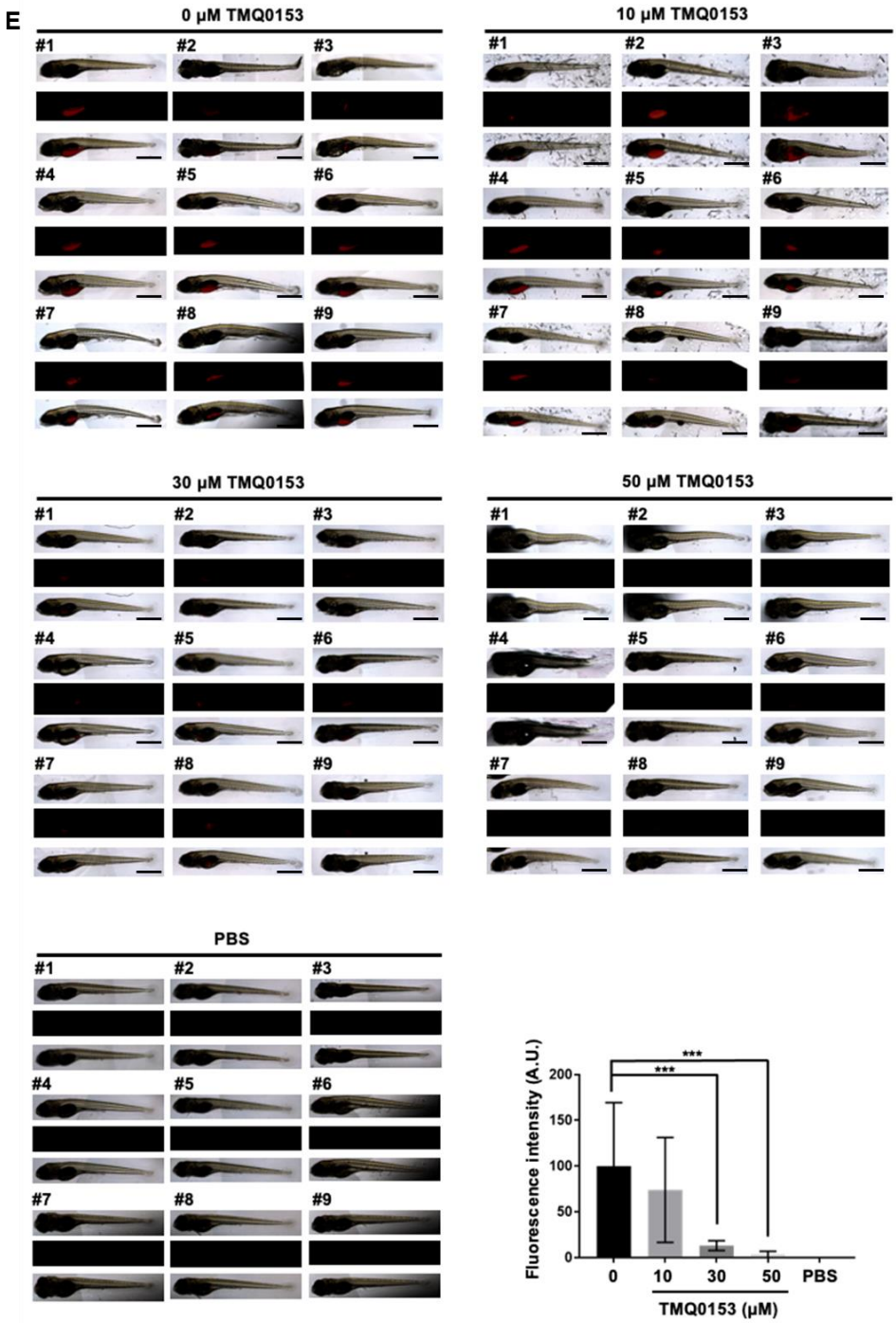
E
0 μM TMQ0153
10 μM TMQ0153
30 μM TMQ0153
50 μM TMQ0153
PBS
#1
#2
#3
#4
#5
#6
#7
#8
#9
Fluorescence intensity (A.U.)
200
150
100
50
0
***
***
0
10
30
50
PBS
TMQ0153 (μM)

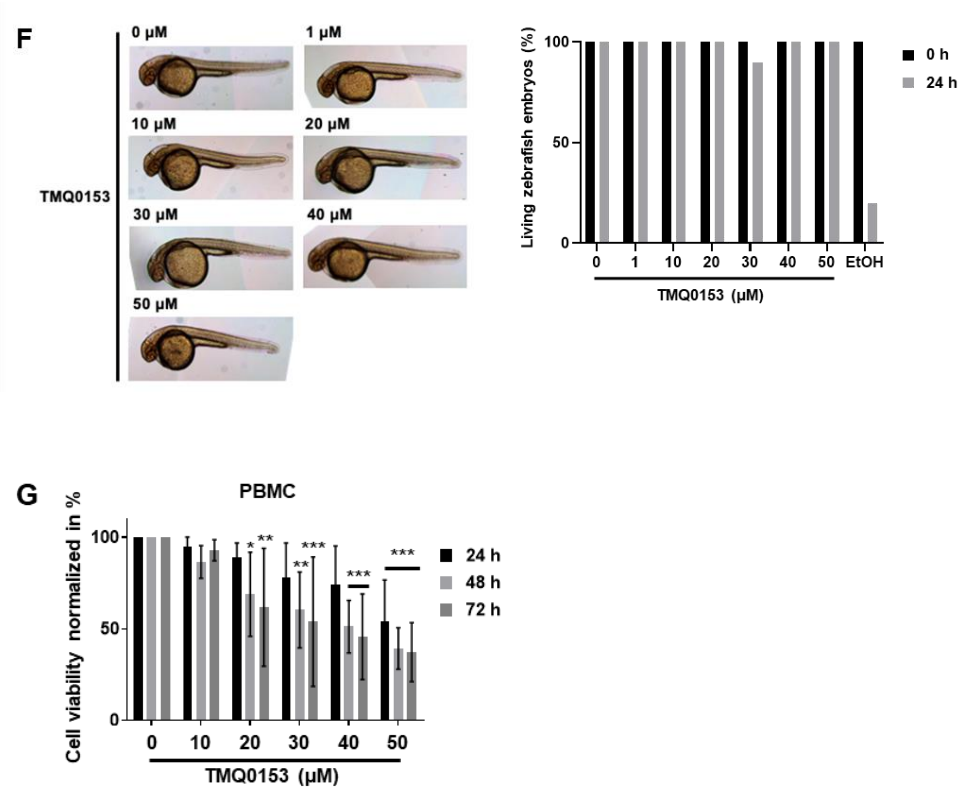

Figure 2.2 Effect of TMQ0153 on chronic myeloid leukemia cell viability (**A**) Chemical structure of TMQ0153. (**B**) Time- and dose-dependent effect of TMQ0153 on CML cells proliferation and viability (**C**) A dose-dependent comparison of imatinib-sensitive and -resistant K562 cells after 24 h. After 24 h of treatment, the type of cell death triggered by TMQ0153 was characterized by flow cytometry (FACS) after Annexin V APC/ propidium iodide (PI) staining. Pictures representative of three independent experiments (top panel) and the corresponding quantification (lower panel) are shown. (**D**) Inhibitory effect of increasing concentrations of TMQ0153 on the colony forming capacities of the indicated CML cell lines. Upper panel: pictures representative of three independent experiments. Lower panel: quantification of the colony numbers. (**E**) Inhibition of *in vivo* tumor forming ability of K562 cells xenografted in zebrafish by TMQ0153. Pictures [bright field (top), cell tracker CM-Dil dye-stained cells (middle), merge (bottom] of the 9 fishes used for each condition. PBS injection was used as a control for injection toxicity. The intensity of fluorescence was quantified and represented as the mean (±S.D.) of 9 fishes. Statistical significance was assessed as

***P<0.001 by One-way ANOVA; post hoc: Dunnett's test. (**F**) Acute toxicity assay on zebrafish embryos after 24 h of treatment with increasing concentrations of TMQ0153. Pictures are representative of 10 fishes used for each condition (left panel) and the corresponding quantification of viable embryos (right panel). Ethanol (EtOH, 70 %) as used as a positive control for toxicity. **(G)** Cytotoxicity of TMQ0153 on human peripheral blood mononuclear cells (PBMCs) by Trypan blue assay after 24, 48 and 72 h of treatment (PBMC data represent the mean (± S.D.) of five independent experiments). All data represent mean (±S.D.) of three independent experiments. Statistical significance was assessed as *P<0.05, **P<0.01, ***P<0.001 compared to untreated cells. Two-way ANOVA (Cell viability); post hoc: Sidak's test. One-way ANOVA (Colony formation, FACS); post hoc: Sidak's test. Two-way ANOVA (PBMC); post hoc: Dunnett's test.

2.4.3. TMQ0153 induces concentration-dependent differential cell death modalities

We then investigated the cell death mechanism induced by TMQ0153. Altogether, as shown in **Figure 2.3A-C**, apoptotic cell death was induced at concentrations up to 20 μM after 24 h, rescued by z-VAD pretreatment. Non-apoptotic, z-VAD-insensitive cell death was dose-dependently induced at concentrations over 30 μM after 8, 24, 48 and 72 h **(Figure 2.3A-G)** confirming a concentration-dependent induction of caspase-dependent and -independent cell death modalities in both K562 and K562R cells.

As shown in **Figure 2.3H**, after 24 h of treatment with TMQ0153, procaspase-9, -8 and -3 were significantly activated leading to PARP-1 cleavage. TMQ0153 treatment led also to a decrease of the anti-apoptotic proteins myeloid cell leukemia (Mcl)-1 and B-cell lymphoma-extra large (Bcl-xL) in a dose-dependent manner (**Figure 2.3I**). We confirmed our findings by measuring an increased caspase 3/7 activity following a treatment with up to 20 μM TMQ0153 for 24 h, which is abrogated in presence of z-VAD (**Figure 2.3J**).

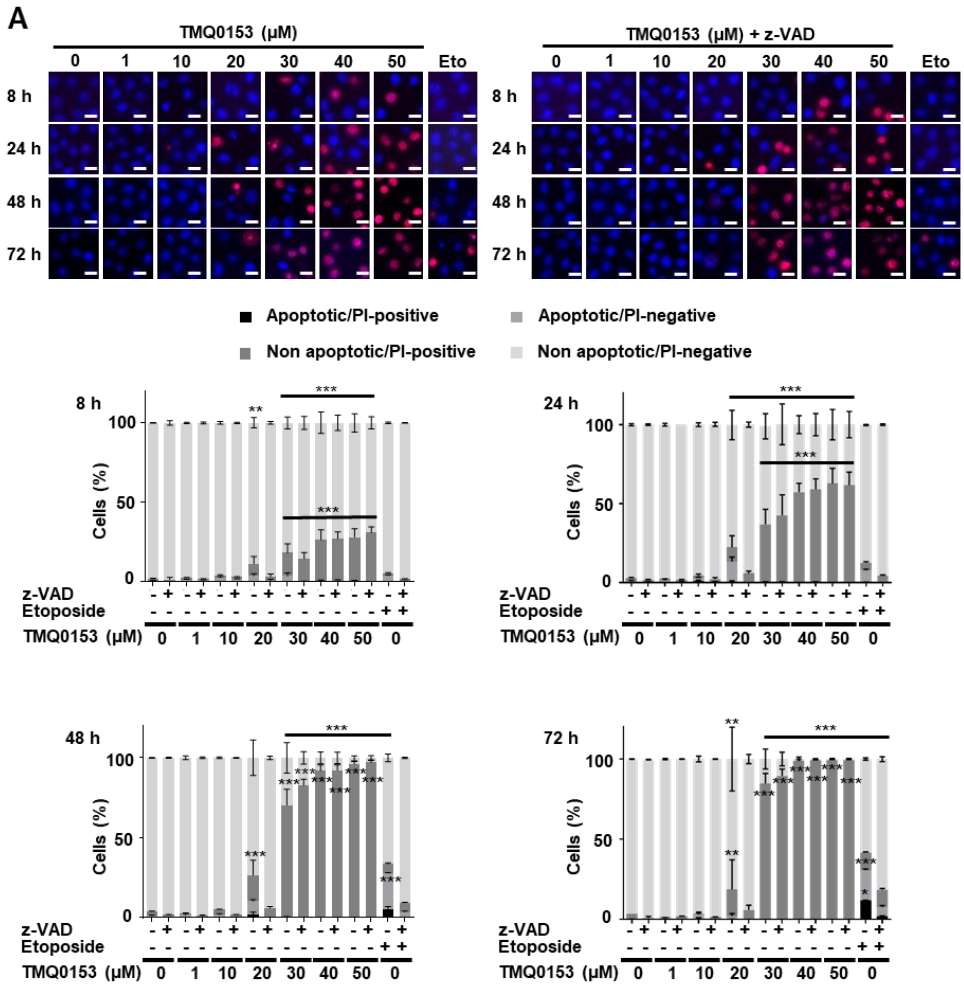
A
TMQ0153 (μM)
TMQ0153 (μM) + z-VAD
0 1 10 20 30 40 50 Eto
8 h
24 h
48 h
72 h
Apoptotic/PI-positive
Apoptotic/PI-negative
Non apoptotic/PI-positive
Non apoptotic/PI-negative
Cells (%)
z-VAD
Etoposide
TMQ0153 (μM)

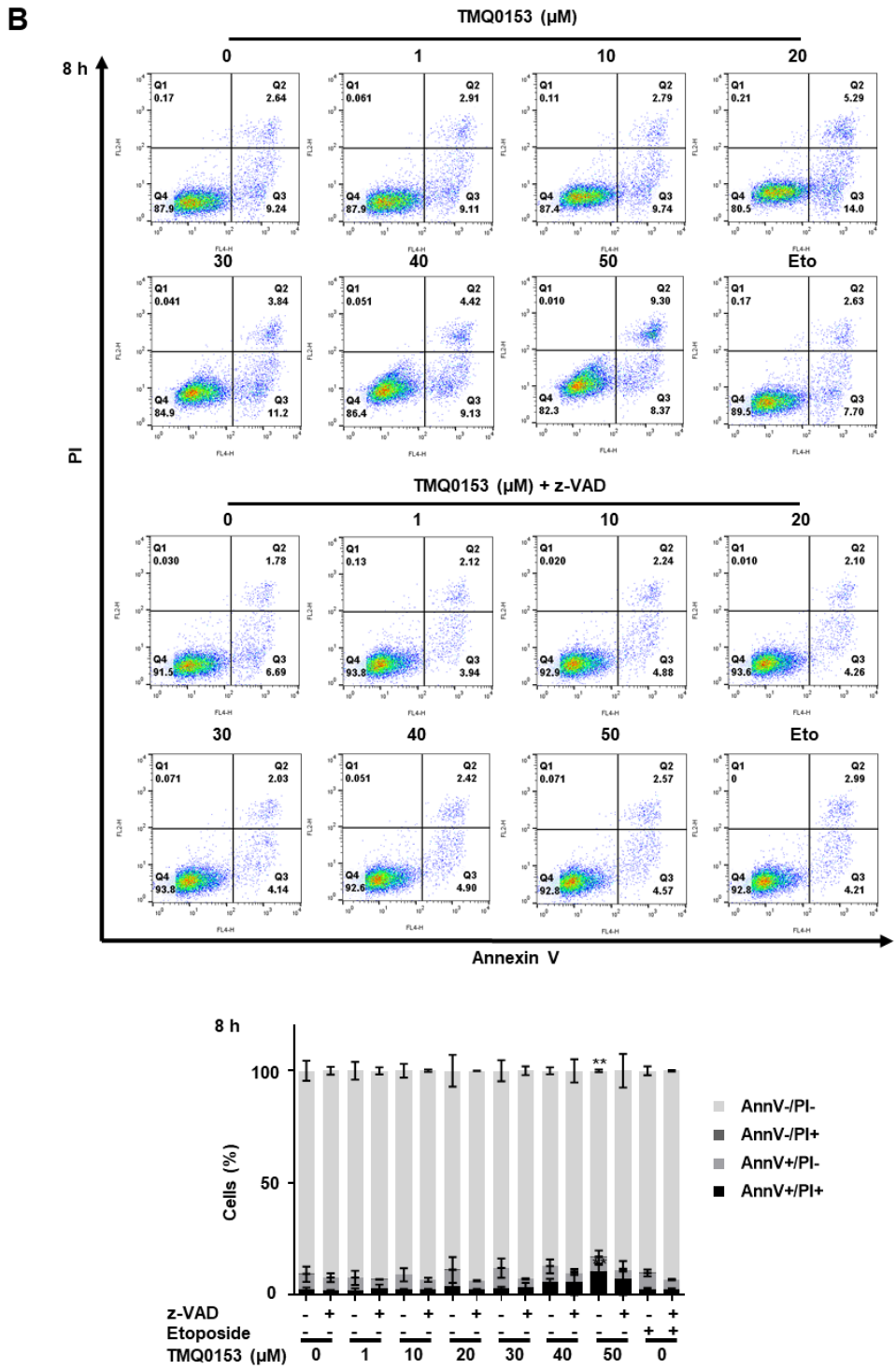
B
TMQ0153 (μM)
8 h
0
1
10
20
30
40
50
Eto
PI
TMQ0153 (μM) + z-VAD
Annexin V
8 h
Cells (%)
100
50
0
AnnV-/PI-
AnnV-/PI+
AnnV+/PI-
AnnV+/PI+
z-VAD
Etoposide
TMQ0153 (μM)

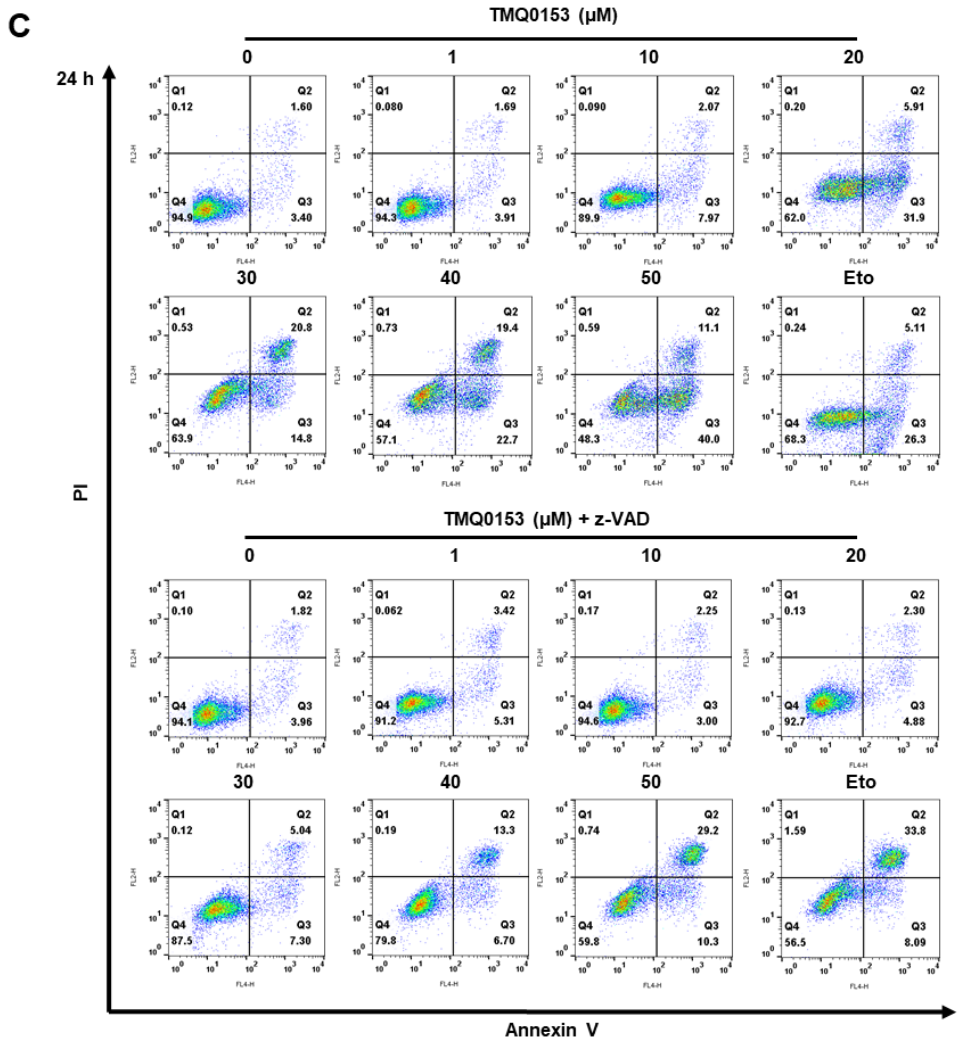
C
TMQ0153 (μM)
0
1
10
20
24 h
Q1 0.12
Q2 1.60
Q4 94.9
Q3 3.40
Q1 0.080
Q2 1.69
Q4 94.3
Q3 3.91
Q1 0.090
Q2 2.07
Q4 89.9
Q3 7.97
Q1 0.20
Q2 5.91
Q4 62.0
Q3 31.9
30
40
50
Eto
Q1 0.53
Q2 20.8
Q4 63.9
Q3 14.8
Q1 0.73
Q2 19.4
Q4 57.1
Q3 22.7
Q1 0.59
Q2 11.1
Q4 48.3
Q3 40.0
Q1 0.24
Q2 5.11
Q4 68.3
Q3 26.3
PI
TMQ0153 (μM) + z-VAD
0
1
10
20
Q1 0.10
Q2 1.82
Q4 94.1
Q3 3.96
Q1 0.062
Q2 3.42
Q4 91.2
Q3 5.31
Q1 0.17
Q2 2.25
Q4 94.6
Q3 3.00
Q1 0.13
Q2 2.30
Q4 92.7
Q3 4.88
30
40
50
Eto
Q1 0.12
Q2 5.04
Q4 87.5
Q3 7.30
Q1 0.19
Q2 13.3
Q4 79.8
Q3 6.70
Q1 0.74
Q2 29.2
Q4 59.8
Q3 10.3
Q1 1.59
Q2 33.8
Q4 56.5
Q3 8.09
Annexin V
24 h
100
50
0
Cells (%)
###
AnnV-/PI-
AnnV-/PI+
AnnV+/PI-
AnnV+/PI+
z-VAD
Etoposide
TMQ0153 (μM)
0
1
10
20
30
40
50
0

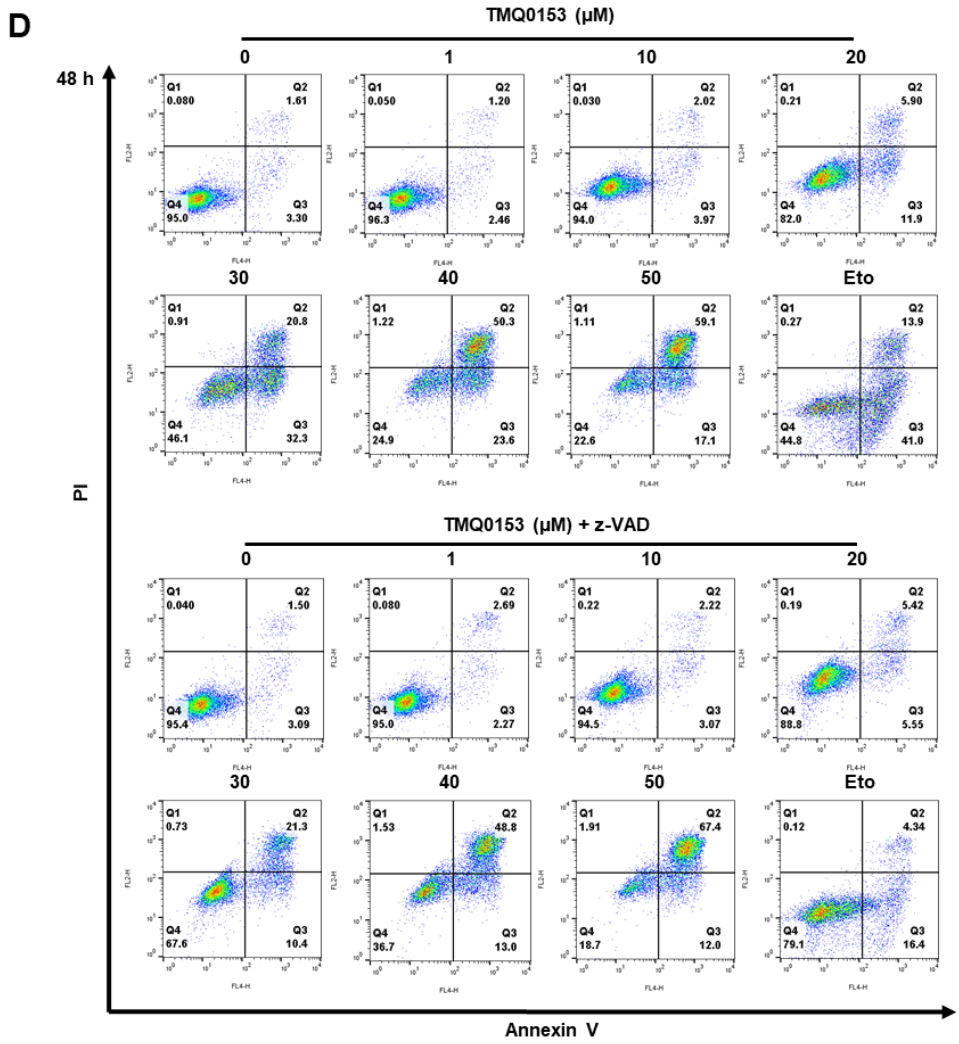
D
TMQ0153 (μM)
0
1
10
20
48 h
Q1 0.080
Q2 1.61
Q4 95.0
Q3 3.30
Q1 0.050
Q2 1.20
Q4 96.3
Q3 2.46
Q1 0.030
Q2 2.02
Q4 94.0
Q3 3.97
Q1 0.21
Q2 5.90
Q4 82.0
Q3 11.9
30
40
50
Eto
Q1 0.91
Q2 20.8
Q4 46.1
Q3 32.3
Q1 1.22
Q2 50.3
Q4 24.9
Q3 23.6
Q1 1.11
Q2 59.1
Q4 22.6
Q3 17.1
Q1 0.27
Q2 13.9
Q4 44.8
Q3 41.0
PI
TMQ0153 (μM) + z-VAD
Q1 0.040
Q2 1.50
Q4 95.4
Q3 3.09
Q1 0.080
Q2 2.69
Q4 95.0
Q3 2.27
Q1 0.22
Q2 2.22
Q4 94.5
Q3 3.07
Q1 0.19
Q2 5.42
Q4 88.8
Q3 5.55
Q1 0.73
Q2 21.3
Q4 67.6
Q3 10.4
Q1 1.53
Q2 48.8
Q4 36.7
Q3 13.0
Q1 1.91
Q2 67.4
Q4 18.7
Q3 12.0
Q1 0.12
Q2 4.34
Q4 79.1
Q3 16.4
Annexin V

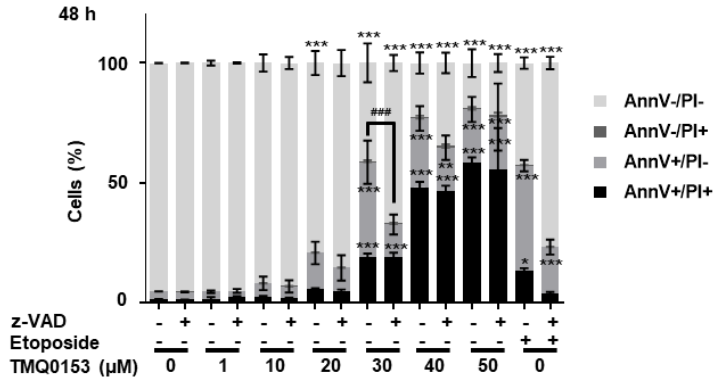
48 h
Cells (%)
100
50
0
###
AnnV-/PI-
AnnV-/PI+
AnnV+/PI-
AnnV+/PI+
z-VAD
Etoposide
TMQ0153 (μM)
0
1
10
20
30
40
50
0

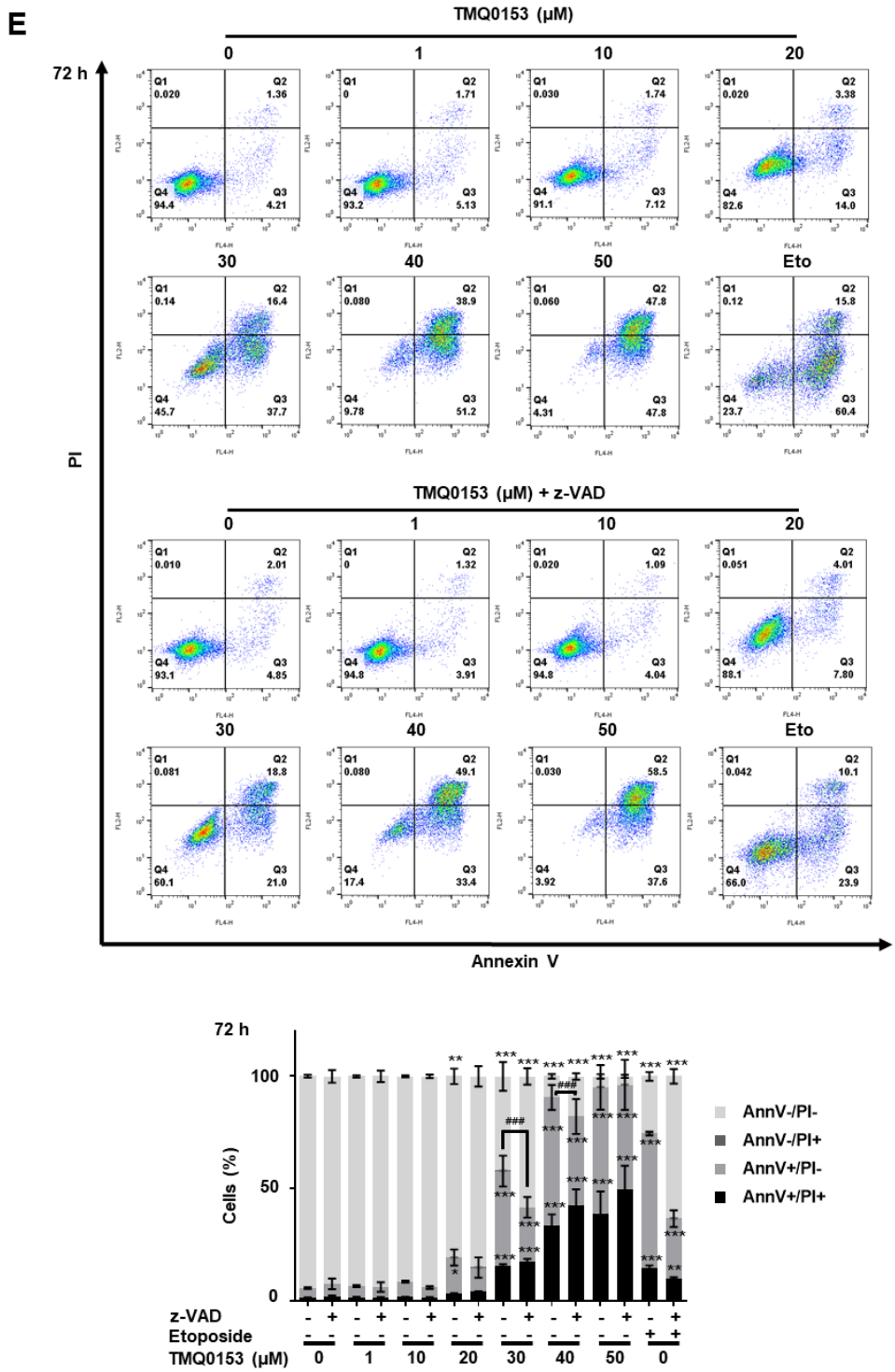
E
TMQ0153 (μM)
0
1
10
20
72 h
Q1 0.020
Q2 1.36
Q4 94.4
Q3 4.21
Q1 0
Q2 1.71
Q4 93.2
Q3 5.13
Q1 0.030
Q2 1.74
Q4 91.1
Q3 7.12
Q1 0.020
Q2 3.38
Q4 82.6
Q3 14.0
30
40
50
Eto
Q1 0.14
Q2 16.4
Q4 45.7
Q3 37.7
Q1 0.080
Q2 38.9
Q4 9.78
Q3 51.2
Q1 0.060
Q2 47.8
Q4 4.31
Q3 47.8
Q1 0.12
Q2 15.8
Q4 23.7
Q3 60.4
PI
TMQ0153 (μM) + z-VAD
0
1
10
20
Q1 0.010
Q2 2.01
Q4 93.1
Q3 4.85
Q1 0
Q2 1.32
Q4 94.8
Q3 3.91
Q1 0.020
Q2 1.09
Q4 94.8
Q3 4.04
Q1 0.051
Q2 4.01
Q4 88.1
Q3 7.80
30
40
50
Eto
Q1 0.081
Q2 18.8
Q4 60.1
Q3 21.0
Q1 0.080
Q2 49.1
Q4 17.4
Q3 33.4
Q1 0.030
Q2 58.5
Q4 3.92
Q3 37.6
Q1 0.042
Q2 10.1
Q4 66.0
Q3 23.9
Annexin V
72 h
Cells (%)
100
50
0
AnnV-/PI-
AnnV-/PI+
AnnV+/PI-
AnnV+/PI+
z-VAD
Etoposide
TMQ0153 (μM)
0
1
10
20
30
40
50
0

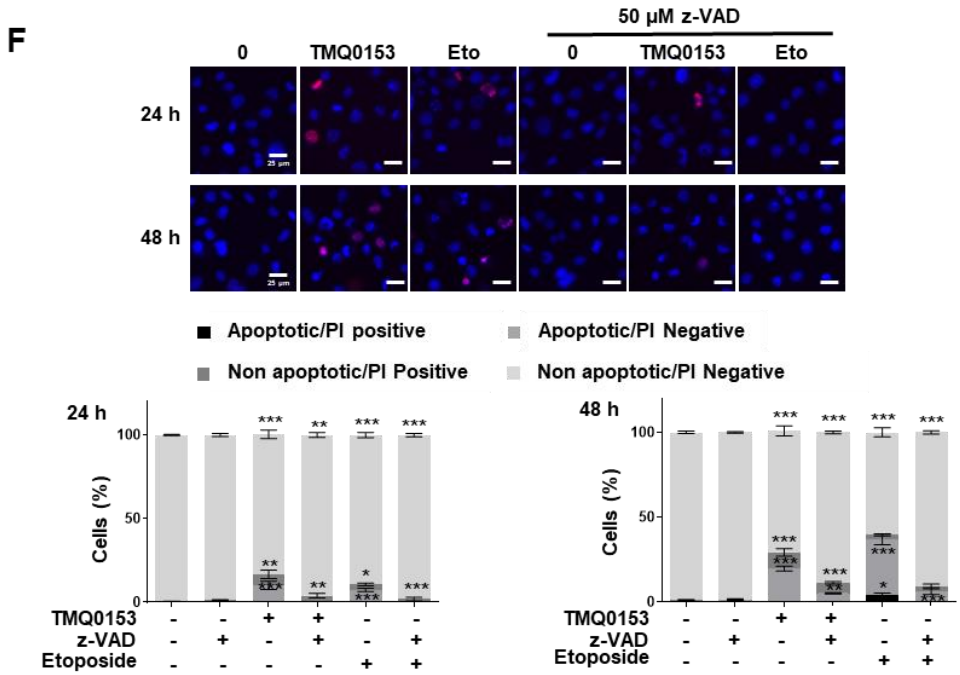
F
50 μM z-VAD
0
TMQ0153
Eto
0
TMQ0153
Eto
24 h
48 h
Apoptotic/PI positive
Apoptotic/PI Negative
Non apoptotic/PI Positive
Non apoptotic/PI Negative
24 h
48 h
Cells (%)
100
50
0
TMQ0153
z-VAD
Etoposide

G

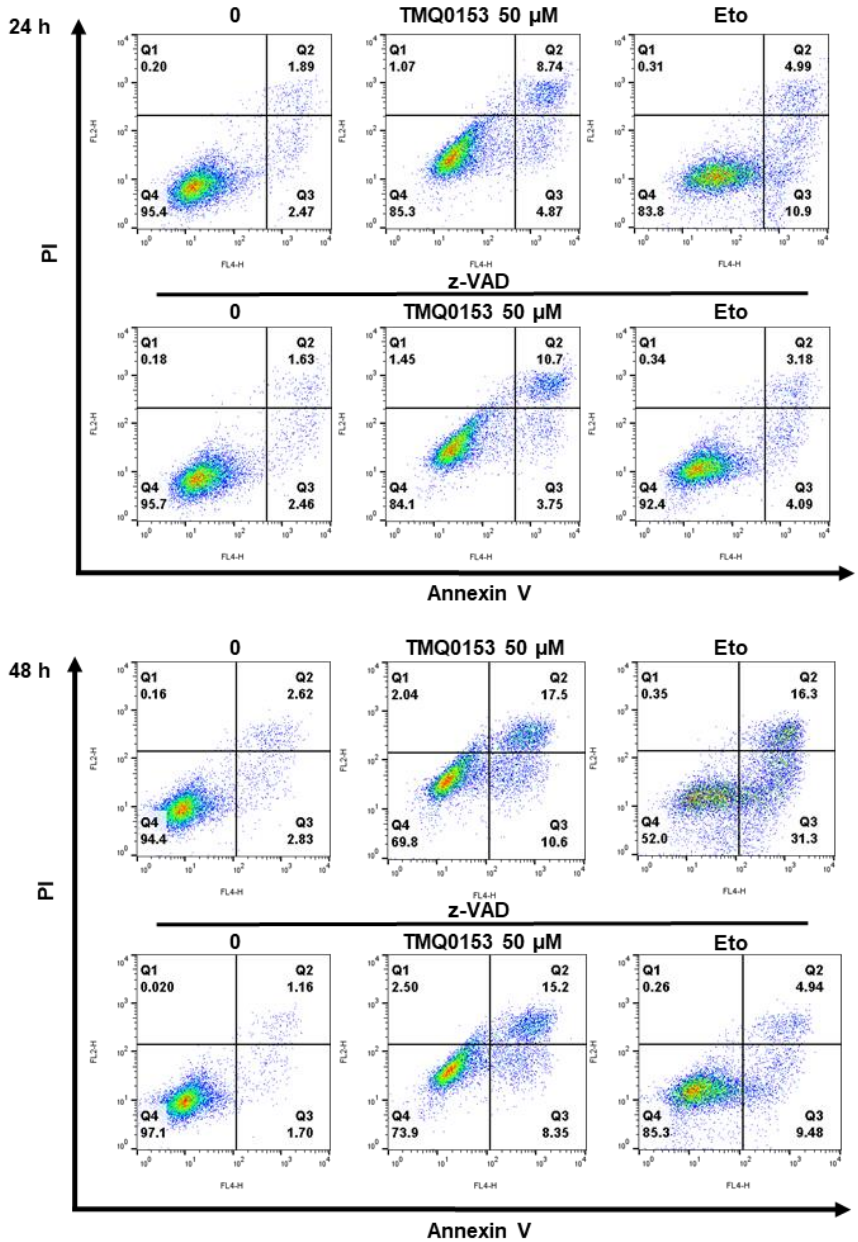
24 h
0
TMQ0153 50 μM
Eto
Q1 0.20
Q2 1.89
Q4 95.4
Q3 2.47
Q1 1.07
Q2 8.74
Q4 85.3
Q3 4.87
Q1 0.31
Q2 4.99
Q4 83.8
Q3 10.9
z-VAD
Q1 0.18
Q2 1.63
Q4 95.7
Q3 2.46
Q1 1.45
Q2 10.7
Q4 84.1
Q3 3.75
Q1 0.34
Q2 3.18
Q4 92.4
Q3 4.09
PI
Annexin V
48 h
Q1 0.16
Q2 2.62
Q4 94.4
Q3 2.83
Q1 2.04
Q2 17.5
Q4 69.8
Q3 10.6
Q1 0.35
Q2 16.3
Q4 52.0
Q3 31.3
Q1 0.020
Q2 1.16
Q4 97.1
Q3 1.70
Q1 2.50
Q2 15.2
Q4 73.9
Q3 8.35
Q1 0.26
Q2 4.94
Q4 85.3
Q3 9.48

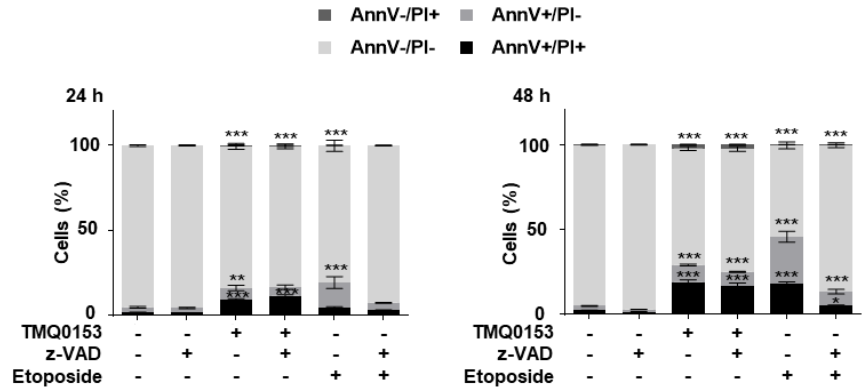
AnnV-/PI+
AnnV+/PI-
AnnV-/PI-
AnnV+/PI+
24 h
48 h
Cells (%)
100
50
0
TMQ0153
z-VAD
Etoposide

H

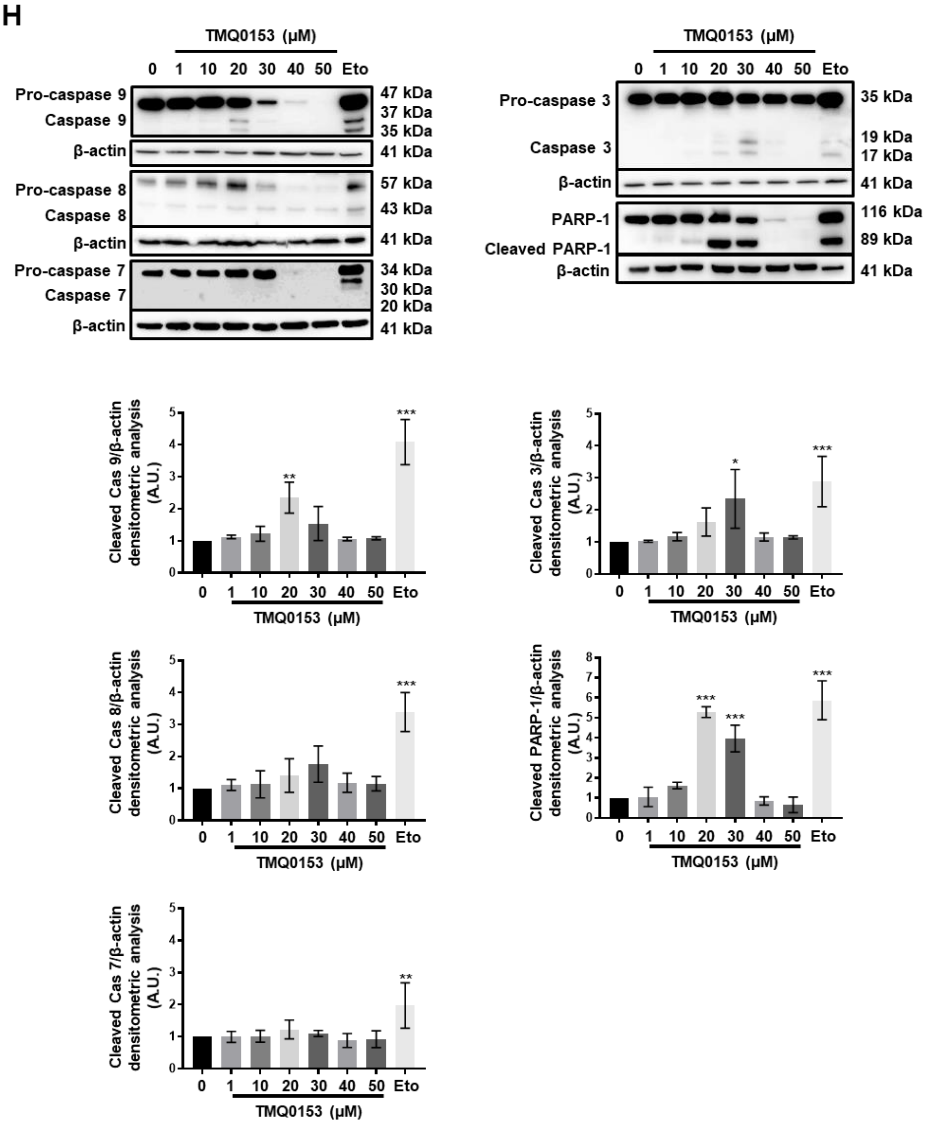
TMQ0153 (μM)
0 1 10 20 30 40 50 Eto
Pro-caspase 9
Caspase 9
β-actin
Pro-caspase 8
Caspase 8
Pro-caspase 7
Caspase 7
Pro-caspase 3
Caspase 3
PARP-1
Cleaved PARP-1
47 kDa
37 kDa
35 kDa
41 kDa
57 kDa
43 kDa
34 kDa
30 kDa
20 kDa
19 kDa
17 kDa
116 kDa
89 kDa
Cleaved Cas 9/β-actin densitometric analysis (A.U.)
Cleaved Cas 3/β-actin densitometric analysis (A.U.)
Cleaved Cas 8/β-actin densitometric analysis (A.U.)
Cleaved PARP-1/β-actin densitometric analysis (A.U.)
Cleaved Cas 7/β-actin densitometric analysis (A.U.)

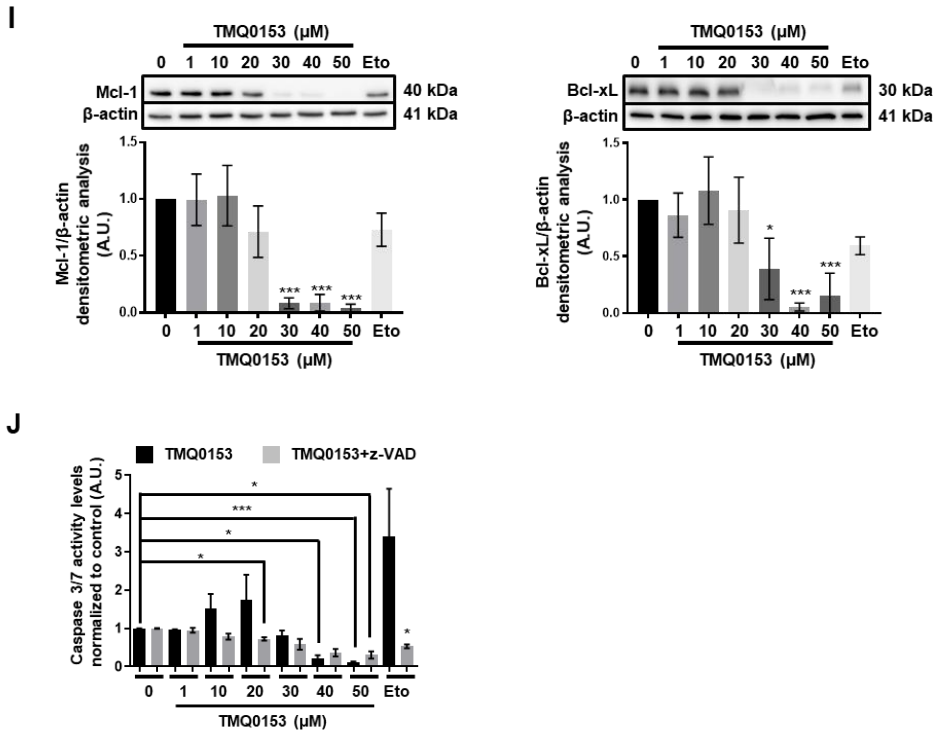

Figure 2.3 TMQ0153 triggered a concentration-dependent induction of caspase-dependent and independent non-apoptotic cell death in K562 cells (**A**) K562 cells were treated with various concentrations of TMQ0153 in presence or absence of the pan caspase inhibitor carbobenzoxy-valyl-alanyl-aspartyl-[O-methyl]-fluoromethylketone (z-VAD; 50 μM). (**A**) After 8, 24, 48 and 72 h of treatment the type of cell death triggered by TMQ0153 was characterized by fluorescence microscopy after Hoechst/ propidium iodide (PI) staining. Pictures representative of three independent experiments (top panel) and the corresponding quantification (lower panel) **(B-E)** After 8, 24, 48 and 72 h of treatment the type of cell death triggered by TMQ0153 was characterized by flow cytometry (FACS) in presence or absence of the pan-caspase inhibitor z-VAD (50 μM) after Annexin V APC/propidium iodide (PI) staining. Etoposide (Eto; 200 μM, 24 h) was used as a positive control for apoptosis induction. Pictures representative of three independent experiments (top panel) and the corresponding quantification (lower panel). **(F)** Characterization of the type of cell death induced by 50 μM TMQ0153 on K562R by nuclear morphology analysis after 24 and 48 h. Etoposide (Eto; 200 μM, 24 h) was used as a positive control for apoptosis induction. **(G)** Characterization of the type of cell death induced by 50 μM TMQ0153 on K562R

by FACS after 24h and 48h. Etoposide (Eto; 200 µM, 24 h) was used as a positive control for apoptosis induction. **(H)** Analysis of caspase and poly [ADP-ribose] polymerase **(**PARP)-1 cleavage by western blot after 24 h of treatment **(I)** Effect of 24 h of treatment on Mcl-1 and Bcl-xL protein expression levels (top panels) and the corresponding quantifications (middle and lower panels). (**H-I**) β–actin was used as loading control. **(J**) Quantification of caspase- 3/7 activity levels after 24 h of treatment. Etoposide (Eto; 100 µM, 24 h) was used as a positive control for apoptosis induction. All pictures are representative of three independent experiments and graphs represent the mean (±S.D.) of three independent experiments. Statistical significance was assessed as *P<0.05, **P<0.01, ***P<0.001 compared to untreated cells. Two-way ANOVA (microscopy analysis, FACS); post hoc: Sidak's test. One-way ANOVA (caspase-3/7 assay); post hoc: Tukey's test. One-way ANOVA (western blot quantification); post hoc: Dunnett's test.

2.4.4. TMQ0153 activates necrostatin-1 sensitive necroptotic cell death

We then investigated the mechanisms involved in TMQ0153-mediated non-apoptotic cell death at higher concentrations (*i.e.* from 30 µM) after 8 and 24 h in K562 cells. We pre-treated K562 cells with the RIP1 inhibitor Nec-1 to assess for induction of cell death by necroptosis. Briefly, we confirmed that Nec-1 had no effect on apoptosis at lower concentrations after 24 h in K562 cells (*i.e.* up to 20 µM) by TMQ0153 treatment. Results are shown in the **Figure 2.4A**, TMQ0153 induced over 50 % of non-apoptotic, PI positive cells after 24 h of treatment with 50 µM. Nec-1 pretreatment significantly prevented non-apoptotic cell death induction between 30-50 µM after 24 h, compared to shikonin, used as a positive control (**Figure 2.4B**). These results indicated that TMQ0153 induced cell death in K562 cells *via* the necroptotic cell death pathway.

Necroptosis is known to be accompanied by a modulation of intracellular ATP, increased expression levels of RIP1 and the appearance of a non-apoptotic cleavage fragment of PARP-1 between 50 and 75 kDa [70].

Our results showed a significant decrease of intracellular ATP levels after 4, 8, 16 and 24 h at 30 µM TMQ0153 compared to 20 µM **(Figure 2.4C).** Western blot results confirmed that TMQ0153-treated cells presented increased RIP1 expression levels and this expression was inhibited by a Nec-1 pretreatment. Also, the differentially cleaved necrotic PARP1 fragment revealed by the C2-10 antibody, supported that TMQ0153 induced necrotic cell death at 30 µM after 24 h of treatment **(Figure 2.4D)**. Besides, we observed a concomitant accumulation of cytosolic Ca^{2+} levels at 30 and 50 µM TMQ0153 **(Figure 2.4E).** Hematopoietic cell lines largely lack RIP3 expression and this loss of RIP3 may reduce sensitivity against cytotoxic agents [175].

We then investigated the basal expression levels of RIP3 by western blot analysis in different cancer cell types with known RIP3 expression levels. As expected, RIP3 was silenced in K562, A549, PC3 and MCF7 cells **(Figure 2.4F).** We then treated K562 cells with the DNA hypomethylating agent 5-aza-2'-deoxycytidine (5-aza) at 1 µM for 6 days to re-express RIP3. As shown in **Figure 2.4G**, 5-aza treatments increased RIP3 protein expression levels. We then co-treated these cells with TMQ0153 to investigate potential sensitization. Results showed that TMQ0153 treatment of 5-aza-pretreated K562 cells led to significantly enhanced cell death levels (54 %) compared to TMQ0153 treatment alone (21 %). Overall, our results indicated that the cytotoxicity of TMQ0153 in K562 cells is mediated by necroptosis at higher concentration. In addition, a pretreatment with DNA hypomethylating agents like 5-aza may further potentialize the effect of TMQ0153 in CML devoid of RIP3.

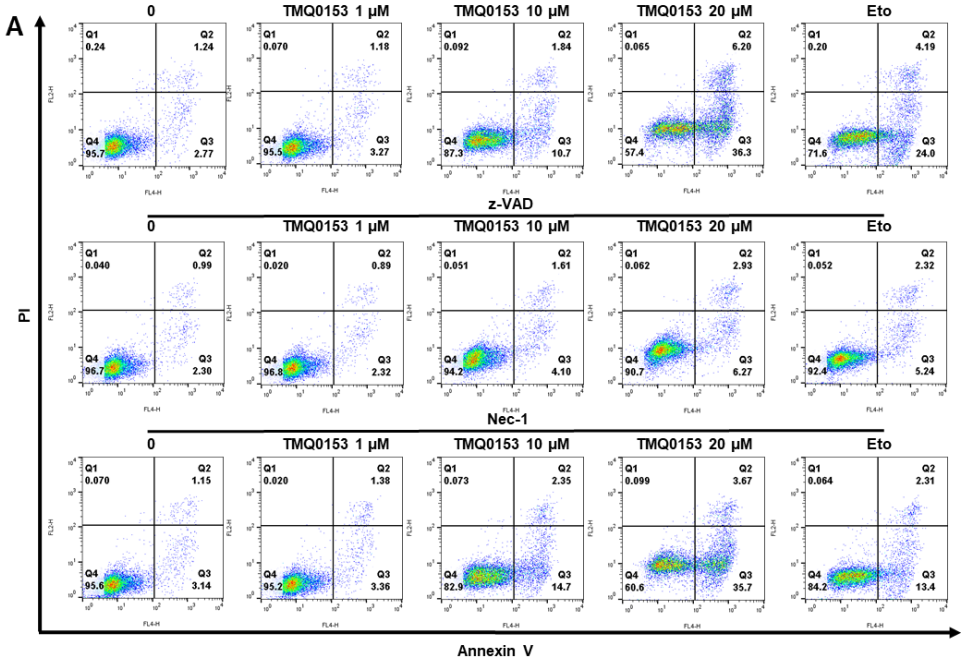
A
0
TMQ0153 1 μM
TMQ0153 10 μM
TMQ0153 20 μM
Eto
z-VAD
Nec-1
PI
Annexin V
Q1 0.24
Q2 1.24
Q4 95.7
Q3 2.77
Q1 0.070
Q2 1.18
Q4 95.5
Q3 3.27
Q1 0.092
Q2 1.84
Q4 87.3
Q3 10.7
Q1 0.065
Q2 6.20
Q4 57.4
Q3 36.3
Q1 0.20
Q2 4.19
Q4 71.6
Q3 24.0
Q1 0.040
Q2 0.99
Q4 96.7
Q3 2.30
Q1 0.020
Q2 0.89
Q4 96.8
Q3 2.32
Q1 0.051
Q2 1.61
Q4 94.2
Q3 4.10
Q1 0.062
Q2 2.93
Q4 90.7
Q3 6.27
Q1 0.052
Q2 2.32
Q4 92.4
Q3 5.24
Q1 0.070
Q2 1.15
Q4 95.6
Q3 3.14
Q1 0.020
Q2 1.38
Q4 95.2
Q3 3.36
Q1 0.073
Q2 2.35
Q4 82.9
Q3 14.7
Q1 0.099
Q2 3.67
Q4 60.6
Q3 35.7
Q1 0.064
Q2 2.31
Q4 84.2
Q3 13.4

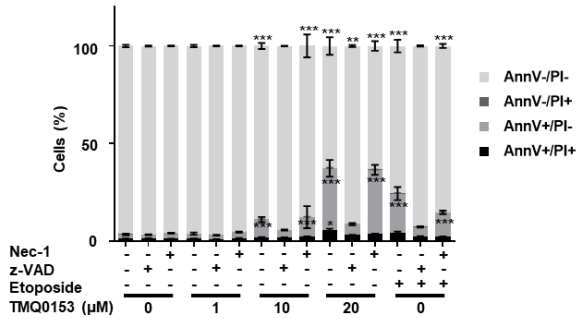
Cells (%)
100
50
0
AnnV-/PI-
AnnV-/PI+
AnnV+/PI-
AnnV+/PI+
Nec-1
z-VAD
Etoposide
TMQ0153 (μM)
0
1
10
20
0

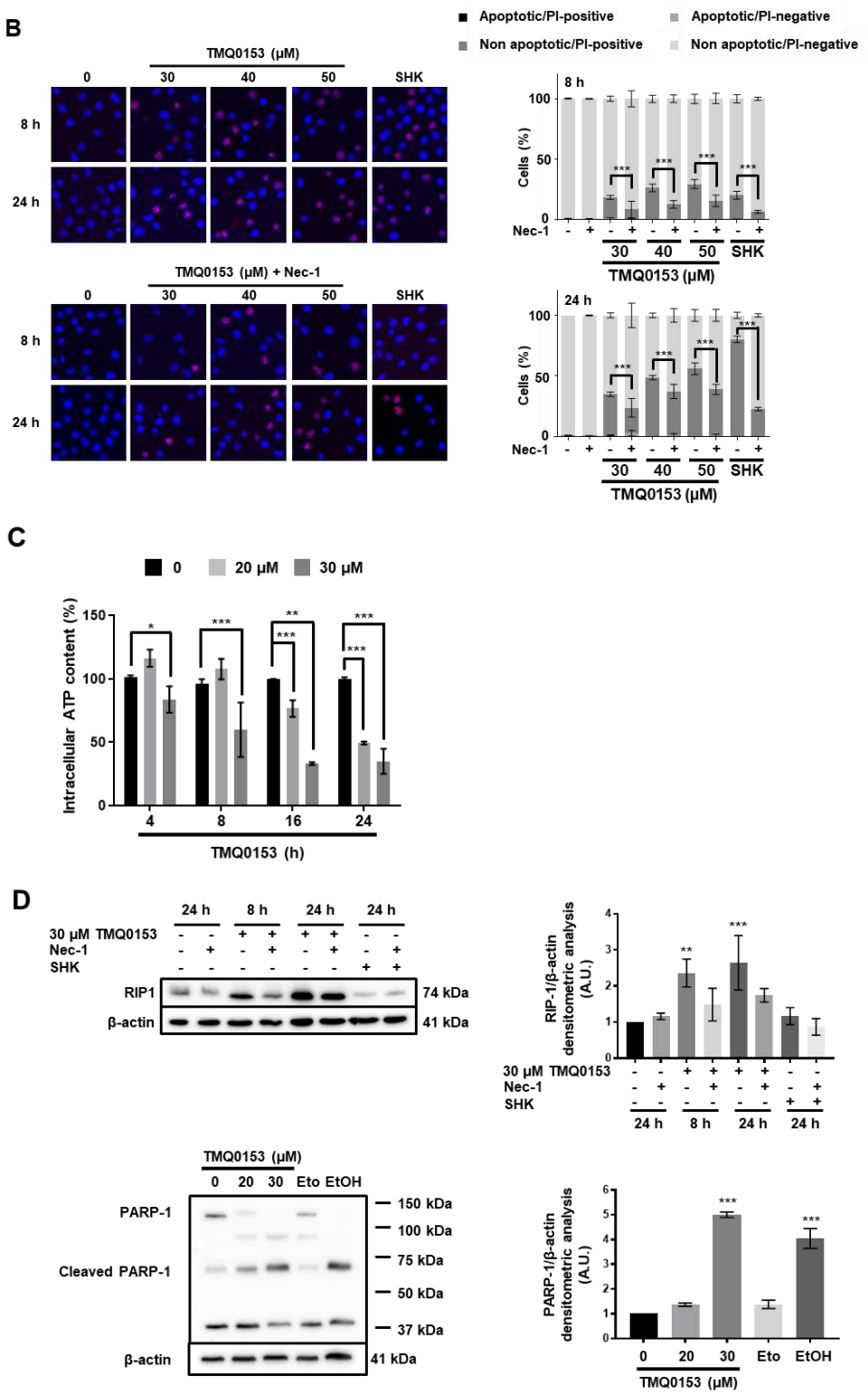
B
Apoptotic/PI-positive
Apoptotic/PI-negative
Non apoptotic/PI-positive
Non apoptotic/PI-negative
TMQ0153 (μM)
0
30
40
50
SHK
8 h
24 h
TMQ0153 (μM) + Nec-1
Cells (%)
Nec-1
TMQ0153 (μM)
C
0
20 μM
30 μM
Intracellular ATP content (%)
TMQ0153 (h)
D
24 h
8 h
30 μM TMQ0153
Nec-1
SHK
RIP1
β-actin
74 kDa
41 kDa
RIP-1/β-actin densitometric analysis (A.U.)
Eto
EtOH
PARP-1
Cleaved PARP-1
150 kDa
100 kDa
75 kDa
50 kDa
37 kDa
PARP-1/β-actin densitometric analysis (A.U.)

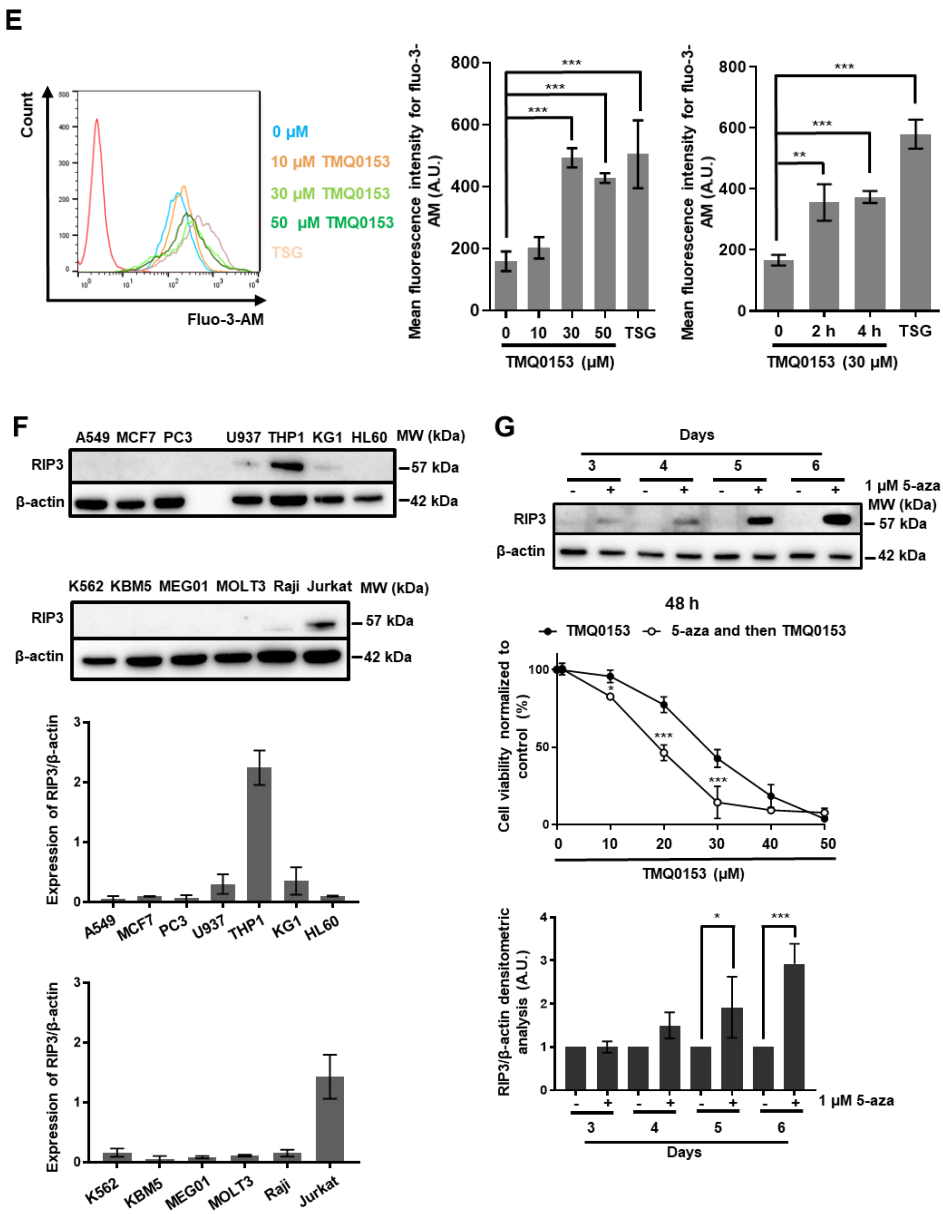

Figure 2.4 TMQ0153 induced a necrostatin-1-sensitive type of cell death in K562 cells (A) K562 cells were incubated in presence or absence of 60 μM necrostatin (Nec)-1 for 1 h and 50 μM z-VAD for 1 h before a treatment with the indicated concentrations of TMQ0153, respectively. Etoposide (Eto; 100 μM) was used as a positive control for apoptosis induction. After 24 h of treatment, the type of cell death triggered by TMQ0153 was characterized by flow cytometry (FACS) after Annexin V APC/propidium iodide (PI) staining. Pictures representative of three independent experiments (top panel) and the corresponding quantifications

(lower panel) are shown. (**B**) K562 cells were incubated in presence or absence of 60 µM necrostatin (Nec)-1 for 1 h before a treatment with the indicated concentrations of TMQ0153. Shikonin (SHK; 5 µM) was used as a positive control for necrosis induction. Nuclear morphology analyses by fluorescence microscopy following Hoechst/ propidium iodide (PI) staining after 8 and 24 h of treatment. Pictures representative of three independent experiments (left panels) and the corresponding quantification (right panels). (**C**) Measurement of intracellular ATP levels at the indicated concentrations and time points. (**D**) Receptor-interacting protein kinase (RIP)1 protein levels and PARP-1 cleavage were determined by western blotting using C2-10 antibody. Shikonin (SHK; 5 µM, 24 h) and necrostatin (Nec)-1 (60 µM, 1 h) were used as a positive control and inhibitor for RIP1. Etoposide (Eto; 100 µM, 24 h) and ethanol (EtOH; 10 %, 2 h) were used as positive controls for apoptotic and necrotic PARP-1 cleavage, respectively. (**E**) Cytosolic Ca^{2+} levels were measured using Fluo-3-AM. Thapsigargin (TSG; 300 nM, 24 h) was used as a positive control for intracellular Ca^{2+} accumulation. (**F**) Western blot analysis of lysates from multiple cancer cells lines showing basal RIP3 expression levels. Cancer cells were used for comparative studies (β–actin ratios). Quantification of the signals (lower panel). (**G**) K562 cells were pre-treated with 1 µM 5-azacytidine (5-aza) for 3 days and then treated with TMQ0153 for 48 h and cell viability was assessed by trypan blue assay. RIP3 protein levels were detected by western blot (upper panel) and the corresponding densitometric analysis is shown (lower panel). β–actin was used as loading control. All pictures are representative of three independent experiments and all graphs represent the mean (± S.D.) of three independent experiments. Statistical significance was assessed as *P<0.05, **P<0.01, ***P<0.001 for the indicated comparisons. Two-way ANOVA (FACS, microscopy analysis, cell viability); post hoc: Sidak's test. Two-way ANOVA (cell titer glo assay, western blot quantification); post hoc; Tukey's test. One-way ANOVA (intracellular Ca^{2+} assay); post hoc; Dunnett's test.

2.4.5. TMQ0153 induces an early onset of autophagy in K562 cells followed by controlled necrosis

As we observed extensive vacuole formation **(Figure 2.5A)** in

treated K562 cells prior to cell death induction, we hypothesized that TMQ0153 was triggering an initial intracellular stress reaction, potentially *via* autophagy. TMQ0153 dose-dependently and progressively induced the conversion of LC3-I to LC3-II between 10 to 50 µM after 2 h by western blot analysis. Results showed that TMQ0153 significantly increased LC3-II levels at 10 µM **(Figure 2.5B)**. In addition, there is a significant increase of LC3 conversion between 10 and 30 µM potentially reflecting the differential ATP levels in the treated cells. Based on these results, an initial morphological analysis of TMQ0153-treated K562 cells by confocal microscopy and Diff-Quik staining allowed quantifying early vesicle formation (**Figure 2.5C**). Treatment of K562 cells with TMQ0153 at necroptosis-inducing concentrations (30 µM) for 2, 4, 6 and 8 h showed the onset of vesicle formation by confocal microscopy after CYTO-ID staining further ascertaining autophagic activity **(Figure 2.5D)**. Western blot analysis demonstrated that TMQ0153 time-dependently induced the conversion of LC3-I to LC3-II at 30 µM after 2, 4, 6 and 8 h, prior to necroptosis induction. In agreement with these results, sequestosome-1 (SQST)M1/p62 **(Figure 2.5E)** was degraded. Moreover, in the presence of the lysosome inhibitor baf-A1, we observed an enhanced accumulation of LC3-II and p62 levels in TMQ0153-treated cells after 2 and 4 h confirming an active autophagic flux (**Figure 2.5F**). Results were confirmed by transmission electron microscopy (TEM) confirming extensive vacuolization **(Figure 2.5G)**.

To investigate the effect of TMQ0153 on cellular metabolism, we used a Seahorse XF Analyzer. Our results showed a significant decrease of the oxygen consumption rate (OCR) upon 4 h of treatment with 30 µM TMQ0153 (**Figure 2.5H)**, which precedes necroptosis induction. As these results indicated that TMQ0153 disrupted mitochondrial bioenergetics, we further detected mitochondria with damaged morphologies by TEM (4h, 30 µM) in line with the observed metabolic alterations.

We then investigated the effect of autophagy induction on caspase-8 expression levels. Our results showed a progressive reduction of pro-caspase-8 levels during autophagy induction between 2 and 8 h with 30 µM TMQ0153 **(Figure 2.5I)**. Despite the progressive degradation of pro-caspase-8 after treatment, **Figure 2.5J** shows that chemical inhibition of autophagy at 8 h by Baf-A1, 3-MA and CQ does not allow to significantly rescue pro-caspase-8 levels. Noteworthy, under the same conditions, caspase 3/7 and -9 activities significantly decreased **(Figure 2.5K).**

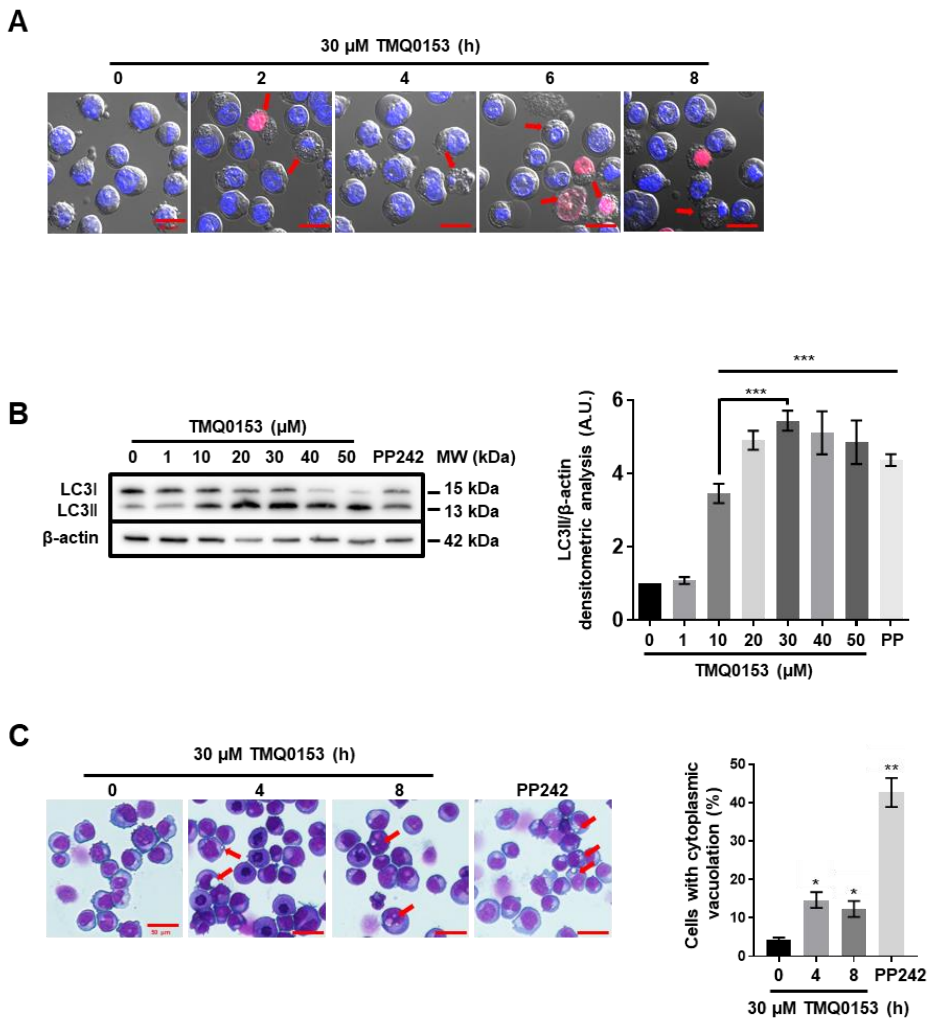

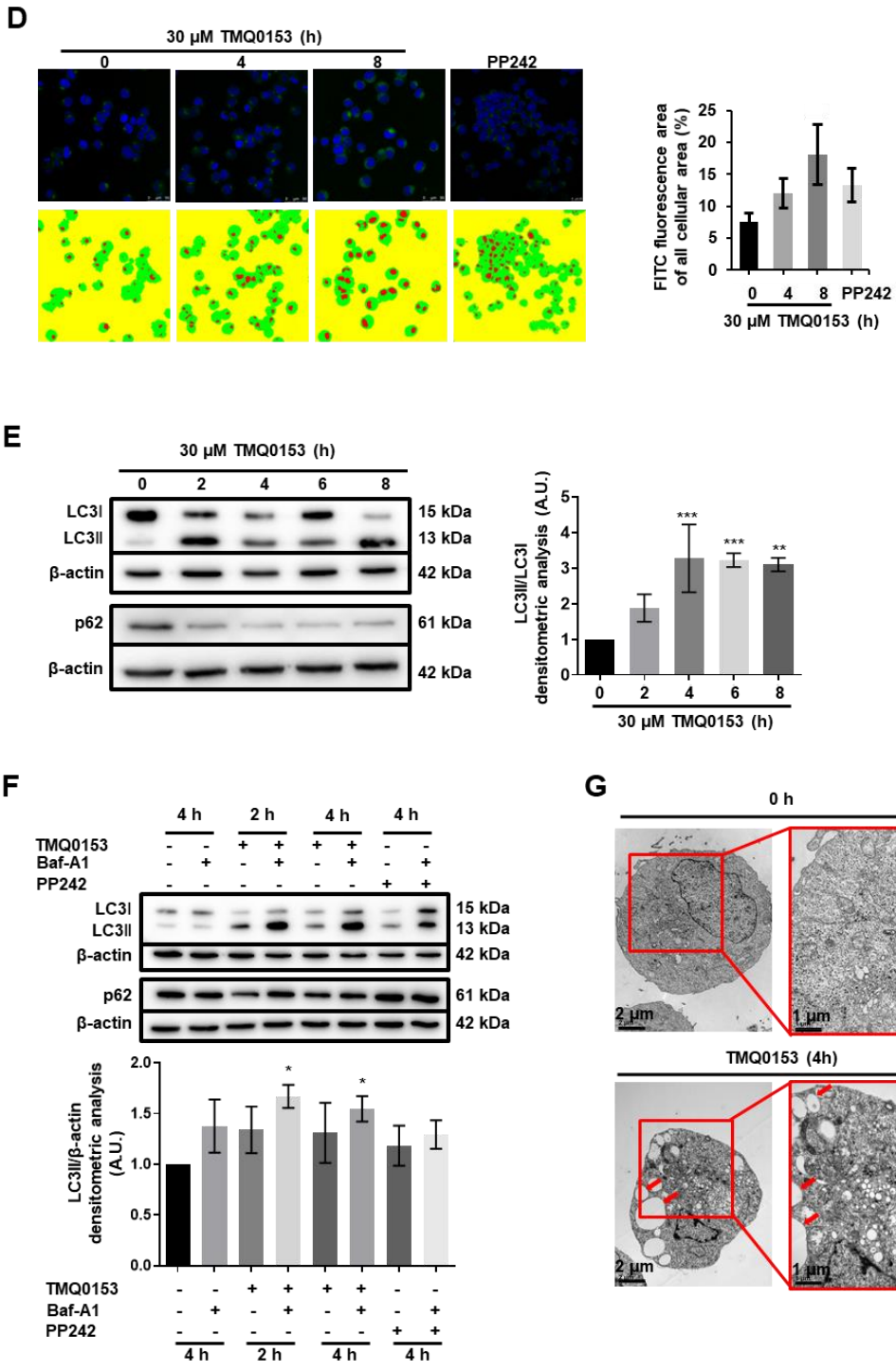
D
30 μM TMQ0153 (h)
0
4
8
PP242
FITC fluorescence area of all cellular area (%)
25
20
15
10
5
0
0 4 8 PP242
30 μM TMQ0153 (h)
E
30 μM TMQ0153 (h)
0 2 4 6 8
LC3I
LC3II
β-actin
15 kDa
13 kDa
42 kDa
p62
β-actin
61 kDa
42 kDa
LC3II/LC3I densitometric analysis (A.U.)
5
4
3
2
1
0
***
***
**
0 2 4 6 8
30 μM TMQ0153 (h)
F
4 h
2 h
4 h
4 h
TMQ0153
Baf-A1
PP242
LC3I
LC3II
β-actin
15 kDa
13 kDa
42 kDa
p62
β-actin
61 kDa
42 kDa
LC3II/β-actin densitometric analysis (A.U.)
2.0
1.5
1.0
0.5
0.0
*
*
TMQ0153
Baf-A1
PP242
4 h
2 h
4 h
4 h
G
0 h
2 μm
1 μm
TMQ0153 (4h)
2 μm
1 μm

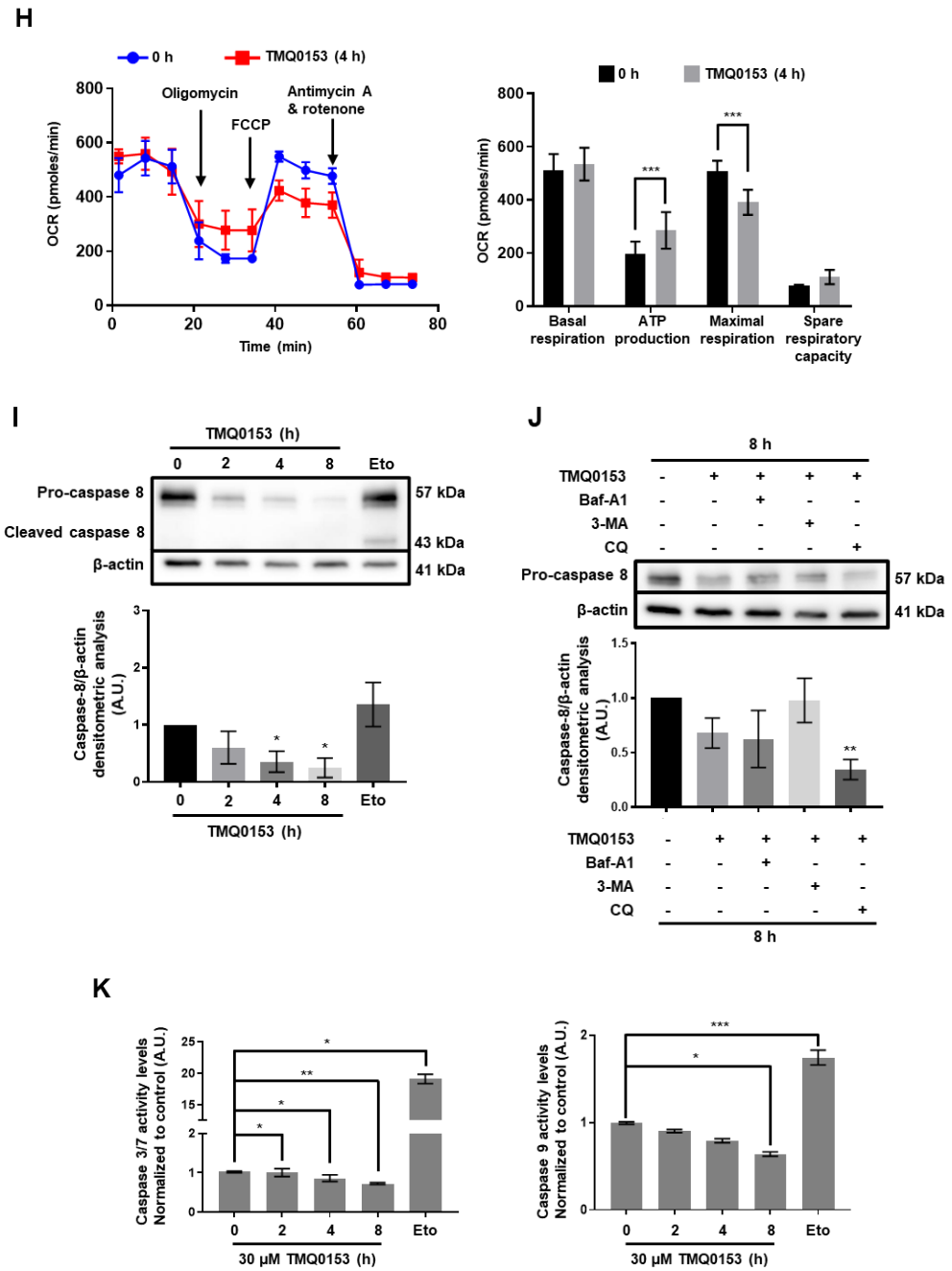

Figure 2.5 TMQ0153 stimulated autophagy prior to necroptosis K562 cells were treated with 30 μM TMQ0153 for the indicated time points (**A**) Confocal microscopy observations after Hoechst/propidium iodide staining. Arrowhead: intracellular vacuole formation. **(B)** Western blot detection of LC3 protein levels (left panel) and the corresponding densitometric analysis (right panel). 10 μM PP242 for 4 h was used as a positive control for autophagy induction. (**C)** Pictures

acquired under light microscopy after Diff-Quik staining (left panel) and the corresponding quantification of the percentage of vacuole-containing cells (right panel). (**D)** Confocal UV microscopy analysis after staining with Cyto-ID (left panel). Representative images of FITC stained images in the 4 groups accompanied by the corresponding pseudocolor masks (red: FITC signal, green: cell area) used for calculation and the corresponding quantification of fluorescence intensity (right panel). Statistical results were compared by Kruskal-Wallis test followed by Conover post-test further adjusted by the Benjamini-Hochberg FDR method. 0 h vs. 4 h and vs 8 h ($p < 0.0004$ and $p < 0.00006$, respectively), 4 h vs.8 h ($p < 0.002$). (**E**) Western blot detection of LC3 and p62 protein levels (left panel) and the corresponding densitometric analysis (right panel) (**F**) Similar analysis in cells pretreated with 40 nM bafilomycin A1 (baf-A1) for 1 h (upper panel) and the corresponding densitometric analysis (lower panel). 10 µM PP242 for 4 h was used as a positive control for autophagy induction. (**G**) Transmission electron microscopy at 12.000x and 25.000x magnification. (**H**) Oxygen consumption rate (OCR) was measured by Seahorse XFp analyzer. (**I**) Caspase 8 analysis by western blot. Etoposide (Eto; 100 µM, 24 h) was used as a positive control for apoptotic caspase cleavage. **(J)** Caspase 8 analysis by western blot in the presence or absence of autophagy inhibitors: 40 nM baf-A1, 10 mM, 3-methyladenine (3-MA) and 75 µM chloroquine (CQ). In western blot analyses, β-actin was used as a loading control. **(K)** Quantification of caspases-3/7 (left graph) and -9 activity (right graph) levels at 30 µM of TMQ0153 treatment. Etoposide (Eto; 100 *µM*, 24 h) was used as a positive control for apoptosis induction. All pictures are representative of three independent experiments and data represent mean (± S.D.) of three independent experiments. Statistical significance was assessed as $*p < 0.05$, $**p < 0.01$, $***p < 0.001$ compared to untreated cells unless otherwise specified. One-way ANOVA (diff-quick); post hoc; Dunnett's test. One-way ANOVA (western blot quantification); post hoc; Tukey's test. Two-way ANOVA (mito stress test); post hoc; Sidak's test.

2.4.6. Autophagic inhibitors augment necroptosis induced by TMQ0153 in K562 cells

To investigate the relationship between TMQ0153 induced

autophagy and necroptosis, K562 cells were treated with TMQ0153 in the presence of autophagic inhibitors. Nuclear morphology analyses showed that the inhibition of TMQ0153-induced autophagy by baf-A1 significantly enhanced necroptosis in K562 cells compared to cells treated with TMQ0153 alone **(Figure 2.6A)**. In addition, baf-A1-, 3-MA- and CQ-mediated inhibition of autophagy led to necroptotic cell death in line with a switch from apoptotic to necrotic cell demise and concomitant with the reduction of procaspase-8 levels **(Figure 2.5I)**.

To avoid non-specific effects of chemical inhibitors, we then also investigated the effect of TMQ0153-induced autophagy in beclin 1 siRNA-transfected cells. Silencing beclin 1 enhanced necroptosis **(Figure 2.6B)** and decreased autophagy **(Figure 2.6C)**. Moreover, enhanced levels of necrotic PARP-1 cleavage products (50-75 kDa) were detected when using the C2-10 anti-PARP antibody **(Figure 2.6D&E)**. Altogether, whereas inhibition of autophagy did not allow a significant switch towards apoptosis, it caused increased levels of necrosis, most likely due to induction of energetic catastrophe.

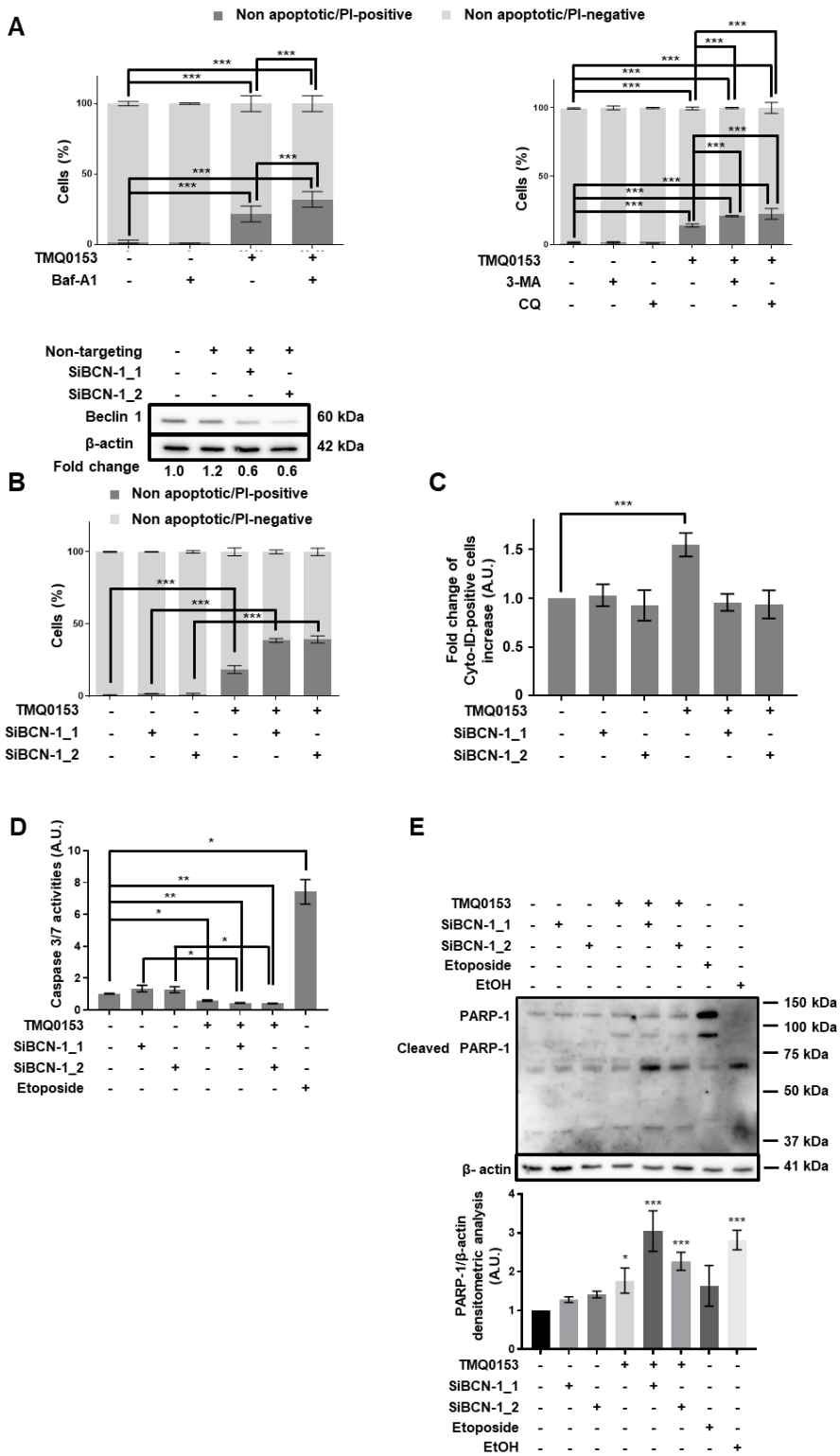

Figure 2.6 Inhibition of autophagy increases TMQ0153-induced necroptosis

(**A**) Effect of autophagy inhibitors [40 nM baf-A1, 10 mM, 3-methyladenine (3-

MA) and 75 µM chloroquine (CQ)] on 30 µM TMQ0153-induced K562 cell death assessed by nuclear morphology analysis after 8 h of treatment. (**B-E**) K562 cells were transfected with specific small interferin (si)RNAs against beclin 1 [(SiBCN-1), 5 nM SiBCN-1_1 and 10 nM SiBCN-1_2] for 24 h. (**B**) Upper panel: effect of siRNA on beclin 1 protein expression level. Lower panel: transfected cells were treated with 30 µM of TMQ0153 and a nuclear morphology analysis was carried out after 8 h of treatment. (**C-E**) Effect of siRNA on TMQ0153-induced autophagy quantified by flow cytometry after Cyto-ID staining (**C**); on caspase-3/7 activity (**D**), and PARP-1 cleavage using C2-10 antibody (**E**). Etoposide (Eto; 100 µM, 24 h) and EtOH (10 %, 2 h) were used as positive controls for apoptotic and necrotic PARP-1 cleavage, respectively. In western blot analyses, β-actin was used as a loading control. All pictures are representative of three independent experiments and data represent mean (±S.D.) of three independent experiments Statistical significance was assessed as *P<0.05, **P<0.01, ***P<0.001, ****P<0.0001 for the indicated comparisons. Two-way ANOVA (nuclear morphology analysis); post hoc; Sidak's test. One-way ANOVA (Cyto-ID asaay); post hoc; Dunnett's test. One-way ANOVA (caspase 3/7 assay); post hoc; Tukey's test.

2.4.7. CML patient cells are characterized by increased expression levels of genes involved in oxidative stress

We wanted to further document the status of activated redox metabolism by using patient data. Further exacerbation of this status should facilitate cell death induction in agreement with the concept of pro-oxidant CML therapy. Indeed. CML patient cells are characterized by increased expression levels of genes involved in oxidative stress. We used a patient cohort regrouping 74 healthy donors and leukemia patients including 76 patients that were diagnosed with CML [168, 169] to assess the gene expression level of oxidative stress-related genes. In particular, in assessing the gene expression level of the NADPH oxidases (NOX) family constituted of 7 members (NOX1-NOX5, DUOX1, DUOX2), as they are largely responsible for the production of ROS [176]. Our results show that the expression level of NOX

regulator cytochrome b-245 heavy chain (CYBB) was more elevated in CML patients compared to healthy donors (**Figure 2.7A**) leading to an increased NOX activity and thus an increase in ROS production [177]. Based on these observations, we hypothesized that the resulting increased ROS levels in CML patient cells could be therapeutically targeted by exacerbation of intracellular ROS levels by TMQ0153 leading to a pro-oxidant treatment approach. Indeed, from a chemical point of view, TMQ0153 can be redox active similar to quinones and afford radical anions leading to the formation of reactive superoxide.

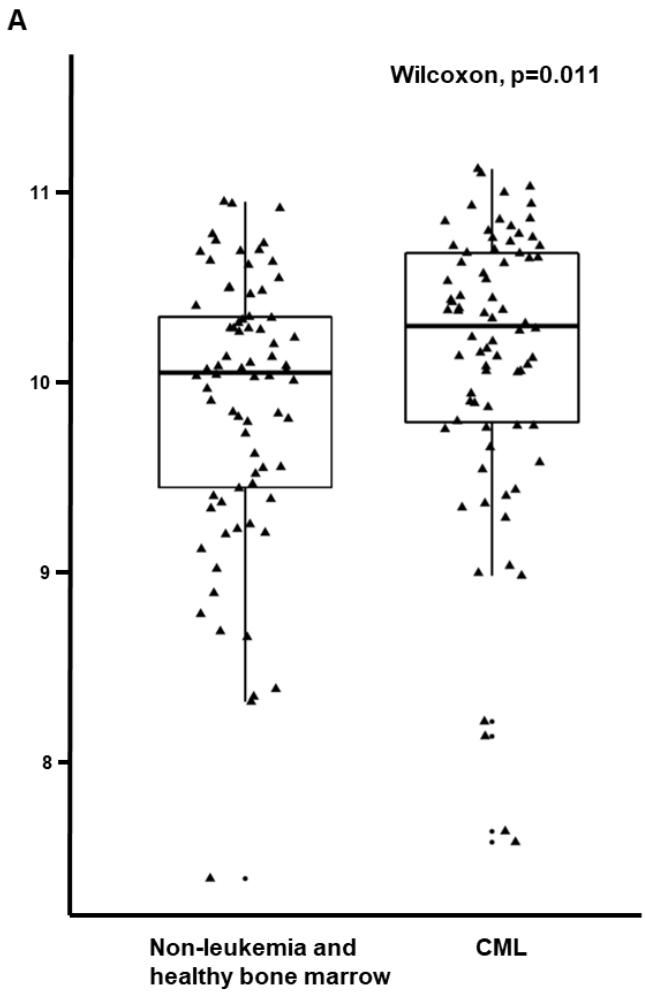

Figure 2.7 CYBB expression in healthy donors and CML patients from the MILE study (A) Outliers are represented as dots while healthy donors and CML patients are represented as triangles. Wilcoxon test was used to assess significance.

2.4.8. TMQ0153 depolarizes mitochondrial membrane potential and triggers necroptotic cell death through ROS formation

Accumulation of intracellular ROS is known to depolarize the mitochondrial membrane potential (MMP). First, we performed a morphological analysis of mitochondria by TEM after treatment of K562 with TMQ0153 (30 µM). Our results showed that 30 µM TMQ0153 induced mitochondrial morphological changes such as enlarged and swollen mitochondria compared to control after 8 h **(Figure 2.8A&B).** Next, we measured the MMP in K562 cells after 24h of treatment with TMQ0153. Results demonstrated that TMQ0153 increased the proportion of cells with low MMP in a dose-dependent manner **(Figure 2.8C)** In addition, TMQ0153-mediated reduced cell viability and MMP loss were totally prevented by the ROS scavenger NAC **(Figure 2.8D)** and also prevented by the RIP1 inhibitor Nec-1 **(Figure 2.8E).**.

Next, we investigated the implication of ROS in the generation of necroptotic cell death [178]. To identify the nature and roles of intracellular ROS induced by TMQ0153, K562 cells were pretreated with and without various antioxidants: NAC, Trolox and Tiron. Apoptotic concentrations of TMQ0153 (20 µM) did not induce significant levels of ROS compared to a necrosis-inducing concentration (30 µM) after 4 and 8 h whereas pretreatment with NAC significantly abrogated ROS formation at 30 µM **(Figure 2.8F&G)** in both K562 and K562R cells. Vitamin E derivative Trolox that reduces the levels of lipid peroxidation when the oxidation was initiated inside the plasma membrane [179] or mitochondrially-localized Tiron [180] did not significantly reduce ROS levels **(Figure 2.8H)**.

Since the balance of intracellular reduced and oxidized glutathione (GSH) levels reflects the redox state of the cells, we evaluated total GSH levels and the GSH/GSSG ratio after 4 and 24 h of treatment. Results revealed that both total GSH levels and GSH/GSSG ratio were significantly reduced upon 30 µM TMQ0153 treatment **(Figure 2.8I)**. After GSH

depletion, redox and cellular stress are considered to be potent inducers of mitochondrial dysfunction through ROS accumulation [36]. Therefore, we examined the effect of Nec-1 on intracellular ROS accumulation by TMQ0153 and found that Nec-1 pretreatment decreased cellular ROS levels in TMQ0153-treated K562 cells after 4 and 8 h **(Figure 2.8F)**. This finding could suggest that Nec-1 protects against TMQ0153-induced necroptosis by suppressing the intracellular burden of ROS formation after necroptosis induction. Finally, ROS-induced LMP is increasing in K562 cells after TMQ0153-induced necroptotic cell death in a time-dependent manner at 30 μM as demonstrated by fluorescence microscopy and FACS **(Figure 2.8J)**.

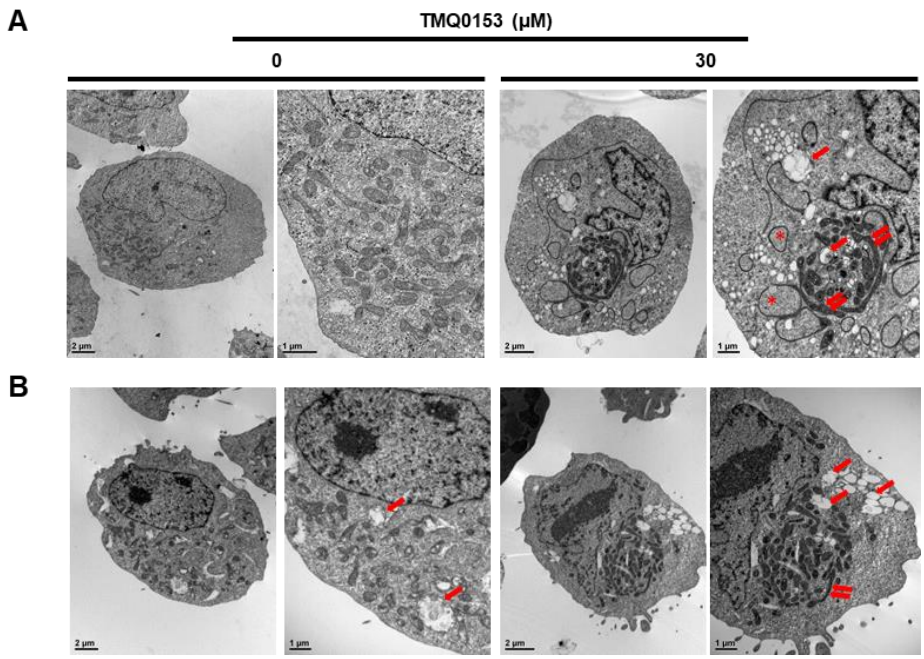

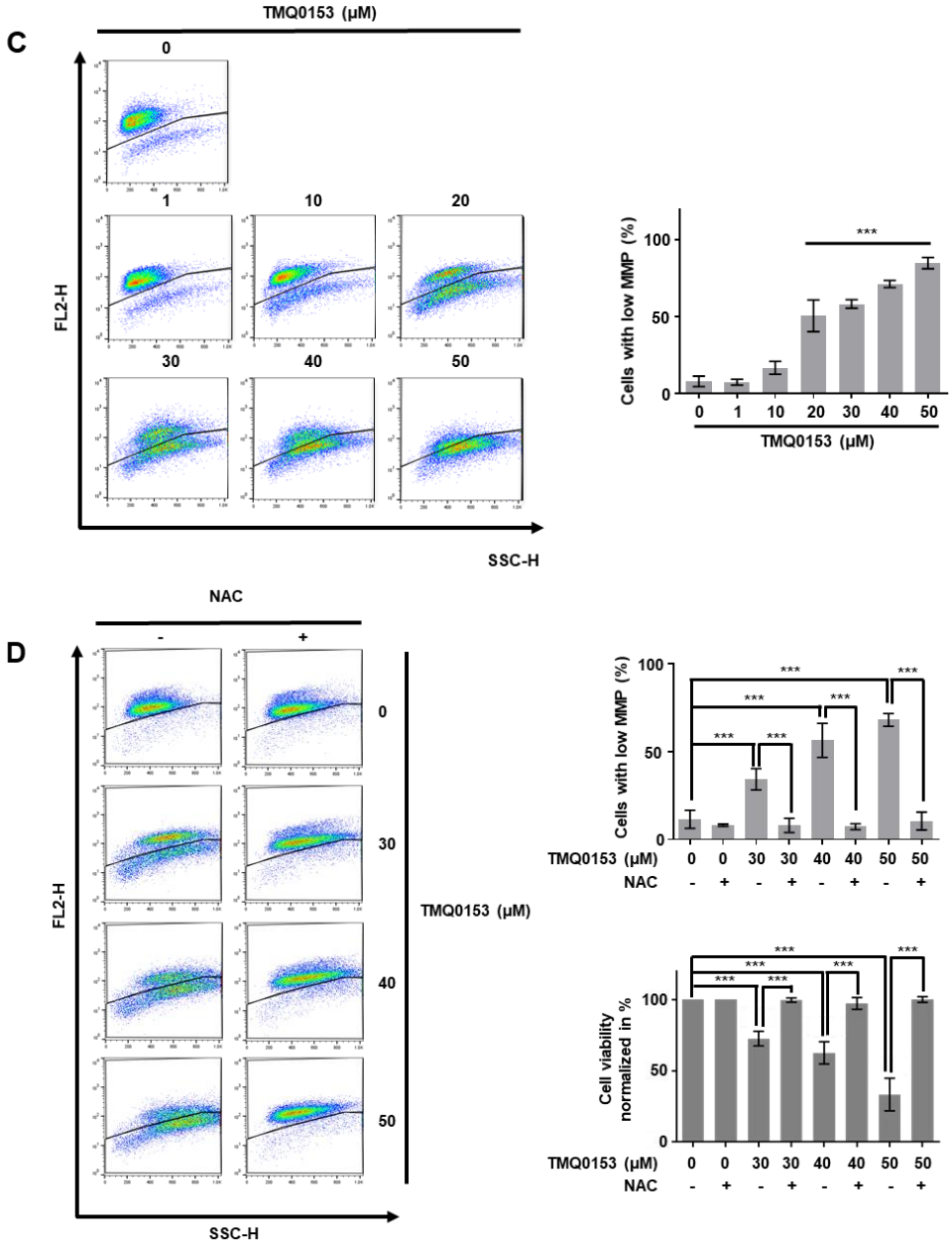
C
TMQ0153 (μM)
0
1
10
20
30
40
50
FL2-H
SSC-H
Cells with low MMP (%)
100
50
0
***
0 1 10 20 30 40 50
TMQ0153 (μM)
D
NAC
-
+
0
30
40
50
TMQ0153 (μM)
FL2-H
SSC-H
Cells with low MMP (%)
***
TMQ0153 (μM) 0 0 30 30 40 40 50 50
NAC - + - + - + - +
Cell viability normalized in %
***
TMQ0153 (μM) 0 0 30 30 40 40 50 50
NAC - + - + - + - +

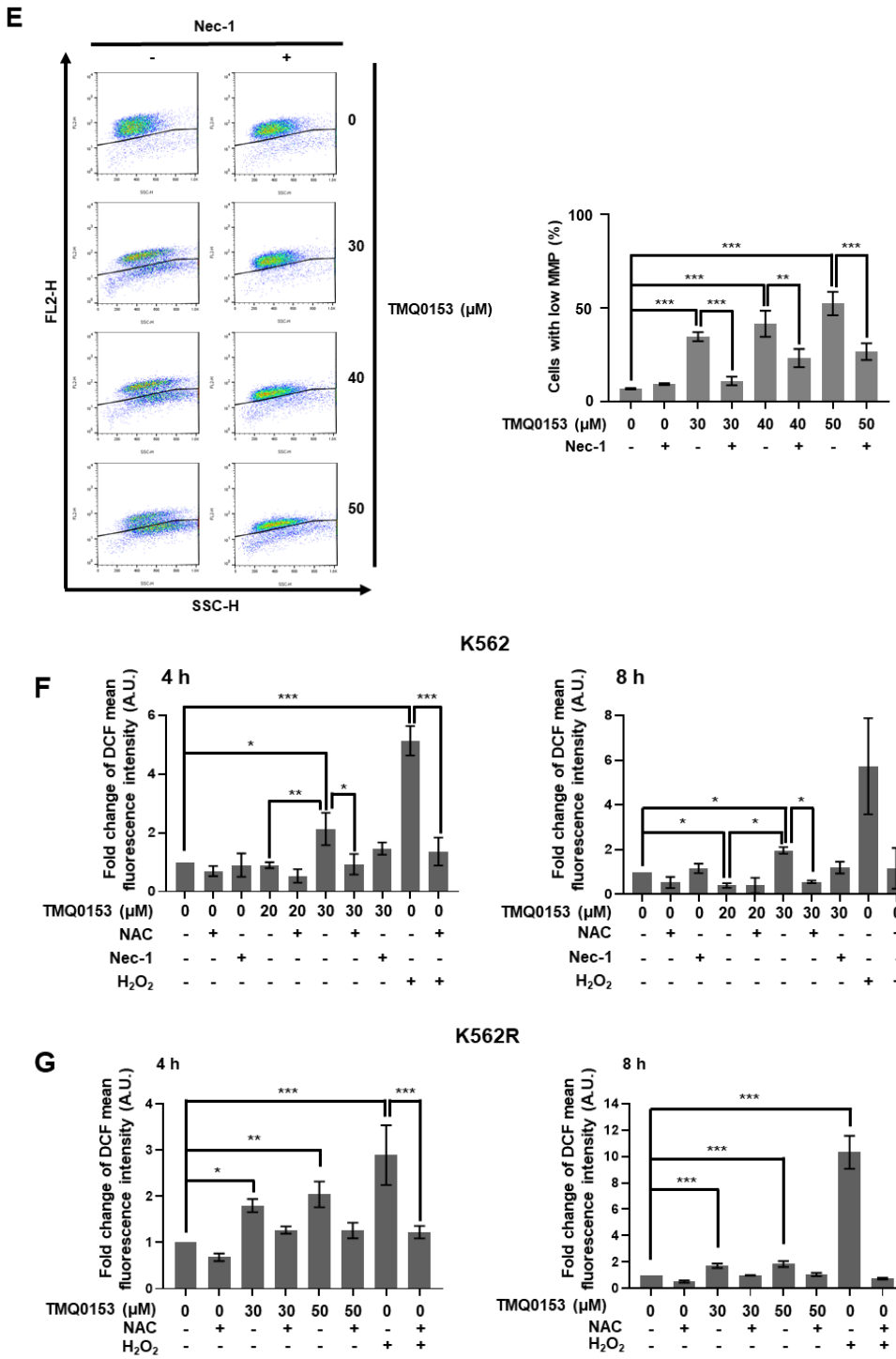
E
Nec-1
-
+
FL2-H
SSC-H
0
30
40
50
TMQ0153 (μM)
Cells with low MMP (%)
100
50
0
TMQ0153 (μM) 0 0 30 30 40 40 50 50
Nec-1 - + - + - + - +
K562
F
4 h
Fold change of DCF mean fluorescence intensity (A.U.)
TMQ0153 (μM) 0 0 0 20 20 30 30 30 0 0
NAC - + - - + - + - - +
Nec-1 - - + - - - - + - -
H2O2 - - - - - - - - + +
8 h
K562R
G
4 h
8 h

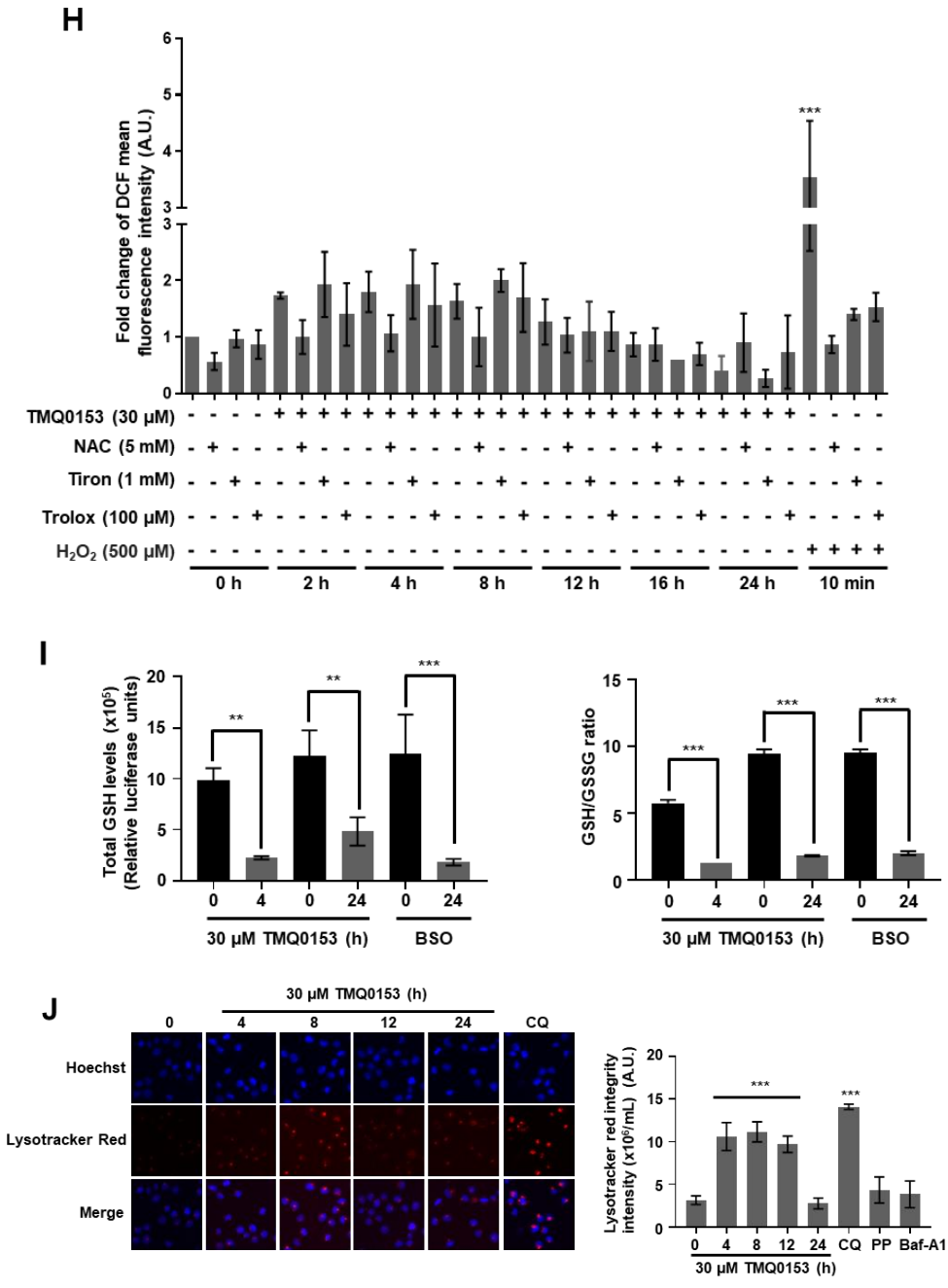
H
Fold change of DCF mean fluorescence intensity (A.U.)
***
TMQ0153 (30 μM)
NAC (5 mM)
Tiron (1 mM)
Trolox (100 μM)
H2O2 (500 μM)
0 h
2 h
4 h
8 h
12 h
16 h
24 h
10 min
I
Total GSH levels (x10^5) (Relative luciferase units)
**
**
***
0
4
0
24
0
24
30 μM TMQ0153 (h)
BSO
GSH/GSSG ratio
***
***
***
0
4
0
24
0
24
30 μM TMQ0153 (h)
BSO
J
30 μM TMQ0153 (h)
0
4
8
12
24
CQ
Hoechst
Lysotracker Red
Merge
Lysotracker red integrity intensity (x10^6/mL) (A.U.)
***
***
0
4
8
12
24
CQ
PP
Baf-A1
30 μM TMQ0153 (h)

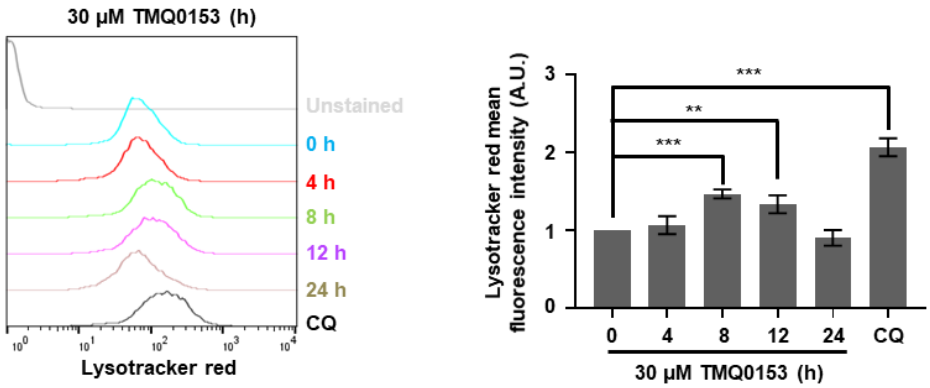

Figure 2.8 TMQ0153 induced mitochondrial dysfunction, decreased GSH levels, involvement of LMP and ROS in K562 cells (**A**) Cells were treated with TMQ0153 for 8 h and mitochondrial morphology was assessed by TEM at 12.000x and 25.000x magnification. (**B**) Cells were treated with TMQ0153 for 4h **(left picture)** and for 8 h **(right picture)** and mitochondrial morphology was assessed by TEM at 12.000x and 25.000x magnification. Single arrows and double arrows indicate respectively dilated and giant mitochondria. **(C)** Mitochondrial membrane potential (MMP) analysis in cells treated with increasing concentrations of TMQ0153 for 24 h. The fraction of low MMP presenting cells is depicted. (**D**) Cells were pre-incubated for 1 h in presence or absence of 50 mM N-acetyl-L-cysteine (NAC) followed by a treatment with the indicated concentrations of TMQ0153. After 24 h of treatment, MMP (upper panel) cell viability (bottom panel) were assessed by trypan blue assay and flow cytometry, respectively. **(E)** Cells were pre-incubated for 1 h in presence or absence of 60 µM necrostatin (Nec)-1 followed by a treatment with the indicated concentrations of TMQ0153. After 24 h of treatment, MMP was assessed by flow cytometry, respectively. (**F**) Cells were pre-incubated for 1 h in presence or absence of 50 mM NAC or 60 µM necrostatin (Nec)-1. After 4 and 8 h of treatment with TMQ0153 at 20 and 30 µM, reactive oxygen species (ROS) levels were measured by flow cytometry following dichlorofluorescein diacetate (H_2DCFDA) staining. H_2O_2 was used as a positive control for ROS induction. **(G)** Reactive oxygen species (ROS) levels were quantified by FACS in K562R cells treated with the indicated concentrations of TMQ0153 and stained with H_2DCFDA. H_2O_2 was used as a positive control for ROS induction. (**H**) Cells were pre-incubated for 1 h in presence or absence of

various antioxidants [N-acetyl-L-cysteine (NAC), tiron and trolox] and then treated or not with TMQ0153. Reactive oxygen species (ROS) were measured at indicated time points using H_2DCFDA. H_2O_2 was used as a positive control for ROS induction **(I)** Quantification of total GSH levels (left panel) and GSH (glutathione)/glutathione disulfide (GSSG) ratio (right panel). 50 μM Buthionine sulfoximine (BSO) was used as a positive control for the inhibition of GSH synthesis **(J)** Cell were stained with Hoechst and Lysotracker Red and analyzed by fluoresence microsopy. Lysotracker Red fluorescence intensity was quantified using Image J 1.8.0 software (upper panel). Lysotracker Red intensity was quantified by FACS (bottom panel). Chloroquine (CQ; 75μM, 4 h), PP242 (PP, 10 μM, 4h) and baf-A1 (40 nM, 4 h) were used as a positive and negative controls for autophagy inhibition and induction, respectively. All pictures are representative of three independent experiments and data represent the mean (±S.D.) of three independent experiments. Statistical significance was assessed as *$p < 0.05$, **$p < 0.01$, ***$p < 0.001$ compared to untreated cells unless otherwise specified. One-way ANOVA (mitochondrial membrane, LMP); post hoc; Dunnett's test. One-way ANOVA (cell viability, ROS, GSH assay); post hoc; Tukey's test.

2.4.9. TMQ0153-treated K562 cells release immunogenic cell death markers

Our results showed a decrease in intracellular ATP levels and increased mitochondrial ROS and cytoplasmic Ca^{2+} levels eventually concomitant with necroptosis induction [83]. Since these changes were described to contribute to the immunogenicity of the dying cells [181], we also assessed the release of HMGB1 and demonstrated that TMQ0153 triggered accumulation HMGB1 in the supernatant in a dose- and time-dependent manner in K562 cells **(Figure 2.9A)**. In addition, 24 h of treatment with TMQ0153 induced extracellular ATP secretion into the supernatant of K562 cells at 30 and 50 μM **(Figure 2.9B)**. Furthermore, the potential immunogenic signal from dying cells also includes proteins that are exposed at the surface of stressed or dying cells. Results showed that TMQ0153-

treated cells increased significantly the ectopic expression of calreticulin (Ecto-CRT) and Ecto-ERp57 **(Figure 2.9C&D)**. These results indicate that TMQ0153-induced necroptosis could further augment immunogenicity of dying K562 cells.

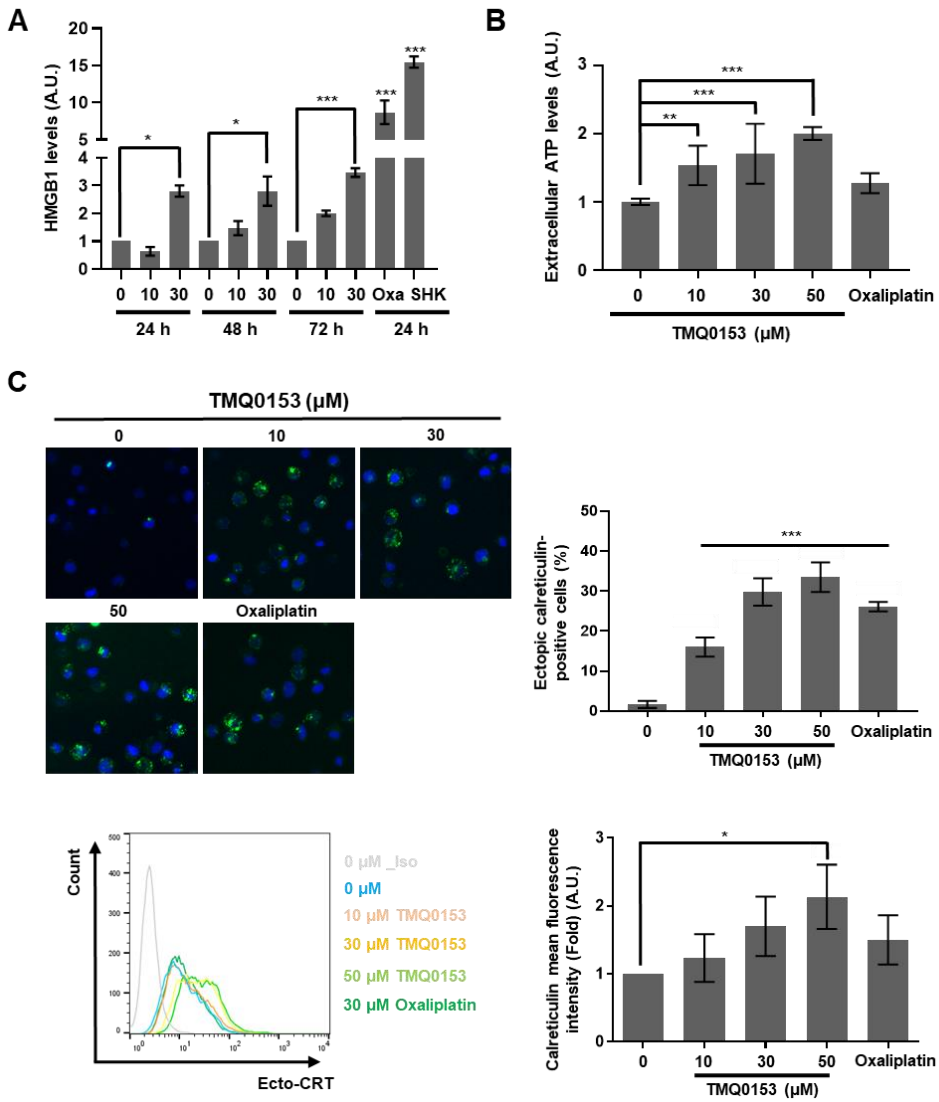

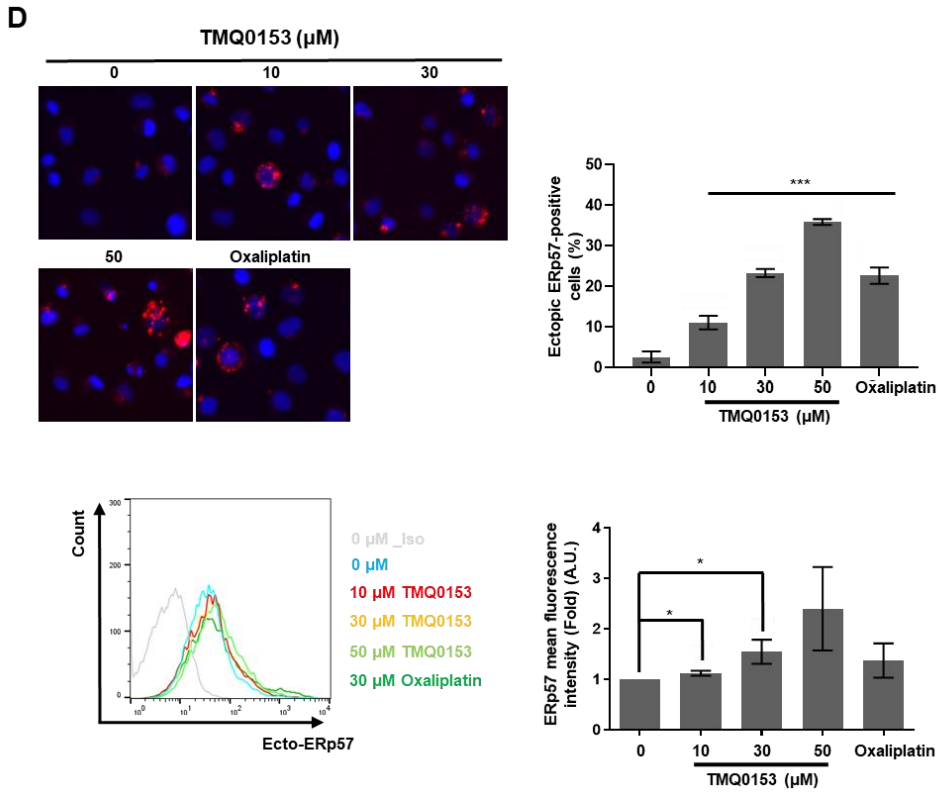

Figure 2.9 TMQ0153 treatments released immunogenic cell death markers from K562 cells (**A**) Supernatants from TMQ0153-treated cells were assessed for high mobility group box (HMGB)1 levels. **(B-D**) Cells were treated for 24 h with the indicated concentrations of TMQ0153, followed by the analysis of (**B**) extracellular ATP release **(C)** calreticulin exposure by fluorescence microscopy after 24 h of TMQ0153 treatment at indicated doses (Upper panel). Quantification of calreticulin-positive cells by FACS (Bottom panel) **(D)** ectopic ERp57 expression by fluorescence microscopy after 24 h of TMQ0153 treatment at indicated doses (Upper panel). Quantification of ERp57-positive cells assessed by FACS (Bottom panel). Oxaliplatin (Oxa, 30 μM, 24 h) and shikonin (SHK; 5 μM, 24 h) were used as positive controls for immunogenic cell death induction. All pictures are representative of three independent experiments and data represent the mean (±S.D.) of three independent experiments. Statistical significance was assessed as *P<0.05, **P<0.01, ***P<0.001 compared to untreated cells. One-wa y ANOVA (HMGB1 assay); post hoc; Tukey's test. One-way ANOVA (extra

cellular ATP assay, calreticulin expression, ERp57 expression); post hoc; Dun nett's test.

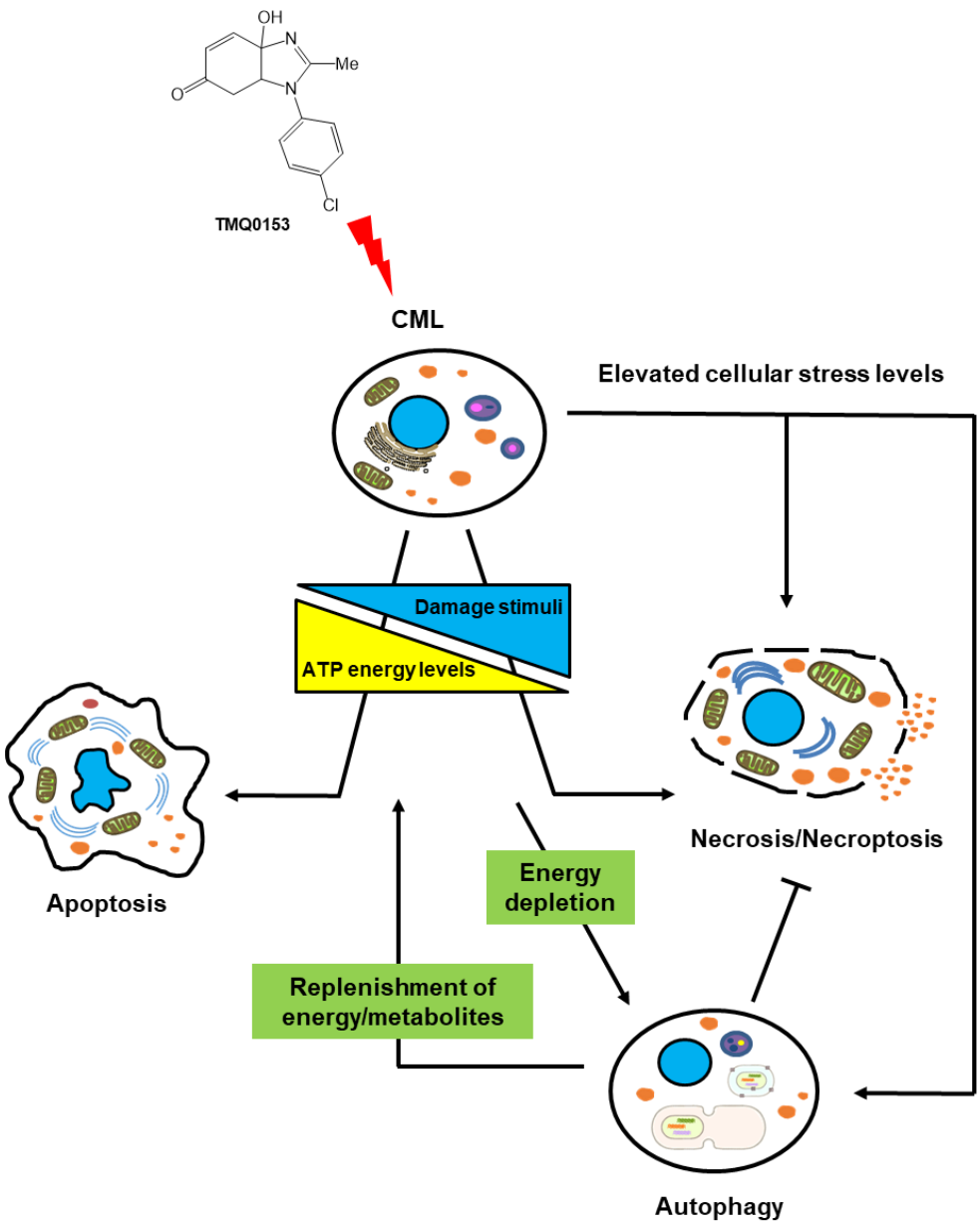

Figure 2.10 Overall mechanism of action of TMQ0153 in CML cells (**A**) TMQ0153 regulates apoptosis, necrosis/necroptosis and autophagy *via* a pro-oxidant cellular stress response in CML. The cell death modalities triggered by TMQ0153 are controlled by various factors including energy/ATP availability, the amplification of damages caused by ROS or cellular stress. Depending on the

severity of damage and amount of stress encountered by the cells, low doses of TMQ0153 triggered apoptosis, whereas higher concentrations induced necroptosis. TMQ0153-induced autophagy contributes to apoptosis inhibition in favor of a RIP1-dependent necroptotic cell death.

2.5. Discussion

CML still has high morbidity and mortality among the leukemia patients [182]. Even though the development of TKIs is an effective treatment against CML, severe side effects and mutations of BCR-ABL are considered as one of main reasons for drug resistance [183]. For this reason, novel therapies that target the molecular or metabolic characteristics of CML are highly required.

In the present study, we attempted to address the interplay between apoptosis, autophagy and necroptosis in CML cell models, by using an experimental pro-oxidant therapeutic approach with the cytotoxic synthetic hydroquinone derivative TMQ0153 aiming to disrupt oxidative and metabolic stress homeostasis. As a result, we observed a ROS-and concentration-dependent induction of protective autophagy eventually leading to Nec-1-sensitive necroptosis, whereas low TMQ0153 concentrations do not trigger any significant increase of ROS levels and led to caspase-dependent apoptosis. We also observed different levels of ATP during the induction of apoptosis and necroptosis. Indeed, ATP is required for caspase activation and induction of apoptosis [184]. Therefore, high levels of ROS can lead to necroptotic cell death whereas low levels of ROS induce apoptotic cell death.

Quinone derivatives such as 5-hydroxy-2-methyl-1,4-naphthoquinone (plumbagin) induce apoptosis or necrosis in AML by producing ROS and decreasing Mcl-1 and Bcl-2 anti-apoptotic proteins abundance [185]. However, the effect of quinone-induced ROS on the apoptotic machinery remains largely unknown. In our study, 20 µM TMQ0153 induced apoptosis in K562 cells along with caspase 8, 9 and 3 cleavage, that are both prevented in presence of z-VAD. In addition, we found that apoptosis was associated with an early downregulation of anti-apoptotic protein Mcl-1 and Bcl-xL after TMQ0153 treatment.

We showed that TMQ0153 induces cell death in K562 cells *via* a

RIP1-dependent necroptotic cell death pathway. 2,3,5-tris-hydroquinone was reported to induce ROS production and increase intracellular Ca^{2+} levels that contribute to PARP-1-mediated necrosis in HK-2 cells [186]. β-lapachone is reduced to β-lapachone hydroquinone, which induces programmed necrosis through the ROS production and a RIP-1-dependent cell death pathway in human hepatocellular carcinoma [135]. Here, TMQ0153 is acting as a pro-oxidant and induces necroptosis through downstream mediators including RIP1 leading to mitochondrial dysfunction as a response to energy depletion. Previous research investigated that cells lacking RIP3 expression were resistant to typical programmed necrotic stimuli but became sensitive when RIP3 is re-expressed [175]. Our results supported these results as we observed a sensitization against TMQ0153 by the re-expression of RIP3 after treatment with the DNA demethylating agent 5-azacitidine [175].

Despite the successful use of TKIs in CML therapy, a better understanding of the physiology of CML cells remains important. According to Karvela et al. [187], CML cells show elevated rates of a basal autophagic flux due to upregulation of autophagy genes including ATG7. In addition, higher levels of ROS and autophagy were shown to be implicated in the development of CML and closely involved in drug resistance in leukemia [188, 189]. Our results confirmed the elevated basal levels of autophagosome formation in K562 cells. Autophagy is triggered as a pro-survival strategy in human cancer cells treated with mammalian target of rapamycin (mTOR) inhibitor rapamycin [190], sarco/endoplasmic reticulum (ER) Ca^{2+}-ATPase (SERCA) inhibitor stemphol [165] or the naphtoquinone shikonin [191]. Indeed, the inhibition of shikonin-induced autophagy increased necroptosis as well as PARP-1-mediated cell death in A549 [191]. Our results support the idea that autophagy protects against necroptosis in TMQ0153-treated K562 as we confirmed that autophagy was detected at early time points before the induction of necroptotic cell death with 30 μM TMQ0153 most likely due to

an early cellular stress response in K562 cells.

In cancer cells, metabolic stress may arise from insufficient energy or oxygen supply. Autophagy can be induced as an alternative source of energy and metabolites [192]. Our results showed that K562 cells treated with autophagy inhibitors such as baf-A1 enhanced necroptotic cell death concomitantly with a non-apoptotic degradation of caspase-8, thus preventing canonical apoptosis induction. These results were confirmed by a profile of PARP-1 degradation typical of necrosis/ necroptosis.

In beclin 1-silenced K562 cells, TMQ0153 induced the appearance of necrotic PARP-1 band and enhanced necroptotic cell population suggesting that autophagy serves a protective role. In addition, we observed that TMQ0153 induced autophagic responses in K562 cells as evidenced by LC3-positive autophagy like vacuoles, and the increased conversion of LC3-I to LC3-II. We also found that pretreatment with baf-A1, which blocks autophagosomal degradation, increased the formation of LC3-II in K562 cells after treatment with TMQ0153.

We provided evidence that TMQ0153 induced the dysfunction of mitochondria as shown by TEM and OCR analysis, as well as oxidative stress *via* increasing ROS levels and triggering accumulation of cytoplasmic Ca^{2+} levels. GSH is an important antioxidant in cellular metabolism and the reduction of GSH levels was described to induce autophagy, apoptotic or necrotic/necroptotic cell death [193, 194]. We observed that intracellular GSH levels decreased during the onset of autophagy and necroptosis induced by TMQ0153. TMQ0153, as a pro-oxidant compound, amplifies ROS stress in K562 cells prior to necroptosis induction. Therefore, necroptotic cell death potentially further exacerbates ROS generation. The change of oxidative stress levels by TMQ0153 affects mitochondria homeostasis leading to different forms of cell death. A shift from apoptosis to necroptosis appears to be associated with decreased mitochondrial function and ATP production [195]. Other mechanisms may involve Ca^{2+} accumulation known to trigger

necroptotic cell death [161].

Weak release of lysosomal enzymes leads to apoptosis, whereas a massive release of lysosomal enzymes results in necrosis [196]. In our study, TMQ0153 induced increased ROS and LMP at early time points which are decreased later when necroptosis is induced. Interestingly, increased ROS levels are specifically reduced by the pre-treatment by NAC but not by Trolox and Tiron. These compounds possess different antioxidant capacities. NAC is a precursor of glutathione and can scavenge different types of ROS [197]. Trolox neutralizes lipid-derived radicals [198] whereas Tiron is a metal chelator [199]. Considering our results, ROS induced by TMQ0153 which is preventable by NAC, must be generated in the mitochondria considering the specific antioxidant effects of NAC [200].

Wiedmer et al. showed that autophagy is upregulated for the clearance of damaged lysosomes, leading to cell recovery, thus playing a pro-survival role [201]. Hence, lysosomal instability triggered by TMQ0153 contributes to final steps of necroptosis. Besides LMP, mitochondrial dysfunction is another executioner of necroptosis [178]. Our results showed that TMQ0153 treatment generated mitochondrial alterations and dysfunction associated with a loss of MMP.

Necroptosis triggers cell membrane rupture and the release of cellular cytoplasmic contents into the extracellular spaces such as HMGB1 and ATP [160]. TMQ0153 treatment significantly released HMGB1 and increased extracellular ATP levels. Immunogenic cell death (ICD) is a form of chemotherapy-induced tumor cell death, which is mediated by damage associated molecular patterns (DAMPs) that triggers effective antitumor immune responses [202]. ICD-inducers are able to mediate endoplasmic reticulum (ER) stress resulting in the cell surface presentation of calreticulin and ERp57 [160, 203]. Here, we showed that TMQ0153 treatment led to CRT and ERp57 surface expression. These results provided evidence that TMQ0153 released ICD markers as an essential feature of this

chemotherapeutic compound.

In summary **(Figure 2.10, based on [204] with modifications)**, TMQ0153 possesses a potent pro-oxidant capacity effective against imatinib-sensitive and -resistant CML cells underlining the interest of TMQ0153 as an experimental pre-clinical therapeutic agent accompanied by release of ICD markers.

References

1. Ryter, S.W. *et al.* Mechanisms of cell death in oxidative stress. *Antioxid Redox Signal* **9**, 49-89 (2007).

2. Circu, M.L. & Aw, T.Y. Reactive oxygen species, cellular redox systems, and apoptosis. *Free Radic Biol Med* **48**, 749-762 (2010).

3. Quinlan, C.L., Treberg, J.R., Perevoshchikova, I.V., Orr, A.L. & Brand, M.D. Native rates of superoxide production from multiple sites in isolated mitochondria measured using endogenous reporters. *Free Radic Biol Med* **53**, 1807-1817 (2012).

4. Brandes, R.P., Weissmann, N. & Schroder, K. Nox family NADPH oxidases: Molecular mechanisms of activation. *Free Radic Biol Med* **76**, 208-226 (2014).

5. Nathan, C. & Cunningham-Bussel, A. Beyond oxidative stress: an immunologist's guide to reactive oxygen species. *Nat Rev Immunol* **13**, 349-361 (2013).

6. Redza-Dutordoir, M. & Averill-Bates, D.A. Activation of apoptosis signalling pathways by reactive oxygen species. *Biochim Biophys Acta* **1863**, 2977-2992 (2016).

7. Pashkovskaia, N., Gey, U. & Rodel, G. Mitochondrial ROS direct the differentiation of murine pluripotent P19 cells. *Stem Cell Res* **30**, 180-191 (2018).

8. Reczek, C.R. & Chandel, N.S. ROS-dependent signal transduction. *Curr Opin Cell Biol* **33**, 8-13 (2015).

9. Gorrini, C., Harris, I.S. & Mak, T.W. Modulation of oxidative stress as an anticancer strategy. *Nat Rev Drug Discov* **12**, 931-947 (2013).

10. Thanan, R. *et al.* Development and characterization of a hydrogen peroxide-resistant cholangiocyte cell line: A novel model of oxidative stress-related cholangiocarcinoma genesis. *Biochem Biophys Res Commun* **464**, 182-188 (2015).

11. Tafani, M. *et al.* The Interplay of Reactive Oxygen Species, Hypoxia, Inflammation, and Sirtuins in Cancer Initiation and Progression. *Oxidative medicine and cellular longevity* **2016**, 3907147 (2016).

12. Cao, L. *et al.* Absence of full-length Brca1 sensitizes mice to oxidative stress and carcinogen-induced tumorigenesis in the esophagus and forestomach. *Carcinogenesis* **28**, 1401-1407 (2007).

13. Mori, K. *et al.* A mitochondrial ROS pathway controls matrix metalloproteinase 9 levels and invasive properties in RAS-activated cancer cells. *FEBS J* **286**, 459-478 (2019).

14. Porporato, P.E. *et al.* A mitochondrial switch promotes tumor metastasis. *Cell Rep* **8**, 754-766 (2014).

15. O'Hagan, H.M. *et al.* Oxidative damage targets complexes containing DNA methyltransferases, SIRT1, and polycomb members to promoter CpG Islands. *Cancer cell* **20**, 606-619 (2011).

16. Florean, C., Schnekenburger, M., Grandjenette, C., Dicato, M. & Diederich, M. Epigenomics of leukemia: from mechanisms to therapeutic applications. *Epigenomics* **3**, 581-609 (2011).

17. Schnekenburger, M., Florean, C., Dicato, M. & Diederich, M. Epigenetic alterations as a universal feature of cancer hallmarks and a promising target for personalized treatments. *Current topics in medicinal chemistry* **16**, 745-776 (2016).

18. Karius, T. *et al.* Reversible epigenetic fingerprint-mediated glutathione-S-transferase P1 gene silencing in human leukemia cell lines. *Biochem Pharmacol* **81**, 1329-1342 (2011).

19. Chio, I.I.C. & Tuveson, D.A. ROS in Cancer: The Burning Question. *Trends Mol Med* **23**, 411-429 (2017).

20. DeNicola, G.M. *et al.* Oncogene-induced Nrf2 transcription promotes ROS detoxification and tumorigenesis. *Nature* **475**, 106-109 (2011).

21. Goodman, G.E. *et al.* The Beta-Carotene and Retinol Efficacy Trial: incidence of lung cancer and cardiovascular disease mortality during 6-year follow-up after stopping beta-carotene and retinol supplements. *J Natl Cancer Inst* **96**, 1743-1750 (2004).

22. Cruz-Bermudez, A. *et al.* Cancer-associated fibroblasts modify lung cancer metabolism involving ROS and TGF-beta signaling. *Free Radic Biol Med* **130**, 163-173 (2019).

23. Bossis, G. *et al.* The ROS/SUMO axis contributes to the response of acute myeloid leukemia cells to chemotherapeutic drugs. *Cell Rep* **7**, 1815-1823 (2014).

24. Fandy, T.E. *et al.* Decitabine induces delayed reactive oxygen species (ROS) accumulation in leukemia cells and induces the expression of ROS generating enzymes. *Clin Cancer Res* **20**, 1249-1258 (2014).

25. Klionsky, D.J. *et al.* Guidelines for the use and interpretation of assays for monitoring autophagy (3rd edition). *Autophagy* **12**, 1-222 (2016).

26. Poprac, P. *et al.* Targeting Free Radicals in Oxidative Stress-Related Human Diseases. *Trends Pharmacol Sci* **38**, 592-607 (2017).

27. Galadari, S., Rahman, A., Pallichankandy, S. & Thayyullathil, F. Reactive oxygen species and cancer paradox: To promote or to suppress? *Free Radic Biol Med* **104**, 144-164 (2017).

28. Liu, Y. *et al.* Cancer drug resistance: redox resetting renders a way. *Oncotarget* **7**, 42740-42761 (2016).

29. Cadet, J., Davies, K.J.A., Medeiros, M.H., Di Mascio, P. & Wagner, J.R. Formation and repair of oxidatively generated damage in cellular DNA. *Free Radic Biol Med* **107**, 13-34 (2017).

30. Winterbourn, C.C. The biological chemistry of hydrogen peroxide. *Methods in enzymology* **528**, 3-25 (2013).

31. Lizama-Manibusan, B. & McLaughlin, B. Redox modification of proteins as essential mediators of CNS autophagy and mitophagy. *FEBS letters* **587**, 2291-2298 (2013).

32. AbdulSalam, S.F., Thowfeik, F.S. & Merino, E.J. Excessive Reactive Oxygen Species and Exotic DNA Lesions as an Exploitable Liability. *Biochemistry* **55**, 5341-5352 (2016).

33. Matt, S. & Hofmann, T.G. The DNA damage-induced cell death response: a roadmap to kill cancer cells. *Cellular and molecular life sciences : CMLS* **73**, 2829-2850 (2016).

34. Gaschler, M.M. & Stockwell, B.R. Lipid peroxidation in cell death. *Biochem Biophys Res Commun* **482**, 419-425 (2017).

35. Kalinina, E.V., Chernov, N.N. & Novichkova, M.D. Role of glutathione, glutathione transferase, and glutaredoxin in regulation of redox-dependent processes. *Biochemistry. Biokhimiia* **79**, 1562-1583 (2014).

36. Franco, R. & Cidlowski, J.A. Glutathione efflux and cell death. *Antioxid Redox Signal* **17**, 1694-1713 (2012).

37. Circu, M.L. & Aw, T.Y. Glutathione and apoptosis. *Free radical research* **42**, 689-706 (2008).

38. Brunelle, J.K. & Chandel, N.S. Oxygen deprivation induced cell death: an update. *Apoptosis* **7**, 475-482 (2002).

39. Jacobson, M.D. & Raff, M.C. Programmed cell death and Bcl-2 protection in very low oxygen. *Nature* **374**, 814-816 (1995).

40. Muschel, R.J., Bernhard, E.J., Garza, L., McKenna, W.G. & Koch, C.J. Induction of apoptosis at different oxygen tensions: evidence that oxygen radicals do not mediate apoptotic signaling. *Cancer Res* **55**, 995-998 (1995).

41. Kamata, H. *et al.* Reactive oxygen species promote TNFalpha-induced death and sustained JNK activation by inhibiting MAP kinase phosphatases. *Cell* **120**, 649-661 (2005).

42. Diederich, M. & Cerella, C. Non-canonical programmed cell death mechanisms triggered by natural compounds. *Semin Cancer Biol* **40-41**, 4-34 (2016).

43. Conrad, M., Angeli, J.P., Vandenabeele, P. & Stockwell, B.R. Regulated necrosis: disease relevance and therapeutic opportunities. *Nat Rev Drug Discov* **15**, 348-366 (2016).

44. Aki, T., Funakoshi, T. & Uemura, K. Regulated necrosis and its implications in toxicology. *Toxicology* **333**, 118-126 (2015).

45. Vanden Berghe, T., Linkermann, A., Jouan-Lanhouet, S., Walczak, H. & Vandenabeele, P. Regulated necrosis: the expanding network of non-apoptotic cell death pathways. *Nat Rev Mol Cell Biol* **15**, 135-147 (2014).

46. Grootjans, S., Vanden Berghe, T. & Vandenabeele, P. Initiation and execution mechanisms of necroptosis: an overview. *Cell death and differentiation* **24**, 1184-1195 (2017).

47. Radogna, F., Dicato, M. & Diederich, M. Cancer-type-specific crosstalk between autophagy, necroptosis and apoptosis as a pharmacological target. *Biochem Pharmacol* **94**, 1-11 (2015).

48. Lin, Y. *et al.* Tumor necrosis factor-induced nonapoptotic cell death requires receptor-interacting protein-mediated cellular reactive oxygen species accumulation. *J Biol Chem* **279**, 10822-10828 (2004).

49. Holler, N. *et al.* Fas triggers an alternative, caspase-8-independent cell death pathway using the kinase RIP as effector molecule. *Nat Immunol* **1**, 489-495 (2000).

50. Saveljeva, S., Mc Laughlin, S.L., Vandenabeele, P., Samali, A. &

Bertrand, M.J. Endoplasmic reticulum stress induces ligand-independent TNFR1-mediated necroptosis in L929 cells. *Cell Death Dis* **6**, e1587 (2015).

51. Fan, H. *et al.* Involvement of endoplasmic reticulum stress in the necroptosis of microglia/macrophages after spinal cord injury. *Neuroscience* **311**, 362-373 (2015).

52. Ma, Y.M. *et al.* Novel CHOP activator LGH00168 induces necroptosis in A549 human lung cancer cells via ROS-mediated ER stress and NF-kappaB inhibition. *Acta Pharmacol Sin* **37**, 1381-1390 (2016).

53. Basit, F., Cristofanon, S. & Fulda, S. Obatoclax (GX15-070) triggers necroptosis by promoting the assembly of the necrosome on autophagosomal membranes. *Cell death and differentiation* **20**, 1161-1173 (2013).

54. Wang, X. *et al.* Direct activation of RIP3/MLKL-dependent necrosis by herpes simplex virus 1 (HSV-1) protein ICP6 triggers host antiviral defense. *Proc Natl Acad Sci U S A* **111**, 15438-15443 (2014).

55. Li, Y. *et al.* Type I IFN operates pyroptosis and necroptosis during multidrug-resistant A. baumannii infection. *Cell death and differentiation* (2018).

56. Wang, H. *et al.* Mixed lineage kinase domain-like protein MLKL causes necrotic membrane disruption upon phosphorylation by RIP3. *Mol Cell* **54**, 133-146 (2014).

57. Xia, B. *et al.* MLKL forms cation channels. *Cell Res* **26**, 517-528 (2016).

58. Petrie, E.J. *et al.* Conformational switching of the pseudokinase domain promotes human MLKL tetramerization and cell death by necroptosis. *Nat Commun* **9**, 2422 (2018).

59. Dondelinger, Y. *et al.* MLKL compromises plasma membrane integrity by binding to phosphatidylinositol phosphates. *Cell Rep* **7**, 971-981 (2014).

60. Kaiser, W.J. *et al.* Toll-like receptor 3-mediated necrosis via TRIF, RIP3, and MLKL. *J Biol Chem* **288**, 31268-31279 (2013).

61. Upton, J.W., Kaiser, W.J. & Mocarski, E.S. DAI/ZBP1/DLM-1 complexes with RIP3 to mediate virus-induced programmed necrosis that is targeted by murine cytomegalovirus vIRA. *Cell Host Microbe* **11**, 290-297 (2012).

62. Dillon, C.P. *et al.* RIPK1 blocks early postnatal lethality mediated by caspase-8 and RIPK3. *Cell* **157**, 1189-1202 (2014).

63. Oberst, A. & Green, D.R. It cuts both ways: reconciling the dual roles of caspase 8 in cell death and survival. *Nat Rev Mol Cell Biol* **12**, 757-763 (2011).

64. Marshall, K.D. & Baines, C.P. Necroptosis: is there a role for mitochondria? *Frontiers in physiology* **5**, 323 (2014).

65. Schulze-Osthoff, K. *et al.* Cytotoxic activity of tumor necrosis factor is mediated by early damage of mitochondrial functions. Evidence for the involvement of mitochondrial radical generation. *J Biol Chem* **267**, 5317-5323 (1992).

66. Ye, Y.C. *et al.* RIP1-mediated mitochondrial dysfunction and ROS production contributed to tumor necrosis factor alpha-induced L929 cell necroptosis and autophagy. *Int Immunopharmacol* **14**, 674-682 (2012).

67. Vanlangenakker, N. *et al.* cIAP1 and TAK1 protect cells from TNF-induced necrosis by preventing RIP1/RIP3-dependent reactive oxygen species production. *Cell death and differentiation* **18**, 656-665 (2011).

68. Festjens, N., Vanden Berghe, T. & Vandenabeele, P. Necrosis, a well-orchestrated form of cell demise: signalling cascades, important mediators and concomitant immune response. *Biochim Biophys Acta* **1757**, 1371-1387 (2006).

69. Shindo, R., Kakehashi, H., Okumura, K., Kumagai, Y. & Nakano, H. Critical contribution of oxidative stress to TNFalpha-induced necroptosis downstream of RIPK1 activation. *Biochem Biophys Res Commun* **436**, 212-216 (2013).

70. Degterev, A. *et al.* Chemical inhibitor of nonapoptotic cell death with therapeutic potential for ischemic brain injury. *Nat Chem Biol* **1**, 112-119 (2005).

71. He, S. *et al.* Receptor interacting protein kinase-3 determines cellular necrotic response to TNF-alpha. *Cell* **137**, 1100-1111 (2009).

72. Temkin, V., Huang, Q., Liu, H., Osada, H. & Pope, R.M. Inhibition of ADP/ATP exchange in receptor-interacting protein-mediated necrosis. *Mol Cell Biol* **26**, 2215-2225 (2006).

73. Zhang, D.W. *et al.* RIP3, an energy metabolism regulator that switches TNF-induced cell death from apoptosis to necrosis. *Science* **325**, 332-336 (2009).

74. Roca, F.J. & Ramakrishnan, L. TNF dually mediates resistance and susceptibility to mycobacteria via mitochondrial reactive oxygen species. *Cell* **153**, 521-534 (2013).

75. Tait, S.W. *et al.* Widespread mitochondrial depletion via mitophagy does not compromise necroptosis. *Cell Rep* **5**, 878-885 (2013).

76. Kim, Y.S., Morgan, M.J., Choksi, S. & Liu, Z.G. TNF-induced activation of the Nox1 NADPH oxidase and its role in the induction of necrotic cell death. *Mol Cell* **26**, 675-687 (2007).

77. Festjens, N. *et al.* Butylated hydroxyanisole is more than a reactive oxygen species scavenger. *Cell death and differentiation* **13**, 166-169 (2006).

78. Ardestani, S., Deskins, D.L. & Young, P.P. Membrane TNF-alpha-activated programmed necrosis is mediated by Ceramide-induced reactive oxygen species. *J Mol Signal* **8**, 12 (2013).

79. Yazdanpanah, B. *et al.* Riboflavin kinase couples TNF receptor 1 to NADPH oxidase. *Nature* **460**, 1159-1163 (2009).

80. Meng, X.M. *et al.* NADPH oxidase 4 promotes cisplatin-induced acute kidney injury via ROS-mediated programmed cell death and inflammation. *Lab Invest* **98**, 63-78 (2018).

81. Xie, C. *et al.* Distinct roles of basal steady-state and induced H-ferritin in tumor necrosis factor-induced death in L929 cells. *Mol Cell Biol* **25**, 6673-6681 (2005).

82. Antosiewicz, J., Ziolkowski, W., Kaczor, J.J. & Herman-Antosiewicz, A. Tumor necrosis factor-alpha-induced reactive oxygen species formation is mediated by JNK1-dependent ferritin degradation and elevation of labile iron pool. *Free Radic Biol Med* **43**, 265-270 (2007).

83. Berghe, T.V., Linkermann, A., Jouan-Lanhouet, S., Walczak, H. & Vandenabeele, P. Regulated necrosis: the expanding network of non-apoptotic cell death pathways. *Nature Reviews Molecular Cell Biology* **15**, 135 (2014).

84. Degterev, A. *et al.* Identification of RIP1 kinase as a specific cellular target of necrostatins. *Nat Chem Biol* **4**, 313-321 (2008).

85. McQuade, T., Cho, Y. & Chan, F.K. Positive and negative phosphorylation regulates RIP1- and RIP3-induced programmed necrosis. *Biochem J* **456**, 409-415 (2013).

86. Zhang, Y. *et al.* RIP1 autophosphorylation is promoted by mitochondrial ROS and is essential for RIP3 recruitment into necrosome. *Nature Communications* **8**, 14329 (2017).

87. Schenk, B. & Fulda, S. Reactive oxygen species regulate Smac mimetic/TNFalpha-induced necroptotic signaling and cell death. *Oncogene* **34**, 5796-5806 (2015).

88. Canli, O. *et al.* Glutathione peroxidase 4 prevents necroptosis in mouse erythroid precursors. *Blood* **127**, 139-148 (2016).

89. Chen, J.J., Bertrand, H. & Yu, B.P. Inhibition of adenine nucleotide translocator by lipid peroxidation products. *Free Radic Biol Med* **19**, 583-590 (1995).

90. Esterbauer, H., Schaur, R.J. & Zollner, H. Chemistry and biochemistry of 4-hydroxynonenal, malonaldehyde and related aldehydes. *Free Radic Biol Med* **11**, 81-128 (1991).

91. Orrenius, S., Gogvadze, V. & Zhivotovsky, B. Mitochondrial oxidative stress: implications for cell death. *Annu Rev Pharmacol Toxicol* **47**, 143-183 (2007).

92. Suffys, P. *et al.* Tumour-necrosis-factor-mediated cytotoxicity is correlated with phospholipase-A2 activity, but not with arachidonic acid release per se. *Eur J Biochem* **195**, 465-475 (1991).

93. Vandenabeele, P., Galluzzi, L., Vanden Berghe, T. & Kroemer, G. Molecular mechanisms of necroptosis: an ordered cellular explosion. *Nat Rev Mol Cell Biol* **11**, 700-714 (2010).

94. Vanden Berghe, T. *et al.* Necroptosis, necrosis and secondary necrosis converge on similar cellular disintegration features. *Cell death and differentiation* **17**, 922-930 (2010).

95. Kang, R. *et al.* Lipid Peroxidation Drives Gasdermin D-Mediated Pyroptosis in Lethal Polymicrobial Sepsis. *Cell Host Microbe* **24**, 97-108 e104 (2018).

96. Wang, J. & Yi, J. Cancer cell killing via ROS: to increase or decrease, that is the question. *Cancer biology & therapy* **7**, 1875-1884 (2008).

97. Manda, G. *et al.* The redox biology network in cancer pathophysiology and therapeutics. *Redox Biol* **5**, 347-357 (2015).

98. Guigni, B.A. *et al.* Skeletal muscle atrophy and dysfunction in breast cancer patients: role for chemotherapy-derived oxidant stress. *Am J Physiol Cell Physiol* **315**, C744-C756 (2018).

99. Huang, C.Y. *et al.* Mitochondrial ROS-induced ERK1/2 activation and HSF2-mediated AT1 R upregulation are required for doxorubicin-induced cardiotoxicity. *J Cell Physiol* **233**, 463-475 (2018).

100. Sorensen, J.C. *et al.* BGP-15 Protects against Oxaliplatin-Induced Skeletal Myopathy and Mitochondrial Reactive Oxygen Species Production in Mice. *Frontiers in pharmacology* **8**, 137 (2017).

101. Suzuki, S. *et al.* JNK suppression of chemotherapeutic agents-induced ROS confers chemoresistance on pancreatic cancer stem cells. *Oncotarget* **6**, 458-470 (2015).

102. Han, W., Xie, J., Li, L., Liu, Z. & Hu, X. Necrostatin-1 reverts shikonin-induced necroptosis to apoptosis. *Apoptosis* **14**, 674-686 (2009).

103. Fu, Z. *et al.* The anti-tumor effect of shikonin on osteosarcoma by inducing RIP1 and RIP3 dependent necroptosis. *BMC Cancer* **13**, 580 (2013).

104. Wada, N. *et al.* Shikonin, dually functions as a proteasome inhibitor and a necroptosis inducer in multiple myeloma cells. *Int J Oncol* **46**, 963-972 (2015).

105. Shahsavari, Z., Karami-Tehrani, F., Salami, S. & Ghasemzadeh, M. RIP1K and RIP3K provoked by shikonin induce cell cycle arrest in the triple negative breast cancer cell line, MDA-MB-468: necroptosis as a desperate programmed suicide pathway. *Tumour Biol* **37**, 4479-4491 (2016).

106. Chen, S.Y. *et al.* zVAD-induced autophagic cell death requires c-Src-dependent ERK and JNK activation and reactive oxygen species generation. *Autophagy* **7**, 217-228 (2011).

107. Piao, J.L. *et al.* The molecular mechanisms and gene expression profiling for shikonin-induced apoptotic and necroptotic cell death in U937 cells. *Chem Biol Interact* **205**, 119-127 (2013).

108. Longato, G.B. *et al.* Different cell death responses induced by eupomatenoid-5 in MCF-7 and 786-0 tumor cell lines. *Toxicol In Vitro* **29**, 1026-1033 (2015).

109. Bonapace, L. *et al.* Induction of autophagy-dependent necroptosis is

required for childhood acute lymphoblastic leukemia cells to overcome glucocorticoid resistance. *J Clin Invest* **120**, 1310-1323 (2010).

110. Sulkshane, P. & Teni, T. BH3 mimetic Obatoclax (GX15-070) mediates mitochondrial stress predominantly via MCL-1 inhibition and induces autophagy-dependent necroptosis in human oral cancer cells. *Oncotarget* **8**, 60060-60079 (2017).

111. Simenc, J. & Lipnik-Stangelj, M. Staurosporine induces apoptosis and necroptosis in cultured rat astrocytes. *Drug Chem Toxicol* **35**, 399-405 (2012).

112. Dunai, Z.A. *et al.* Staurosporine induces necroptotic cell death under caspase-compromised conditions in U937 cells. *PLoS One* **7**, e41945 (2012).

113. Lee, P.Y. *et al.* Histone H4 is cleaved by granzyme A during staurosporine-induced cell death in B-lymphoid Raji cells. *BMB Rep* **49**, 560-565 (2016).

114. Xu, Y. *et al.* Cisplatin-induced necroptosis in TNFalpha dependent and independent pathways. *Cell Signal* **31**, 112-123 (2017).

115. McCabe, K.E. *et al.* Triggering necroptosis in cisplatin and IAP antagonist-resistant ovarian carcinoma. *Cell Death Dis* **5**, e1496 (2014).

116. Tristao, V.R. *et al.* Synergistic effect of apoptosis and necroptosis inhibitors in cisplatin-induced nephrotoxicity. *Apoptosis* **21**, 51-59 (2016).

117. Jing, L. *et al.* MLKL-PITPalpha signaling-mediated necroptosis contributes to cisplatin-triggered cell death in lung cancer A549 cells. *Cancer Lett* **414**, 136-146 (2018).

118. Zhang, L., Wang, H., Ding, K. & Xu, J. FTY720 induces autophagy-related apoptosis and necroptosis in human glioblastoma cells. *Toxicol Lett* **236**, 43-59 (2015).

119. Saddoughi, S.A. *et al.* Sphingosine analogue drug FTY720 targets I2PP2A/SET and mediates lung tumour suppression via activation of PP2A-RIPK1-dependent necroptosis. *EMBO Mol Med* **5**, 105-121 (2013).

120. Yu, X. *et al.* Neoalbaconol induces cell death through necroptosis by regulating RIPK-dependent autocrine TNFalpha and ROS production. *Oncotarget* **6**, 1995-2008 (2015).

121. Deng, Q. *et al.* Neoalbaconol induces energy depletion and multiple cell death in cancer cells by targeting PDK1-PI3-K/Akt signaling pathway. *Cell Death Dis* **4**, e804 (2013).

122. Lin, C.Y. *et al.* Simultaneous induction of apoptosis and necroptosis by Tanshinone IIA in human hepatocellular carcinoma HepG2 cells. *Cell Death Discov* **2**, 16065 (2016).

123. Chromik, A.M. *et al.* Comparative analysis of cell death induction by Taurolidine in different malignant human cancer cell lines. *J Exp Clin Cancer Res* **29**, 21 (2010).

124. Mohler, H., Pfirrmann, R.W. & Frei, K. Redox-directed cancer therapeutics: Taurolidine and Piperlongumine as broadly effective antineoplastic agents (review). *Int J Oncol* **45**, 1329-1336 (2014).

125. Stendel, R. *et al.* The antibacterial substance taurolidine exhibits anti-neoplastic action based on a mixed type of programmed cell death. *Autophagy* **5**, 194-210 (2009).

126. Basit, F. *et al.* Mitochondrial complex I inhibition triggers a mitophagy-dependent ROS increase leading to necroptosis and ferroptosis in melanoma cells. *Cell Death Dis* **8**, e2716 (2017).

127. Gong, K. & Li, W. Shikonin, a Chinese plant-derived naphthoquinone, induces apoptosis in hepatocellular carcinoma cells through reactive oxygen species: A potential new treatment for hepatocellular carcinoma. *Free Radic Biol Med* **51**, 2259-2271 (2011).

128. Chen, J. *et al.* Shikonin and its analogs inhibit cancer cell glycolysis by targeting tumor pyruvate kinase-M2. *Oncogene* **30**, 4297-4306 (2011).

129. Shahsavari, Z., Karami-Tehrani, F. & Salami, S. Shikonin Induced Necroptosis via Reactive Oxygen Species in the T-47D Breast Cancer Cell Line. *Asian Pac J Cancer Prev* **16**, 7261-7266 (2015).

130. Xuan, Y. & Hu, X. Naturally-occurring shikonin analogues--a class of necroptotic inducers that circumvent cancer drug resistance. *Cancer Lett* **274**, 233-242 (2009).

131. Bey, E.A. *et al.* An NQO1- and PARP-1-mediated cell death pathway induced in non-small-cell lung cancer cells by beta-lapachone. *Proc Natl Acad Sci U S A* **104**, 11832-11837 (2007).

132. Siegel, D. & Ross, D. Immunodetection of NAD(P)H:quinone oxidoreductase 1 (NQO1) in human tissues. *Free Radic Biol Med* **29**,

246-253 (2000).

133. Strassburg, A., Strassburg, C.P., Manns, M.P. & Tukey, R.H. Differential gene expression of NAD(P)H:quinone oxidoreductase and NRH:quinone oxidoreductase in human hepatocellular and biliary tissue. *Mol Pharmacol* **61**, 320-325 (2002).

134. Siegel, D., Yan, C. & Ross, D. NAD(P)H:quinone oxidoreductase 1 (NQO1) in the sensitivity and resistance to antitumor quinones. *Biochem Pharmacol* **83**, 1033-1040 (2012).

135. Park, E.J. *et al.* beta-Lapachone induces programmed necrosis through the RIP1-PARP-AIF-dependent pathway in human hepatocellular carcinoma SK-Hep1 cells. *Cell Death Dis* **5**, e1230 (2014).

136. Nguyen, M. *et al.* Small molecule obatoclax (GX15-070) antagonizes MCL-1 and overcomes MCL-1-mediated resistance to apoptosis. *Proc Natl Acad Sci U S A* **104**, 19512-19517 (2007).

137. Trudel, S. *et al.* Preclinical studies of the pan-Bcl inhibitor obatoclax (GX015-070) in multiple myeloma. *Blood* **109**, 5430-5438 (2007).

138. Perez-Galan, P., Roue, G., Villamor, N., Campo, E. & Colomer, D. The BH3-mimetic GX15-070 synergizes with bortezomib in mantle cell lymphoma by enhancing Noxa-mediated activation of Bak. *Blood* **109**, 4441-4449 (2007).

139. Bai, L.Y., Chiu, C.F., Chiu, S.J., Chu, P.C. & Weng, J.R. FTY720 Induces Autophagy-Associated Apoptosis in Human Oral Squamous Carcinoma Cells, in Part, through a Reactive Oxygen Species/Mcl-1-Dependent Mechanism. *Sci Rep* **7**, 5600 (2017).

140. Rodak, R. *et al.* Induction of reactive oxygen intermediates-dependent programmed cell death in human malignant ex vivo glioma cells and inhibition of the vascular endothelial growth factor production by taurolidine. *J Neurosurg* **102**, 1055-1068 (2005).

141. Ma, S., Henson, E.S., Chen, Y. & Gibson, S.B. Ferroptosis is induced following siramesine and lapatinib treatment of breast cancer cells. *Cell Death Dis* **7**, e2307 (2016).

142. Rizzi, F. *et al.* Polyphenon E(R), a standardized green tea extract, induces endoplasmic reticulum stress, leading to death of immortalized PNT1a cells by anoikis and tumorigenic PC3 by necroptosis. *Carcinogenesis* **35**, 828-839 (2014).

143. Wallenberg, M. *et al.* Selenium induces a multi-targeted cell death

process in addition to ROS formation. *J Cell Mol Med* **18**, 671-684 (2014).

144. Sonkusre, P. & Cameotra, S.S. Biogenic selenium nanoparticles induce ROS-mediated necroptosis in PC-3 cancer cells through TNF activation. *J Nanobiotechnology* **15**, 43 (2017).

145. Locatelli, S.L. *et al.* BIM upregulation and ROS-dependent necroptosis mediate the antitumor effects of the HDACi Givinostat and Sorafenib in Hodgkin lymphoma cell line xenografts. *Leukemia* **28**, 1861-1871 (2014).

146. Dixon, S.J. *et al.* Pharmacological inhibition of cystine-glutamate exchange induces endoplasmic reticulum stress and ferroptosis. *eLife* **3**, e02523 (2014).

147. Druker, B.J. *et al.* Five-year follow-up of patients receiving imatinib for chronic myeloid leukemia. *N Engl J Med* **355**, 2408-2417 (2006).

148. Kantarjian, H. *et al.* Nilotinib in imatinib-resistant CML and Philadelphia chromosome-positive ALL. *N Engl J Med* **354**, 2542-2551 (2006).

149. Talpaz, M. *et al.* Dasatinib in imatinib-resistant Philadelphia chromosome-positive leukemias. *N Engl J Med* **354**, 2531-2541 (2006).

150. Boulos, N. *et al.* Chemotherapeutic agents circumvent emergence of dasatinib-resistant BCR-ABL kinase mutations in a precise mouse model of Philadelphia chromosome-positive acute lymphoblastic leukemia. *Blood* **117**, 3585-3595 (2011).

151. Blasiak, J., Hoser, G., Bialkowska-Warzecha, J., Pawlowska, E. & Skorski, T. Reactive Oxygen Species and Mitochondrial DNA Damage and Repair in BCR-ABL1 Cells Resistant to Imatinib. *Biores Open Access* **4**, 334-342 (2015).

152. Landry, W.D., Woolley, J.F. & Cotter, T.G. Imatinib and Nilotinib inhibit Bcr-Abl-induced ROS through targeted degradation of the NADPH oxidase subunit p22phox. *Leuk Res* **37**, 183-189 (2013).

153. Heckmann, B.L., Tummers, B. & Green, D.R. Crashing the computer: apoptosis vs. necroptosis in neuroinflammation. *Cell death and differentiation* **26**, 41-52 (2019).

154. Kroemer, G., Galluzzi, L., Kepp, O. & Zitvogel, L. Immunogenic cell death in cancer therapy. *Annu Rev Immunol* **31**, 51-72 (2013).

155. Garg, A.D., Dudek-Peric, A.M., Romano, E. & Agostinis, P. Immunogenic cell death. *Int J Dev Biol* **59**, 131-140 (2015).

156. Radogna, F. & Diederich, M. Stress-induced cellular responses in immunogenic cell death: Implications for cancer immunotherapy. *Biochem Pharmacol* **153**, 12-23 (2018).

157. Pampliega, O. *et al.* Functional interaction between autophagy and ciliogenesis. *Nature* **502**, 194-200 (2013).

158. Shen, H.M. & Codogno, P. Autophagic cell death: Loch Ness monster or endangered species? *Autophagy* **7**, 457-465 (2011).

159. Tran, M.Q. *et al.* Unaromatized Tetrahydrobenzimidazole Synthesis from p-Benzoquinone and N-Arylamidines and their Cytotoxic Potential. *Eur J Org Chem*, 5878-5884 (2018).

160. Mazumder, A. *et al.* Hydroxycoumarin OT-55 kills CML cells alone or in synergy with imatinib or Synribo: Involvement of ER stress and DAMP release. *Cancer Lett* **438**, 197-218 (2018).

161. Schneider, N.F.Z. *et al.* Cardiac Glycoside Glucoevatromonoside Induces Cancer Type-Specific Cell Death. *Frontiers in pharmacology* **9**, 70 (2018).

162. Lee, J.Y., Mazumder, A. & Diederich, M. Preclinical Assessment of the Bioactivity of the Anticancer Coumarin OT48 by Spheroids, Colony Formation Assays, and Zebrafish Xenografts. *J Vis Exp* (2018).

163. Sommer, C., Straehle, C., Köthe, U. & Hamprecht, F.A. Ilastik: Interactive learning and segmentation toolkit. 2011 IEEE International Symposium on Biomedical Imaging: From Nano to Macro; 2011 30 March-2 April 2011; 2011. p. 230-233.

164. Schindelin, J. *et al.* Fiji: an open-source platform for biological-image analysis. *Nat Methods* **9**, 676-682 (2012).

165. Ji, S. *et al.* The dialkyl resorcinol stemphol disrupts calcium homeostasis to trigger programmed immunogenic necrosis in cancer. *Cancer Lett* **416**, 109-123 (2018).

166. Seidel, C. *et al.* 4-Hydroxybenzoic acid derivatives as HDAC6-specific inhibitors modulating microtubular structure and HSP90alpha chaperone activity against prostate cancer. *Biochem Pharmacol* **99**, 31-52 (2016).

167. Radogna, F. *et al.* Rapid and transient stimulation of intracellular

reactive oxygen species by melatonin in normal and tumor leukocytes. *Toxicol Appl Pharmacol* **239**, 37-45 (2009).

168. Haferlach, T. *et al.* Clinical utility of microarray-based gene expression profiling in the diagnosis and subclassification of leukemia: report from the International Microarray Innovations in Leukemia Study Group. *J Clin Oncol* **28**, 2529-2537 (2010).

169. Kohlmann, A. *et al.* An international standardization programme towards the application of gene expression profiling in routine leukaemia diagnostics: the Microarray Innovations in LEukemia study prephase. *Br J Haematol* **142**, 802-807 (2008).

170. Gautier, L., Cope, L., Bolstad, B.M. & Irizarry, R.A. affy--analysis of Affymetrix GeneChip data at the probe level. *Bioinformatics* **20**, 307-315 (2004).

171. R Development Core Team. R: A language and environment for statistical computing. R Foundation for Statistical Computing; 2010.

172. RStudio Team. RStudio: Integrated Development for R. 2015.

173. Tran, M.Q. *et al.* Unaromatized Tetrahydrobenzimidazole Synthesis from p-Benzoquinone and N-Arylamidines and their Cytotoxic Potential. *Eur J Org Chem* **2018**, 5878-5884 (2018).

174. Lipinski, C.A., Lombardo, F., Dominy, B.W. & Feeney, P.J. Experimental and computational approaches to estimate solubility and permeability in drug discovery and development settings. *Adv Drug Deliv Rev* **46**, 3-26 (2001).

175. Koo, G.B. *et al.* Methylation-dependent loss of RIP3 expression in cancer represses programmed necrosis in response to chemotherapeutics. *Cell Res* **25**, 707-725 (2015).

176. Nauseef, W.M. Biological roles for the NOX family NADPH oxidases. *J Biol Chem* **283**, 16961-16965 (2008).

177. Reddy, M.M. *et al.* NADPH oxidases regulate cell growth and migration in myeloid cells transformed by oncogenic tyrosine kinases. *Leukemia* **25**, 281-289 (2011).

178. Florean, C., Song, S., Dicato, M. & Diederich, M. Redox biology of regulated cell death in cancer: A focus on necroptosis and ferroptosis. *Free Radic Biol Med* **134**, 177-189 (2019).

179. Lúcio, M. *et al.* Antioxidant Activity of Vitamin E and Trolox: Understanding of the Factors that Govern Lipid Peroxidation Studies

In Vitro. *Food Biophys* **4**, 312-320 (2009).

180. Oyewole, A.O. & Birch-Machin, M.A. Mitochondria-targeted antioxidants. *FASEB J* **29**, 4766-4771 (2015).

181. Radogna, F., Dicato, M. & Diederich, M. Natural modulators of the hallmarks of immunogenic cell death. *Biochem Pharmacol* **162**, 55-70 (2019).

182. Jabbour, E. & Kantarjian, H. Chronic myeloid leukemia: 2018 update on diagnosis, therapy and monitoring. *Am J Hematol* **93**, 442-459 (2018).

183. Koptyra, M. *et al.* BCR/ABL kinase induces self-mutagenesis via reactive oxygen species to encode imatinib resistance. *Blood* **108**, 319-327 (2006).

184. Tai, C.J., Chang, S.J., Chien, L.Y., Leung, P.C. & Tzeng, C.R. Adenosine triphosphate induces activation of caspase-3 in apoptosis of human granulosa-luteal cells. *Endocr J* **52**, 327-335 (2005).

185. Gaascht, F. *et al.* Plumbagin modulates leukemia cell redox status. *Molecules* **19**, 10011-10032 (2014).

186. Munoz, F.M., Zhang, F., Islas-Robles, A., Lau, S.S. & Monks, T.J. From the Cover: ROS-Induced Store-Operated Ca2+ Entry Coupled to PARP-1 Hyperactivation Is Independent of PARG Activity in Necrotic Cell Death. *Toxicol Sci* **158**, 444-453 (2017).

187. Karvela, M. *et al.* ATG7 regulates energy metabolism, differentiation and survival of Philadelphia-chromosome-positive cells. *Autophagy* **12**, 936-948 (2016).

188. Chen, Y.F. *et al.* The roles of reactive oxygen species (ROS) and autophagy in the survival and death of leukemia cells. *Crit Rev Oncol Hematol* **112**, 21-30 (2017).

189. Ianniciello, A., Rattigan, K.M. & Helgason, G.V. The Ins and Outs of Autophagy and Metabolism in Hematopoietic and Leukemic Stem Cells: Food for Thought. *Frontiers in Cell and Developmental Biology* **6**, 120 (2018).

190. Fan, Q.W. *et al.* Akt and autophagy cooperate to promote survival of drug-resistant glioma. *Sci Signal* **3**, ra81 (2010).

191. Kim, H.J. *et al.* Shikonin-induced necroptosis is enhanced by the inhibition of autophagy in non-small cell lung cancer cells. *J Transl Med* **15**, 123 (2017).

192. Onodera, J. & Ohsumi, Y. Autophagy is required for maintenance of amino acid levels and protein synthesis under nitrogen starvation. *J Biol Chem* **280**, 31582-31586 (2005).

193. Mancilla, H. *et al.* Glutathione Depletion Induces Spermatogonial Cell Autophagy. *J Cell Biochem* **116**, 2283-2292 (2015).

194. Sun, Y., Zheng, Y., Wang, C. & Liu, Y. Glutathione depletion induces ferroptosis, autophagy, and premature cell senescence in retinal pigment epithelial cells. *Cell Death Dis* **9**, 753 (2018).

195. Armstrong, J.A. *et al.* Oxidative stress alters mitochondrial bioenergetics and modifies pancreatic cell death independently of cyclophilin D, resulting in an apoptosis-to-necrosis shift. *J Biol Chem* **293**, 8032-8047 (2018).

196. Liu, S. *et al.* Lysosomal damage after spinal cord injury causes accumulation of RIPK1 and RIPK3 proteins and potentiation of necroptosis. *Cell Death Dis* **9**, 476 (2018).

197. Sun, S.Y. N-acetylcysteine, reactive oxygen species and beyond. *Cancer biology & therapy* **9**, 109-110 (2010).

198. Hamad, I., Arda, N., Pekmez, M., Karaer, S. & Temizkan, G. Intracellular scavenging activity of Trolox (6-hydroxy-2,5,7,8-tetramethylchromane-2-carboxylic acid) in the fission yeast, Schizosaccharomyces pombe. *J Nat Sci Biol Med* **1**, 16-21 (2010).

199. Krishna, C.M. *et al.* The catecholic metal sequestering agent 1,2-dihydroxybenzene-3,5-disulfonate confers protection against oxidative cell damage. *Arch Biochem Biophys* **294**, 98-106 (1992).

200. Wright, D.J. *et al.* N-Acetylcysteine improves mitochondrial function and ameliorates behavioral deficits in the R6/1 mouse model of Huntington's disease. *Transl Psychiatry* **5**, e492 (2015).

201. Wiedmer, T. *et al.* Autophagy Inhibition Improves Sunitinib Efficacy in Pancreatic Neuroendocrine Tumors via a Lysosome-dependent Mechanism. *Mol Cancer Ther* **16**, 2502-2515 (2017).

202. Schnekenburger, M., Dicato, M. & Diederich, M.F. Anticancer potential of naturally occurring immunoepigenetic modulators: A promising avenue? *Cancer* **125**, 1612-1628 (2019).

203. Liu, C.C. *et al.* Integrins and ERp57 Coordinate to Regulate Cell Surface Calreticulin in Immunogenic Cell Death. *Front Oncol* **9**, 411 (2019).

204. Long, J.S. & Ryan, K.M. New frontiers in promoting tumour cell death: targeting apoptosis, necroptosis and autophagy. *Oncogene* **31**, 5045-5060 (2012).

Abstract in Korean (국문초록)

새로운 반합성 천연물 TMQ (Unaromatized Tetrahydrobenzimidazole)는 p-Benzoquinone 과 N-Arylamidines에서 합성된 물질이며, 만성 골수성 백혈병 (CML) 에서 다양한 세포 사멸 형태인 apoptosis, necroptosis 및 Autophagy를 동시에 유발하는 새로운 저분자 천연물질이다. 오랫동안 Programmed cell death에 있어서 apoptosis가 유일한 것으로 여겨져 왔으나 최근에는 necrosis과정에도 programmed necrosis 또는 necroptosis라 불리는 세포사멸이 존재한다는 것이 밝혀졌다. 최근 necroptosis에는 RIP1과 RIP3가 중요 조절인자임이 알려지고 있으나 현재까지 관련 연구의 많은 부분이 미미한 수준이고 많은 연구가 필요한 분야임을 확인할 수 있었다. 또한 기존에 알려지지않은 autophagy가 apoptosis와 necroptosis에 어떤 작용을 하는지에 대한 연구가 필요하며, 특이적이고 결정적인 조절인자의 차이점에 대하여 많은 연구가 필요한 실정이다. 선행연구를 통해 TMQ 시리즈 중 건강한 PBMC (A peripheral blood mononuclear cell) 세포에서는 독성을 일으키지 않으며 여러 종류의 암세포에서 특이적으로 세포독성을 일으키는 TMQ0153을 선별하였다.

따라서 TMQ0153을 통해 낮은 농도에서 유도된 canonical-programmed 세포사멸은 caspase에 의존적이지만 높은 농도에서 유도된 non-canonical-programmed 세포사멸은 caspase와 무관하며 미토콘드리아의 기능장애를 거쳐 ROS를 축적시켜 그 결과 세포스트레스와 다른 미토콘드리아의 손상을 일으킴을 seahorse XFp cell mito stress 및 FACS를 통해 입증하였고, 세포스트레스의 작용으로 necroptosis 세포사멸이 일어나기 전에 autophagy가 먼저 일어남을 공초점 형광 현미경과 관련 단백질 LC3과 p62의 western blotting을 통해 관찰하였다. 또한 autophagy의 핵심 단백질 Beclin-1의 knockdown을 통해 억제시킨뒤 TMQ0153을 투여하였을때 세포사멸이 더 증가하였으며 이는 암세포를 민감하게 (Sensitization)하는 것을 밝혀내었다. 전자현미경 이미지를 분석함으로써 autophagy가 일어나는 시점에서 미토콘드리아의 팽창 및 autophagosome 의 형성을 추가 관찰하였고, 세포스트레스의 요소로 세포질의 Ca^{2+} 축적, 세포내 GSH (Glutathione)의 감소 및 Lysosomal membrane potential (LMP) 의 증가를 FACS와 형광 현미경을 통해 분석하였다. 세포스트레스의 증가 및 necroptosis와 관련있는 특이적 PARP-1 (C2-10), RIP1 단백질의 검출, 세포내 ATP의 급격한 감소가 necroptosis의 원인임을 알

수 있었고 이러한 효과는 necrostatin-1에 의해 저해됨을 증명하였다. 이어서 TMQ0153 에 의해 유도되는 necroptosis는 mitochondria membrane permeabilization (MMP) 를 증가시키고 N-Acetyl Cysteine (NAC)에 의해 세포사멸 및 미토콘드리아가 보존되는 것을 입증할 수 있었다.

최근 선행연구에 따르면 RIP3단백질은 necroptosis를 조절 하는 핵심 단백질로 알려져 있는데, 많은 암세포에서 현저히 감소되어 새로운 암세포 사멸 전략으로 활용하는데 한계가 있었다. 또한 암세포의 특징중 하나인 apoptosis에 대한 저항성은 암세포가 항암제에 저항할 수 있게 함으로써, 암세포 사멸 전략의 한계점을 가져왔다. 따라서 이를 극복할 Necroptosis를 일으키는 약물의 기전연구를 통해 약물의 저항성을 극복하는 방법을 제시할 수 있었다. 탈메틸화제 (5-aza-2'-deoxycytidine; 5'aza)를 투여하여 암발생으로 감소된 RIP3 단백질을 복구한 뒤 TMQ0153을 투입한 결과, TMQ0153만 투여한 암세포보다 더 많은 necroptosis를 관찰할 수 있었음을 형광현미경을 통해 확인하였다. TMQ0153이 처리된 Necroptosis가 일어난 세포로부터 HMGB1의 방출과 세포외 ATP의 증가, Ecto-Calreticulin와 ERp57 의 세포막 노출 및 증가를 관찰함으로써 이 천연물질의 면역세포사멸과 이에 따른 중계연구의 가능성을 제시할 수 있었다. 마지막으로 TMQ0153가 콜로니와 In vivo 제브라피쉬 xenograft 모델에서 종양형성의 발달을 저해하는 것을 추가적으로 관찰하였다. 따라서 본 연구를 통해 제시된 다양한 세포사멸의 현상을 조절하는 세포스트레스의 원인 분석 및 항암제의 분자 작용과 세포사멸 제어 기전을 규명하여 효과적인 암 치료제 개발에 활용하고자 한다.

주요어

세포스트레스, 미토콘드리아, 활성산소, 만성 골수성 백혈병, 프로그램된 세포사멸